FEDERAL UNIVERSITY OF SÃO CARLOS
CENTER FOR EXACT SCIENCES AND TECHNOLOGY
GRADUATE PROGRAM IN MATERIALS SCIENCE AND ENGINEERING

MICROSTRUCTURE, CORROSION, AND WEAR RESISTANCE OF A BORON-MODIFIED DUPLEX STAINLESS STEEL PRODUCED BY LASER POWDER BED FUSION

Brenda Juliet Martins Freitas

São Carlos-SP
2024

FEDERAL UNIVERSITY OF SÃO CARLOS
CENTER FOR EXACT SCIENCES AND TECHNOLOGY
GRADUATE PROGRAM IN MATERIALS SCIENCE AND ENGINEERING

MICROSTRUCTURE, CORROSION, AND WEAR RESISTANCE OF A BORON-MODIFIED DUPLEX STAINLESS STEEL PRODUCED BY LASER POWDER BED FUSION

Brenda Juliet Martins Freitas

Thesis presented to the Graduate Program of Materials Science and Engineering as a partial requirement to obtain the title of DOCTOR IN MATERIALS SCIENCE AND ENGINEERING

Supervisor: Dr. Claudemiro Bolfarini
Co-supervisor: Dr. Guilherme Yuuki Koga
Cotutelle Supervisor: Dr. Sergio de Traglia Amâncio-Filho
Scholarships: CAPES/PROEX (01/03/2019 to 31/07/2019), FAPESP (01/08/2019 to 28/02/2022 and 01/02/2023 to 31/01/2024, n° 2019/05885-7), FAPESP/BEPE (01/03/2022 to 31/01/2023, n° 2021/10735-4)

São Carlos-SP
2024

VITAE

Master in Materials Science and Engineering – Federal University of São Carlos (2019)

Bachelor in Materials Engineering – Federal University of Technology – Paraná (2016)

UNIVERSIDADE FEDERAL DE SÃO CARLOS

Centro de Ciências Exatas e de Tecnologia
Programa de Pós-Graduação em Ciência e Engenharia de Materiais

Folha de Aprovação

Defesa de Tese de Doutorado da candidata Brenda Juliet Martins Freitas, realizada em 18/03/2024.

Comissão Julgadora:

Prof. Dr. Claudemiro Bolfarini (UFSCar)

Prof. Dr. Guilherme Zepon (UFSCar)

Prof. Dr. Piter Gargarella (UFSCar)

Prof. Dr. Rubens Caram Júnior (UNICAMP)

Prof. Dr. Sergio de Traglia Amancio Filho (TU Graz)

O Relatório de Defesa assinado pelos membros da Comissão Julgadora encontra-se arquivado junto ao Programa de Pós-Graduação em Ciência e Engenharia de Materiais.

ACKNOWLEDGMENTS

I would like to express my deepest gratitude to my supervisor, Prof. Dr. Claudemiro Bolfarini, who generously provided knowledge and expertise in the last few years. I am grateful to my supervisor, Prof. Dr. Sergio de Traglia Amancio Filho, for his essential contribution to my work. Also, I am extremely grateful to my co-supervisor, Prof. Dr. Guilherme Yuuki Koga, for the opportunity to learn so much from him.

I am also grateful to all my colleagues, professors, laboratory technicians, and other university staff at UFSCar and TU Graz for all their support, and for also impacting and inspiring me.

I would like to thank the Fundação de Amparo à Pesquisa do Estado de São Paulo (FAPESP) for the financial support to carry out this study with the following grants: n° 2019/05885-7 and n° 2021/10735-4 (BEPE/FAPESP). I also would like to thank the Coordenação de Aperfeiçoamento de Pessoal de Nível Superior/CAPES for the scholarship (CAPES/PROEX n° 88887.334679/2019-00).

This study was financed in part by the Coordenação de Aperfeiçoamento de Pessoal de Nível Superior - Brasil (CAPES) - Finance Code 001.

I also would like to thank to the Conselho Nacional de Desenvolvimento Científico e Tecnológico - Brasil/CNPq, Austrian aviation program ‘‘TAKE OFF” (PILOT, grant number 852796, 2018), and BMK – The Austrian Ministry for Climate Action, Environment, Energy, Mobility, Innovation and Technology.

I would like to recognize the Laboratory of Structural Characterization (LCE/DEMa/UFSCar) for the general facilities, and the electrochemical facilities of the Center for Development and Characterization of Material (CCDM/DEMa/UFSCar).

Lastly, I would like to mention my family (Nair, Renilson, Renan, Bruno, Monique, Mariana, Valentina and Marcos), my spouse Thiago, my cats Shoyu and Tarê, and my friends (especially Teka, Luana, Ladil, and Malu). Their support was essential in keeping my motivation high during this process.

ABSTRACT

A duplex stainless steels (DSS) containing 0.3 and 0.6 wt.% of boron were produced by laser powder bed fusion (L-PBD) with parameters based on Box-Behnken design. The microstructure was evaluated by XRD, OM, SEM, EBSD, TEM, and ASTAR. Additionally, the alloys were characterized by Vickers microhardness, reciprocating pin-on-plate wear test in sliding mode, and the electrochemical behavior was assessed by cyclic potentiodynamic polarization, electrochemical impedance spectroscopy, and double loop electrochemical potentiokinetic reactivation tests in chloride electrolyte. The results were compared to a pure duplex stainless steel obtained by hot-rolling and by LPBF. Hot-rolled pure DSS presents a dual-phase (α+γ) microstructure with elongated grains along the rolling axis, whereas the as-built LPBF pure DSS exhibits coarsened columnar δ-Fe grains parallel to the building direction. In contrast, boron addition promoted an outstanding grain refinement, resulting in a microstructure non-textured microstructure and composed of refined equiaxed δ-Fe grains with Cr_2B nanoborides decorating the grain boundaries. Such excellent grain refinement is ascribed to the segregation of boron and accumulation of a boron-enriched boundary layer ahead of the growing solid-liquid interface during LPBF solidification. Regarding hardness and wear resistance, compared to the commercial hot-rolled DSS, the LPBF-produced pure DSS presented enhanced hardness and wear resistance, which are further increased by boron addition. Moreover, LPBF-produced boron-containing stainless steel revealed high pitting resistance, great repassivation ability, and unsensitized microstructure in 0.6M NaCl solution, being comparable to pure DSS produced by LPBF and by hot-rolling. Therefore, the addition of boron is responsible for the formation of a wear- and corrosion-resistant ultrafine-grained LPBF-produced stainless steel, opening the possibility of applying this material in challenging environments givens its excellent basket of electrochemical and tribological properties.

Keywords: Additive manufacturing; Grain refinement; Nanoborides; Tribology; Electrochemical behavior; Stainless steel

RESUMO

MICROESTRUTURA E RESISTÊNCIA A CORROSÃO E AO DESGASTE DE UM AÇO INOXIDÁVEL DUPLEX MODIFICADO COM BORO PRODUZIDO POR *LASER POWDER BED FUSION*

Um aço inoxidável duplex contendo 0.3 e 0.6 %p. de B foi produzido por *laser powder bed fusion* (L-PBF). A microestrutura foi avaliada por meio de DRX, MO, MEV, EBSD, MET e ASTAR. Além disso, as ligas foram avaliadas por meio dos seguintes ensaios: dureza Vickers, ensaio de desgaste recíproco pino-sobre-placa, polarização potenciodinâmica cíclica, espectroscopia de impedância eletroquímica, e teste de sensitização *dual-loop*. Para comparação, utilizou-se um aço inoxidável duplex puro processado por laminação a quente e por L-PBF. Os aços inoxidáveis puros processados por laminação a quente e por L-PBF apresentam, respectivamente, uma microestrutura duplex com grãos alongados no eixo de laminação, e uma microestrutura ferrítica com grãos colunares e paralelos à direção de crescimento da peça. As ligas modificadas com boro e produzidas por L-PBF apresentam uma microestrutura ferrítica, com grãos ultrafinos e equiaxiais, e nanoboretos do tipo Cr_2B presentes nos contornos de grão. É proposto que o refinamento de grão promovido pela adição de boro ocorra devido ao aumento do super-resfriamento térmico e de uma reação eutética nos últimos estágios de solidificação. A dureza e resistência ao desgaste apresentadas pela liga modificada com boro é significativamente superior às ligas puras produzidas por laminação a quente e por L-PBF. Além disso, a liga modificada com boro apresenta elevada resistência a pites, habilidade de promover repassivação em meio clorídrico, e não apresenta sensitização, sendo semelhante ao aço inoxidável duplex puro obtido por laminação e por L-PBF. Dessa forma, a adição de boro é responsável pela formação de um aço inoxidável com grãos ultrafinos e resistente a corrosão e ao desgaste, ampliando a possibilidade de utilização desses aços em ambientes agressivos onde demanda-se elevada resistência a corrosão e ao desgaste.

Palavras-chave: Manufatura aditiva; Refinamento de grão; Nanoboretos; Tribologia; Comportamento eletroquímico; Aços inoxidáveis

PUBLICATIONS

Scientific papers:

FREITAS, B.J.M., OLIVEIRA, V.A., GARGARELLA, P., KOGA, G.Y., BOLFARINI, C. Microstructural characterization and wear resistance of boride-reinforced steel coatings produced by Selective Laser Melting (SLM). **Surface and Coatings Technology**, v. 426, 127779, 2021. DOI: 10.1016/j.surfcoat.2021.127779

FREITAS, B.J.M., RODRIGUES, L.C.M., CLAROS, C.A.E., BOTTA, W.J., KOGA, G.Y., BOLFARINI, C. Ferritic-induced high-alloyed stainless steel produced by laser powder bed fusion (L-PBF) of 2205 duplex stainless steel: Role of microstructure, corrosion, and wear resistance. **Journal of Alloys and Compounds**, v. 918, 165576, 2022. DOI: 10.1016/j.jallcom.2022.165576

FREITAS, B.J.M., KOGA, G.Y., RODRIGUES, L.C.M., BOTTA, W.J., AMANCIO-FILHO, S.T., BOLFARINI, C. Ultrafine-grained stainless steel with wear-resistant nanoborides decorating grain boundaries produced by laser powder bed fusion. Paper submitted to **Materialia** journal in December 2023.

FREITAS, B.J.M., KOGA, G.Y., ARNEITZ, S., BOLFARINI, C., AMANCIO-FILHO, S.T. Optimizing LPBF-parameters by Box-Behnken design allows to print crack-free and dense high-boron alloyed stainless steels. Paper submitted to **Additive Manufacturing Letters** in December 2023.

FREITAS, B.J.M., KOGA, G.Y., AMANCIO-FILHO, S.T., BOLFARINI, C. Solute-induced grain refinement in a boron-containing stainless steel produced by laser powder bed fusion. Paper to be submitted to **Advanced Materials** journal in February 2024.

FREITAS, B.J.M., KOGA, G.Y., AMANCIO-FILHO, S.T., BOLFARINI, C. LPBF printing ensures corrosion-resistant and ultrafine-grained stainless steel with

grain boundaries decorated with nanoborides. Paper to be submitted to **Electrochimica Acta** journal in February 2024.

Conference presentation:

FREITAS, B.J.M., RODRIGUES, L.C.M., CLAROS, C.A.E., BOTTA, W.J., KOGA, G.Y., BOLFARINI, C. Ferritic-induced high-alloyed stainless steel produced by laser powder bed fusion of a duplex stainless steel. Oral presentation in VI International Conference of the Institute of Solid-State Chemistry and Mechanochemistry SB RAS, Novosibirsk State University, Russia, November 2022.

FREITAS, B.J.M., KOGA, G.Y., RODRIGUES, L.C.M., BOTTA, W.J., AMANCIO-FILHO, S.T., BOLFARINI, C. Wear and corrosion behavior of a boron-modified duplex stainless steel produced by laser powder bed fusion. Poster presentation in XXI B-MRS Meeting (SBPMat), Maceió-Brazil, October 2023. **Award-winning presentation:** Bernhard Gross Award 2023, Brazilian Materials Research Society, and Best poster XXI B-MRS 2023, American Chemical Society.

FREITAS, B.J.M., KOGA, G.Y., VIEIRA, A.C.M., BOTTA, W.J., AMANCIO-FILHO, S.T., BOLFARINI, C. Wear-resistant Boron-modified Superferritic Stainless Steel. Poster presentation in 29th Congress of the Brazilian Society of Microscopy and Microanalysis and the XVII Interamerican Congress on Microscopy, Olinda-Brazil, November 2023.

FREITAS, B.J.M., KOGA, G.Y., AMANCIO-FILHO, S.T., BOLFARINI, C. Wear Resistant Boron-Modified Stainless Steel Produced by Laser Powder Bed Fusion. Poster presentation in Advanced Materials Research Grand Meeting (MRM and IUMRS-ICA), Kyoto-Japan, December 2023.

SUMMARY

TABLES SUMMARY

FIGURES SUMMARY

SYMBOLS AND ABBREVIATIONS

ΔT: undercooling

ΔT_{cs}: constitutional undercooling

ΔT_n: critical nucleation undercooling

ΔT_t: thermal undercooling

ANOVA: analysis of variance

AM: additive manufacturing

ASTM: American Society for Testing and Materials

BCC: body centered cubic

BD: building direction

CPP: cyclic potentiodynamic polarization

COF: coefficient of friction

CS: constitutional undercooling

DF: dark field

DL-EPR: electrochemical potentiokinetic reactivation

DOE: design of experiment

DSS duplex stainless steel

EBSD: electron backscattered diffraction

E_{corr}: corrosion potential

EDX: energy dispersive X-Ray

EIS: electrochemical impedance spectroscopy

E_{rep}: repassivation potential

E_{transp}: transpassivation potential

FCC: face centered cubic

FSSs: ferritic stainless steels

G: thermal gradient

GBs: grain boundaries

G×R: cooling rate

HAZ: heat affected zone

HV: Vickers hardness

HVOF: velocity oxygen fuel

i_{corr}: corrosion current density

i_{pass}: passive current density
IPF: inverse pole figure
IQ: image quality
k: specific wear rate
L-PBF: laser powder bed fusion
OCP: open circuit potential
OM: optical microscopy
PED: precession electron diffraction
PF: pole figures
PTA: plasma transferred arc
Q: grain growth restriction factor
R: solidifying rate
SAED: selected area electron diffraction
SAF: Sandvik Austenitic Ferritic
SEM: scanning electron microscopy
S/L: solid liquid
STEM: scanning transmission electron microscope
TEM: transmission electron microscopy
XRD: X-ray diffraction
α: alpha-ferrite
γ: gamma-austenite
δ: delta-ferrite

1 INTRODUCTION

Several components operating under harsh conditions such as in the oil and gas, fertilizer and chemical industries are facing several degradation threat related to wear and/or corrosion. These issues may lead to expensive repair/maintenance costs and, in event of equipment failure, can represent a risk to human health and the environment [1].

Stainless steels are widely used in demanding environments due to their combination of strength, toughness and corrosion resistance, being cost-effective compared to other alloys, such as Ni-based superalloys. Besides the wide variety of stainless steel, several alloying elements and processing routes are capable to tailor their microstructure and properties [2]. Although presenting excellent corrosion resistance in chloride media with reliable bulk mechanical properties, stainless steel may present inadequate wear resistance.

Wear-resistant boron-modified stainless steels have been widely studied over the last few years, being obtained by spray forming, casting, and thermal spraying [3-12]. The addition of boron content far beyond the solubility limit in stainless steels promotes the formation of hard borides, which proved to be effective to enhance the hardness and wear resistance of these materials, without significantly impairing the corrosion resistance if the elemental partitioning is controlled.

Laser powder bed fusion (L-PBF) is a metal additive manufacturing technique, being used to process several metals and alloys. L-PBF presents several advantages, such as the production of components with complex geometries, high dimensional precision, relatively good surface quality, raw material savings, and production in a relatively short time [13].

Boron-modified stainless steels are hard and wear resistant, consequently, also present low machinability, which makes their finishing restricted. Therefore, the production of boron-modified duplex stainless steel by L-PBF is under interest given the capability to produce rapidly near-net-shape components with complex geometries, which may reduce or even avoid additional costs related to cutting and machining.

Moreover, metals and alloys produced by L-PBF typically have coarse columnar grain structure, which present anisotropy of properties and tendency to hot-cracking. Strategies [14-27] have been successfully applied to mitigate the formation of columnar grain structure and favor the development of a refined and equiaxed microstructure in L-PBF-produced alloys.

For conventional casting process, boron is effective for grain refinement of ferrous-alloys, given its high grain growth restriction factor (Q) [6, 28]. However, the L-PBF solidification aspects differ from those found in the casting process [22-24], and the efficiency of boron in grain refining of L-PBF-processed steels is of interest.

Given the numerous advantages of L-PBF, the processing of stainless steels modified with boron through additive manufacturing techniques is unprecedented and presents a great scientific and technological interest. Moreover, there is great interest in evaluating the solidification aspects of these alloys under L-PBF solidification conditions, in addition to the resulting microstructure and properties.

2 LITERATURE REVIEW

2.1 Boron-modified stainless steels

Although the corrosion resistance attribute of stainless steels, this class of material may be sensitive to wear resistance depending on the application, which may be risky since they are commonly used in environments where corrosion and wear occur concomitantly. The development of stainless steels reinforced with hard borides has shown to be effective to improve their wear resistance [3-12, 26, 29].

The wear performance of steels reinforced with hard particles depends on the size, volume and distribution of these particles, the matrix features, also on the particular wear mechanisms present in a given tribological system. The processing technique thus plays an important role in obtaining suitable microstructures for component employed in different applications [3, 6].

Compared to carbides, borides present a very high stability in steels. Unlike carbides that may be formed in solid-state transformation during proper heat treatments, the formation of borides normally occurs only during solidification, given the low solubility of boron in ferrite and austenite (<0.008 wt.% [30]). Addition of boron to stainless steels may lead to the formation of M_2B and M_3B_2 phases, in which M is composed of transition metals typically present in stainless steels, such as Fe, Cr, and Mo [3-5].

Recent studies reported that spray-formed stainless steels (e.g., duplex [3], superduplex [4], ferritic [10, 11], and supermartensitic [5-7]) modified with different boron contents (0.3 - 3.5 wt.%) exhibit micro-sized borides homogeneously distributed within a relatively refined equiaxed microstructure. Depending on the solidification path based on the alloy's composition, borides may present different morphologies and percolation. These studies report that hypoeutectic compositions present an interconnected network of eutectic borides surrounding the grains, serving as a rigid and hard skeleton (Fig. 2.1a); unlike hypereutectic compositions, in which the borides morphology is faceted, elongated and non-connected, as illustrated in Fig. 2.1b from a boron-modified ferritic stainless steel [10]. Moreover, for a hypoeutectic stainless steel, given the solidification aspects present in spray forming [5], it was shown that increasing

the boron content, the volume fraction of borides is also increased, and the grain size decreases [5-7, 11]. It is an indication that boron plays a significant role in grain refinement during solidification in spray forming, as can be seen from the micrographs of a boron-modified supermartensitic stainless steel [6] present in Figs. 2.1c, d.

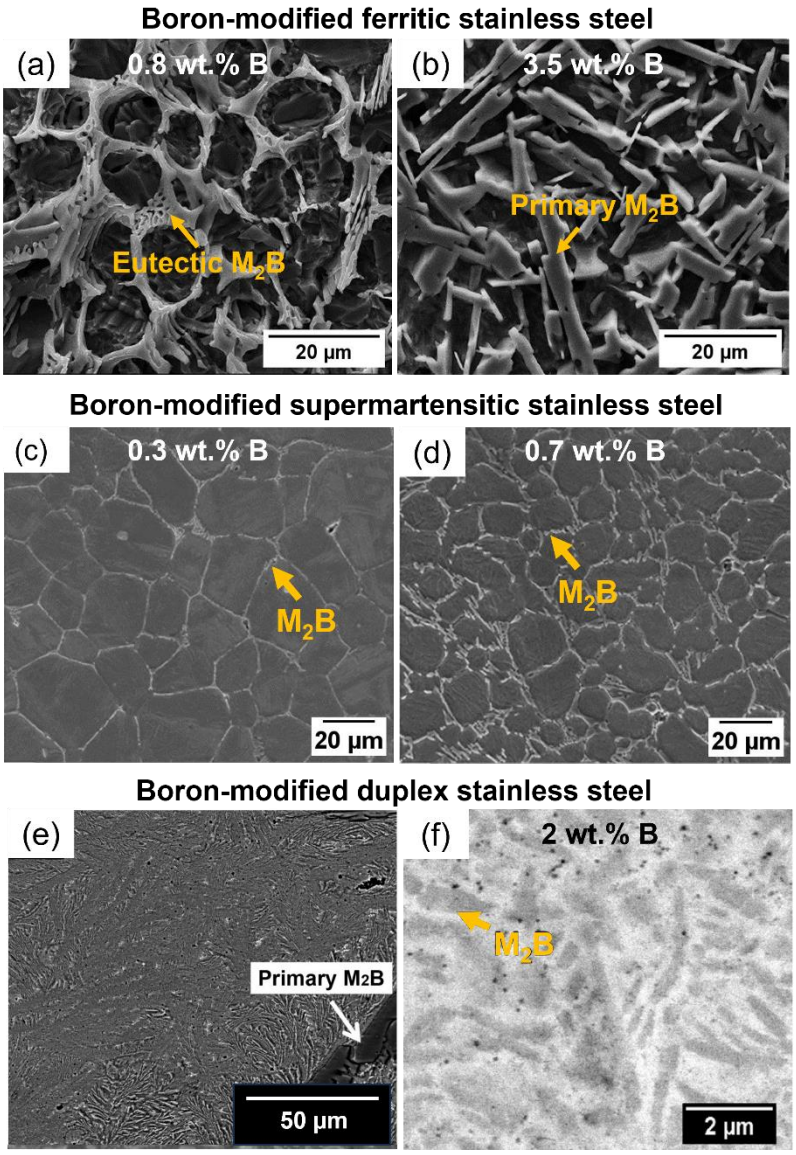

Figure 2.1 - SEM micrographs of a spray-formed ferritic stainless steel modified with (a) 0.8 (hypoeutectic) and (b) 3.5 wt.% of boron (hypereutectic), a spray-formed supermartensitic stainless steel modified with (c) 0.3 and (d) 0.7 wt.% of boron, and boron-modified duplex stainless steel coatings produced by (e) PTA and (f) L-PBF. A deep etching procedure was applied to remove the matrix in a,

b. Illustration adapted from [6, 8, 10, 29]. Reprinted from [6, 8] with permission from Elsevier. Reprinted from [10] with permission from Springer.

Besides spray forming, coatings of a boron-modified supermartensitic, superduplex, and duplex stainless steels were successfully produced by high-velocity oxygen fuel (HVOF) [12], plasma transferred arc (PTA) [8], and laser powder bed fusion (L-PBF) [29]. In general, micro-sized borides were found within the refined microstructure of the coatings. However, compared to PTA process, HVOF and L-PBF-produced coatings present higher degree of microstructural refinement given their solidification aspects. Unlike PTA-produced coating, with the boride particles ~10 - 20 μm in length (see Fig. 2.1e), a similar alloy produced by LPBF presents flake-like borides of ~2 μm length homogeneously distributed in a refined δ-ferritic matrix (grain size of ~2 μm), being ascribed to the high cooling rates imposed during LPBF solidification (Fig. 2.1f) [29].

Further, boron-modified duplex, ferritic and austenitic stainless steels were recently produced by copper-mold [31] and graphite mold casting [9]. It was reported [31] that, instead of the typical cast columnar grain structure, the addition of 2.5 wt.% of boron to a cast duplex stainless steel allowed the production of a refined equiaxed microstructure with borides in small round shape (~10 μm diameter), suggesting that the borides served as nucleation sites for refined δ-ferrite and γ-austenite for hypereutectic alloys.

Lately, a boron-modified austenitic stainless steel obtained by mechanical mixing of 316L powder and micron-sized boron powder at an amount of 0.5 and 1 wt.% was subjected to production by L-PBF. By increasing the boron content, hardness increases, and the grain size slightly reduces from 14 μm (pure alloy) to 5 μm (1 wt.% of boron) [26].

In general, boron-modified stainless steels produced by different techniques present an enhancement of hardness and wear resistance by increasing the boron content since the formation of hard particles of borides protects the matrix against mechanical removal [3, 4, 5-12, 26, 29, 31]. Moreover, although the formation of borides may consume part of the chromium content, the corrosion resistance of these alloys is not impaired as long as the chromium

content in the matrix is maintained above ~12 wt.% and no excessive Cr depletion zones are formed [5, 6, 11].

Several processing techniques have proven to be effective in obtaining different grades of boron-modified stainless steels with excellent wear and corrosion resistance [3-12, 29, 31]. For practical applications, L-PBF may be an interesting technique to produce bulk duplex stainless steels modified with boron, as these alloys present high hardness and wear resistance; hence, their production by additive manufacturing may reduce or even avoid additional costs related to cutting and machining, along with avoiding damage and wear of machining tooling.

2.2 Laser powder bed fusion (L-PBF)

In constant progress and presenting great potential for industrial application, L-PBF is considered as the most versatile and investigated metal additive manufacturing (AM) process, being applied to produce a wide range of metals and alloys and components. Compared to other AM techniques, L-PBF allows the production of components with complex geometries/design flexibility, high dimensional precision, relatively good as-built surface quality, with raw material savings, and in a relatively short production time [32, 33].

The manufacture of components by L-PBF involves a high-power laser beam that selectively melts successive layers of a metallic powder under an inert atmosphere. Hence, a bed/layer of a metallic powder is placed on a substrate, and the laser beam melts pre-defined areas of the first layer; sequentially, the underlying substrate is lowered and another layer of metallic powder is deposited. This step consecutively repeats until the entire component is built [32]. The L-PBF process can be seen schematically in Fig. 2.2a.

The main challenge of industrial use of L-PBF is the production of parts with high density and free of processing defects (e.g., thermal cracks, balling, delamination, lack of fusion, porosity, etc.), which are closely related to the proper adjustment of the L-PBF-processing parameters, such as laser power (P), scanning speed (v), hatch spacing (h), layer thickness (t), scanning strategy, etc. [34, 35].

The laser power is the energy supplied to melt the powder, in which low laser power values result in insufficient melting. The laser scanning speed is the velocity that the laser source moves to melt the powders, in which lower scanning speed values develop high temperatures ensuing in overspreading, increasement of the melt pool width/depth, and may increase the gas dissolution into the molten metal; on the other hand, high scanning speed values limit the liquid spreading ability and may result in insufficient melting [36]. The scanning strategy is a pre-defined geometric pattern in which the laser beam will move, impacting the building time, and manufacturing defects. The hatching space is the distance between two adjacent scanning tracks. Smaller hatching values increase the densification, improve the surface quality, and increase the production time [34-36]. Larger distances between adjacent tracks may result in lack of overlapping tracks, and formation of gaps/voids. Higher layer thickness values may promote higher surface roughness, and increase porosity since higher power is necessary to penetrate through the wide powder layers [36].

The quality of L-PBF-produced parts are extensively affected by the L-PBF-parameters, being used to determine the energy density, as can be seen in Equation 2.1. In general, sufficient energy density is fundamental for melting the powder and, consequently, increase the density of the parts. However, increasing the energy density, the surface quality may be negatively affected by balling phenomenon [36, 37].

$$(E = \frac{P}{(vht)}) \qquad \text{Eq. 2.1}$$

Moreover, L-PBF is considered a non-equilibrium solidification process since its large thermal gradient and high cooling rate induce an epitaxial grain growth and lead to the formation of columnar grains elongated along the build direction (BD), which normally present a strong <100> texture for BCC and FCC metals [35, 36]. Also, given the repeated heating and cooling cycles that the material is subjected, L-PBF-produced metals and alloys often present non-equilibrium microstructures, microsegregation, high residual stress, and increased solidification cracking susceptibility [38-40].

The interaction between laser beam and metallic powder results in the formation of a melt pool, which geometry directly affects the final microstructure of the L-PBF-printed part, being closely related to the processing parameters, material's properties (e.g., thermal conductivity), and the complex physical phenomena within the melt pool caused by the thermal gradient (e.g., gravity, surface tension and capillary forces) [41, 42]. The laser heat input also affects part of the previously solidified layers, creating a heat affected zone (HAZ), which may undergo solid phase transformation and grain coarsening. Moreover, the fast cooling rate in L-PBF may also increases solid solute solubility, since a higher amount of solute are trapped by the fast growing crystal interface, which may promote unexpected phase precipitation during further heating and cooling cycles provoked by subsequent layers [41, 43].

Although the molten metal within the melt pool experiences complex thermal cycles, the L-PBF solidification follows well-established solidification models [44]. The grain growth in the melt pool is governed by the time-dependent temperature distribution which affects the thermal gradient (G), and the growth/solidification rate (R) of the solid-liquid (S/L) interface. G and R influence the direction and size of the growing grain during solidification in L-PBF, respectively. Likewise, the morphology and grain size of the solidified grains are determined by the G/R ratio (i.e., planar (high G/R), cellular, columnar dendritic or equiaxed dendritic (low G/R)), and G×R cooling rate (i.e., coarsened (lower G×R), refined (higher G×R)), respectively [45, 46].

Even though its magnitude depends on the processing parameters, the L-PBF solidification aspects are commonly characterized for presenting high values of G and G×R. The solidification starts with heterogeneous nucleation at the building substrate. After nucleation, the grains grow along the maximum G direction, towards the center of the melt pool, facilitating the maximum heat extraction. As the processing progress with the following molten layers, the current molten metal tends to epitaxially grow from the grains of the previous solidified layer (low nucleation barrier), resulting in the formation of large columnar grains crossing several layers [47]. Fig. 2.2b illustrates the solidification within the melt pool.

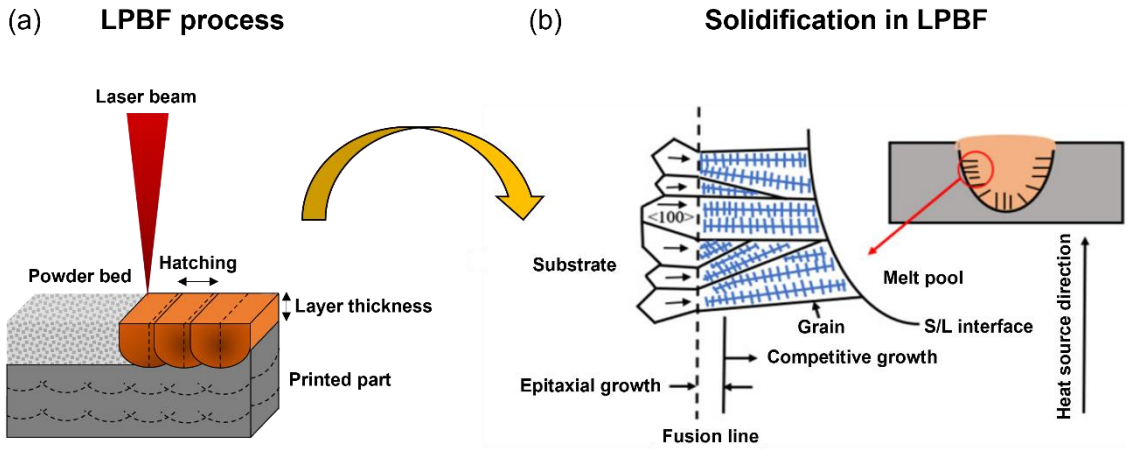

Figure 2.2 - Illustration of the laser powder bed fusion showing (a) the process and the main processing parameters, and (b) the solidification of the molten metal within the melt pool. Adapted from [34] (CC BY 4.0).

Therefore, even though L-PBF presents challenges regarding the adequate selection of processing parameters, and besides the tendency to form highly textured microstructures, L-PBF has a great industrial and technological appeal given its numerous advantages. Thus, there is a great interest in producing several alloys by L-PBF, as well as explore strategies to minimize common defects and crystallographic texture.

2.3 Duplex stainless steels produced by L-PBF

Duplex stainless steels (DSSs) grade consists of a dual phase ferritic-austenitic microstructure, which is responsible for combining high strength, toughness, and excellent corrosion resistance in several environments. These alloys are widely applied in aggressive environmental conditions and under high mechanical loads, such as in chemical, paper and pulp, desalination plants, oil & gas industries, etc. [2]. However, duplex stainless steels present poor machinability due to their high work hardening rate, and low thermal conductivity. Thus, the production of DSSs by additive manufacturing techniques is extremely promising [2, 48].

The number of research involving processing–microstructure–property relationship of DSSs produced by L-PBF has grown exponentially in the last five years [33, 39, 40, 48-64]. For L-PBF-produced DSSs in its as-built condition, an almost entirely δ-ferritic microstructure is found because of the high cooling rates of the process, in which there is not enough time for ferrite-to-austenite transformation to occur [26, 39, 50, 52-58]. Additionally, the potential loss of nitrogen (austenite stabilizer) by vaporization during processing negatively affects the γ-austenite formation [54, 57].

After a proper heat treatment, it is shown that a recrystallized microstructure consisting of austenite and ferrite is obtained, being nearly balanced depending on the applied time and temperature [40, 49, 51-54, 57, 58]. The high dislocation density present in the as-build DSSs parts is the main responsible for nucleation of new grains during heat treatment, in which γ-austenite mainly forms at the grain boundaries (GBs) of δ-ferrite grains [49, 57]. Micrographs of a DSS produced by L-PBF before and after heat treatment are shown in Fig. 2.3.

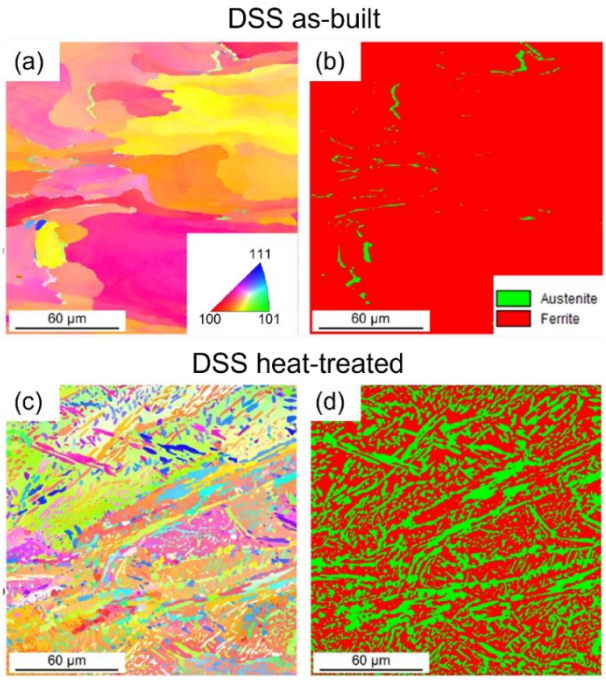

Figure 2.3 - Micrographs obtained by EBSD of a duplex stainless steel produced by LPBF. IPF and phase map of its (a, b) as built, and (c, d) heat-treated

conditions, respectively. Adapted and reprinted from [61] with permission from Elsevier.

Approaches to achieve a balanced dual-phase structure in DSSs produced by L-PBF without the need of applying a post heat-treatment have been recently carried out. The mixture of austenitic and superduplex stainless steel powders proved to be effective to promote the formation of austenite in the as-built state [59]. On the other hand, the attempt to obtain a dual-phase microstructure by producing the parts under a nitrogen atmosphere (austenite stabilizer) was unsuccessful [60].

Some works [33, 48, 49, 51, 54, 61] reported the presence of a large amount of nanometric rod-shaped Cr_2N nitrides within δ-ferrite grains and along grain boundaries (GBs) of a DSSs obtained by L-PBF. The formation of nitrides is ascribed to the supersaturation of N in the matrix, presence of high density of dislocations generated by the fast cooling, and complex thermal cycle induced by successive melting of overlaying powders layers. Depending on their size, distribution and chemical environment, Cr-depleted regions around the chromium-rich precipitates may be formed, serving as initiation sites for corrosion when the material is exposed to harsh environments. Moreover, Cr_2N precipitates may deteriorate ductility and impact toughness of alloys. However, heat treatments demonstrated to be effective to dissolve the Cr_2N nitrides nanoparticles [48, 54, 61].

Regarding mechanical properties, studies [33, 48, 49, 51, 52, 55, 57] demonstrate that, compared to their heat-treated condition, as-built L-PBF-produced DSSs (i.e., entirely ferritic) present higher strength and hardness, but lower ductility and impact toughness. This mechanical behavior is associated to a single ferritic phase, presence of Cr_2N nanoparticles, and large concentration of dislocations, which restricts further dislocation movement. The post heat treatments applied to restore the dual-phase microstructure, besides to dissolve the Cr_2N nanoparticles, also reduce the dislocation density, promoting a balanced tensile (relatively lower strength and higher ductility) and toughness properties, being similar to their wrought counterpart (e.g., SAF 2205).

In chloride media, given its highly supersaturated matrix, it is reported that as-built L-PBF-produced DSSs exhibit similar corrosion performance compared to their heat-treated L-PBF-produced condition and wrought counterpart [64]. However, as-build DSSs also present a low repassivation ability after a stable pit is formed and weak resistance to localized corrosion, being associated to the presence of a single ferritic phase, and high residual stress [39, 61]. After recovering the balanced austenite-ferrite microstructure and reducing the dislocation density by heat-treatment, the electrochemical behavior of DSSs is comparable to the SAF 2205 DSS [20, 39, 40, 61].

Although Cr_2N nanoparticles are ascribed to negatively affect the mechanical properties of the as-built DSSs [33, 48, 49, 51, 54, 61], it was shown that it has no influence on localized corrosion in chloride media since the depletion of Cr in the matrix of DSSs by the formation of Cr_2N is not critical [54, 61].

Therefore, for practical applications, both DSSs in as-built and/or heat-treated conditions exhibit interesting mechanical and electrochemical properties, opening the possibility of its application depending on the working environment.

2.4 Columnar-to-equiaxed transition and grain refinement in L-PBF

As previously shown in Section 2.2, metals and alloys obtained by L-PBF often exhibit a coarse columnar grain structure that can cross over several layers, leading to hot-cracking susceptibility and significant anisotropy. The typical large thermal gradients (G) and high cooling rates within small melt pools are responsible for epitaxial grain growth and, consequently, formation of coarse dendritic-columnar grain structures [35, 65]. Conversely, equiaxed grains may reduce the susceptibility to cracking, minimize the tendency to anisotropy, and increase strength and toughness [66], which is strongly desirable for many applications.

Pursuing enhanced properties, several strategies have been applied to partially or totally eliminate the columnar grain structure and induce the formation of refined equiaxed grains in different alloys produced by L-PBF [14-27], being the chemical composition design and the L-PBF processing parameters

paramount for the microstructural tailoring. To illustrate the grain refinement effect in L-PBF-produced alloys, Fig. 2.4 shows micrographs of an austenitic stainless steel with addition of boron.

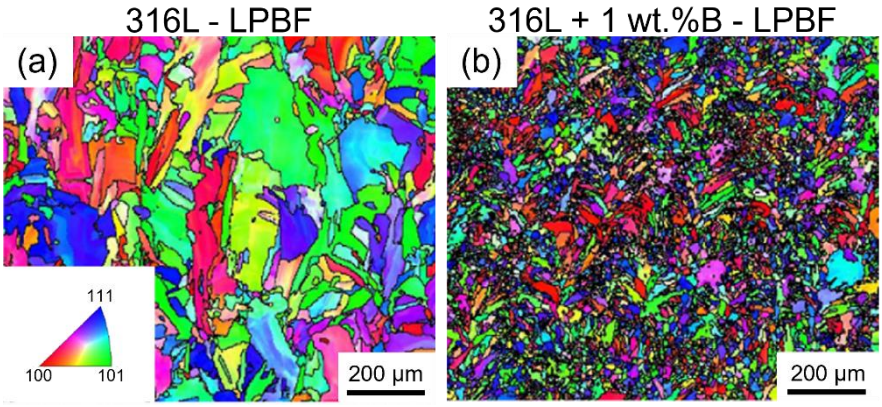

Figure 2.4 - Micrographs obtained by EBSD of a 316L+B produced by L-PBF. IPF of (a) pure 316L, and (b) 316L + 1 wt.% of B (mechanical mixing). Adapted from [26] (CC BY-NC-ND 4.0 DEED).

According to the classical solidification theories [44], to promote the formation of equiaxed grains, it is necessary to activate nucleation ahead of the growing S/L interface by sufficient undercooling that, therefore, prevents the further crystal growth. By reducing the G/R ratio in the melt pool, it is possible to improve the nucleation rate and, consequently, contribute to the formation of equiaxed grain morphology. However, as extensively reported in literature [16, 17, 21, 33, 48, 49, 51, 52, 55], refined and equiaxed grains are hardly formed in alloys produced by L-PBF since G is very high [22].

A few studies [14, 15, 18] reported the production of stainless steels with refined grain structure by exclusively adjusting the L-PBF-processing parameters (i.e., reducing the thermal gradient and/or increasing the cooling rate). However, as expected, this strategy has not demonstrated a high effectiveness in promoting a homogeneous equiaxed grain structure throughout the entire L-PBF-printed component, in which normally the bottom of the melt pools still solidifies epitaxially and presents columnar grains [17]. Moreover, for practical applications (e.g., components with complex geometries and/or large dimension), it is a

challenge to reach grain refinement by uniquely controlling processing parameters since there are variations of the heat accumulation and conduction behavior [21].

On the other hand, widely studied for different alloys system, equiaxed morphology and grain refinement can be successfully obtained by introducing potent inoculant particles (externally added or formed in-situ) with small atomic mismatch with the matrix, to promote heterogeneous nucleation at small critical nucleation undercooling (ΔT_n) [16-21].

It is reported that the addition of Ti inoculant has proven to be effective to promote grain refinement in ferritic stainless steels (FSSs) produced by L-PBF [16, 18. 19, 21], in which the grain refinement is ascribed to the in-situ formation of micro- and nanosized particles of TiN [16, 21], and TiO [17-19] that serves as heterogeneous nucleation sites for ferrite during solidification. Lower content of Ti (~0.3 – 0.8 wt.%) leads to a columnar-to-equiaxed transition within each melt pool, wherein there is a mixture of columnar and equiaxed grains in each melt pool [16, 18]. Alternatively, increasing Ti content (~5 wt.%), a homogeneous grain refinement and texture-free microstructure is observed [19, 20]. Expectedly, as predicted by the Hall-Petch relationship and in addition to solid solution strengthening by Ti, the grain refinement is responsible for increasing hardness [17] and tensile strength [18, 19] of FSSs, besides slightly reducing ductility when compared to their wrought counterpart.

A L-PBF-produced ultrafine DSS with outstanding tensile properties was obtained by introduction of TiC inoculant. The formation of refined equiaxed grains is ascribed to the in-situ formation of TiC_xN_y nanoparticles within and along GBs, which decrease ΔT_n and promote heterogeneous nucleation of δ-ferrite grains, as well as promote Zener pinning effect to restrict grain growth [20].

Besides adjusting L-PBF processing parameters and/or adding potent inoculants [14-18, 20, 21], the design of alloys with adequate solutes showed to be effective in promote nucleation and, consequently, high grain refining efficiency in alloys obtained by L-PBF [22-27].

It is well known that in conventional casting the addition of proper solutes into molten metal limits the grain growth by nucleation in the constitutional

undercooling (CS) zone created by solutes segregation. On the other hand, during L-PBF solidification, the role of solute in grain refinement cannot be directly related to the classic grain growth restriction theory (Q value) used to explain grain refinement in alloys produced by casting, in which solutes with high Q (grain growth restriction) values quickly create constitutional undercooling (ΔT_{CS}) ahead of the S/L interface, promoting grain refinement. Opposing to casting, the constitutional undercooling zone generated by the solute segregation is partially or totally eliminated by the large thermal gradient (G) during L-PBF solidification [23, 24].

Recent works [22, 23, 27] showed that, although the grain refinement is improved increasing the Q value for L-PBF-produced alloys, there is no linear relationship between the grain size reduction and Q value, since the growth restriction effect of the solutes is weakened by the large thermal gradient during L-PBF. As the constitutional undercooling insufficiently contribute to the total undercooling required for nucleation, it was verified that [23], at high cooling rates in L-PBF process, a time lag in dendrite growth is caused by solute rejection during solidification, and this difference between the theoretical solidification rate (associated to the L-PBF parameters and material's properties) and the actual dendrite growth is responsible for creating a large thermal undercooling ahead of the S/L interface. Therefore, it is shown that for grain refinement caused by solute effect in L-PBF, the thermal supercooling (ΔT_t) contributes more than the constitutional undercooling (ΔT_{cs}) to the necessary undercooling (ΔT) for nucleation, resulting in the formation of numerous nuclei and, consequently, reducing grain size.

Grain refinement caused by solute effect was reported for different alloys system produced by L-PBF (e.g., Mo-B, Mo-C, Al-Cu, Al-Si, Al-Ni, Fe-B) [22, 23, 25-27], wherein it is proposed that increasing the solute concentration, a higher content of solute segregate ahead of the solidification front, resulting in an increasing of the grain refining efficiency by the improvement of the growth restriction effect and grain growth lag. Moreover, compared to their columnar grain structure condition (i.e., alloy without addition of adequate solute), an

enhancement of the tensile strength and hardness by the grain refinement is also reported, without extremely impairing the ductility [25-27].

Therefore, by the aforementioned strategies, it can be seen that grain refinement is one of the most efficient approaches to improve mechanical properties. Besides, it minimizes texture/anisotropy and hot-cracking susceptibility of alloys obtained by L-PBF.

3 OBJECTIVES

To the best of my knowledge, there are no studies regarding the production and characterization of L-PBF-produced boron-modified stainless steels using pre-alloyed powders, which is of great scientific and industrial interest. Therefore, based on the knowledge gap found in the literature, the following objectives are proposed:

i. Produce dense and crack-free parts of a boron-modified duplex stainless steel by L-PBF using a pre-alloyed powder (i.e., borides present within the matrix of DSS powder).

ii. Understand the solidification mechanism during L-PBF process, especially with regard to the boron effect on grain refinement.

iii. Evaluate the electrochemical behavior in chloride media and the wear resistance in sliding condition of the L-PBF-produced alloy.

4 EXPERIMENTAL PROCEDURES

4.1 Feedstock powders

Two metallic powders were used in this work. Gas-atomized commercial DSS powder was supplied by Metalpine GmbH's, and a gas-atomized hypereutectic boron-modified DSS powder. Although only hypoeutectic boron-modified DSSs were chosen to be produce by L-PBF, a hypereutectic boron-modified DSS powder (i.e., higher boron content) served as a precursor to obtain a variety of hypoeutectic boron-modified DSS compositions by mechanical powder mixing (sometimes also referenced as `*in situ* alloying' [67]). In detail, two hypoeutectic boron-modified DSS powders were used to produce parts by L-PBF, containing 0.3 and 0.6 wt.% of boron (named as P0.3B and P0.6B, respectively). These hypoeutectic compositions were achieved by mechanically mixing two different powders: (i) hypereutectic DSS modified with 1.2 wt.% of boron (P1.2B), and (ii) non-modified DSS commercial alloy (PDSS).

The chemical composition of the powders can be seen in Table 4.1, being measured by optical emission spectroscopy (OES), except the boron content, which was measured by atomic absorption spectroscopy (AAS).

Table 4.1 - Chemical composition (wt.%) of the powders used in this study.

Powder	B	Cr	Mo	Ni	Si	Mn	C	N	Fe
P1.2B	1.2	24.9	3.2	4.9	0.6	1.3	0.02	0.1	Bal.
PDSS	-	22.0	2.9	5.4	1.3	1.0	0.02	0.1	Bal.
P0.3B[1]	0.3	22.7	3.3	5.2	0.4	0.7	0.02	0.1	Bal.
P0.6B[1]	0.6	23.4	3.2	5.1	0.5	0.9	0.02	0.1	Bal.

[1] Nominal chemical composition.

Figure 4.1 shows an isopleth diagram calculated by Thermo-Calc software for DSS in function of boron content. Despite the powders mixture, a complete and homogeneous melting of the powders is expected during further L-PBF process, resulting in the formation of hypoeutectic compositions in the molten metal.

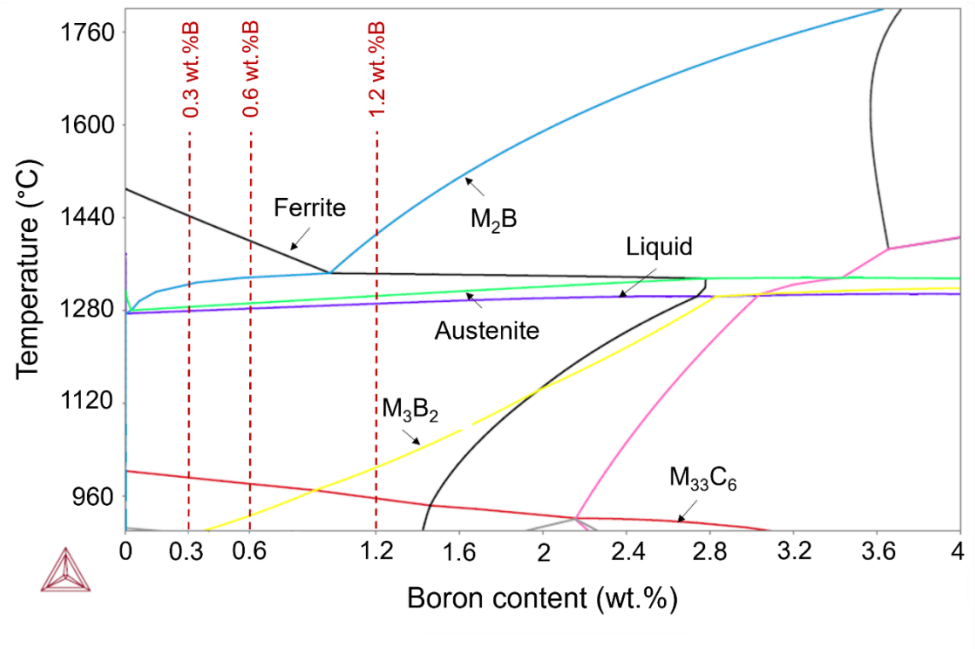

Figure 4.1 - Isopleth of a duplex stainless steel modified with different content of boron. The compositions of 0.3, 0.6, and 1.2 wt.% of B are highlighted in the graphic.

It is important to highlight that pre-alloyed boron-modified stainless steels are not commercially available. Therefore, a SAF 2205 DSS master alloy (Outokumpu, Sweden) and Fe-B, Ni, and Cr (ACL Metais, Brazil) commercially pure elements (>95.5%) were used as precursors to produce ingots of the hypereutectic boron-modified DSS. The master alloy and precursors were melted using a Power-trak 50-30R induction furnace and cast into a graphite mold. After cooling to room temperature, mechanical grinding was performed to remove the oxide layer present on the ingot surface.

The boron-modified stainless-steel ingots were subsequently atomized using a PSI HERMIGA 75/5VI gas atomizer (Phoenix Scientific Industries Ltd, England). The gas atomization parameters are detailed in Table 4.2.

Table 4.2 - Parameters used for production of hypereutectic boron-modified DSS powder by gas atomization.

Gas	Pressure (bar)	Pouring temperature (K)	Nozzle diameter (mm)	Gas-to-metal ratio	Crucible
Ar	40	1923	2.5	0.22	Al_2O_3

Commercial DSS and hypereutectic boron-modified DSS powders were sieved according to ASTM B214 [68], in which particles sizes lower than 63 μm were considered to further processing by L-PBF.

Thus, P1.2B and PDSS powders were mixed together to attain a composite mixture of 0.3 and 0.6 wt.% of boron. A high precision scale was used to weigh the powders before mixing. The mixing process was performed using a self-built mixer system, in which the powders are placed in a container and the powder mixing occurs by rotating the system in one direction at 60 rpm for 2 hours.

4.2 Laser powder bed fusion process (L-PBF), design of experiments (DoE) and analysis of Variance (ANOVA)

Three alloys were subjected to production by L-PBF, as follows: commercial DSS, and DSS modified with 0.3 and 0.6 wt.% of boron, named as ‘Pure-LPBF’, ‘0.3B-LPBF’, and ‘0.6B-LPBF’. The experiments were carried out using an ORLAS Creator (Coherent CREATOR RA, Germany) L-PBF machine equipped with an ytterbium-doped fiber laser (1070 nm) [69]. During printing, the oxygen level was controlled below 0.1% under argon atmosphere for preventing alloy’s oxidation and the AISI 1020 building substrate was not preheated. Cubic specimens with dimensions of 10 × 10 × 10 mm were produced based on current procedures described the literature [70], being connected to the building substrate by small support structures. All the printed specimens were measured and tested in the as-built condition, i.e., without post-processing or post-heat treatment.

Box-Behnken design was used to optimize the L-PBF-processing parameters for each alloy. A 3-factor Box-Behnken design consists of midpoints

(minimum and maximum values) and center points corresponding to −1, +1, and 0, respectively. The center points allow the estimation of quadratic effects in the target response. Therefore, laser power, scanning speed, and hatching distance were chosen as the input variables (see Table 4.3), being porosity the studied response. For all experiments, it was used a bidirectional scanning strategy with a 67° of rotation between layers; the powder layer thickness and laser beam diameter were set in 25 and 40 µm, respectively. Moreover, random experiments were performed as additional data to validate the adjusted ANOVA statistical models (see Appendix A, Tables A.2, A.3, and A.4).

Table 4.3 – L-PBF parameters and processing levels established for Box-Behnken analysis.

	Levels		
Factors	**Minimum value (-)**	**Central point (0)**	**Maximum value (+)**
Laser power (W)	150	200	250
Scanning speed (mm/s)	600	900	1200
Hatching (µm)	30	60	90

The main objective of this DoE-ANOVA investigation was to ensure the absence of cracks and delamination in the as-built L-PBF-produced cubic specimens; therefore, porosity was the only response of the system considered in this evaluation.

Porosity was measured using ImageJ software from analysis of binarized optical micrographs with magnification of 50x (~10-15 images per specimen). For this purpose, the specimens were cut out of the additively manufactured cubes, ground and polished according to standard procedures for metallographic analysis, i.e., grinding sequence of 240, 320, 400, 600, 800, 1200, and 2000 grit SiC paper followed by polishing using diamond suspension of 3 µm and 1 µm, and colloidal silica suspension of 0.05 µm.

The experimental planning and the analysis of variance (ANOVA) were carried out using Minitab software (Minitab, USA). The detailed experiments can be seen in Appendix A, Table A.1. The response surface methodology (RSM)

was used to identify the optimum process window and obtain minimum porosity percentage. Based on RSM and ANOVA, quadratic models were obtained, being expressed by a second-degree polynomial (Equation 4.1) [37]. Y is the predicted response, β_0, β_i, β_{ii}, and β_{ij} represent the coefficients of regression for the intercept, linear, square and interaction terms, respectively. X_i, and X_j are the coded values of the independent variables (input factors) [37].

$$Y = \beta_0 + \sum_{i=1}^{3} \beta_i \ X_i + \sum_{i=1}^{3} \beta_{ii} \ X_i^2 + \sum_{i=1}^{2} \sum_{j=i+1}^{3} \beta_{ij} X_i X_j \quad \text{(Eq. 4.1)}$$

Ultimately, Fig. 4.2 illustrates the experimental steps from gas-atomization to L-PBF process.

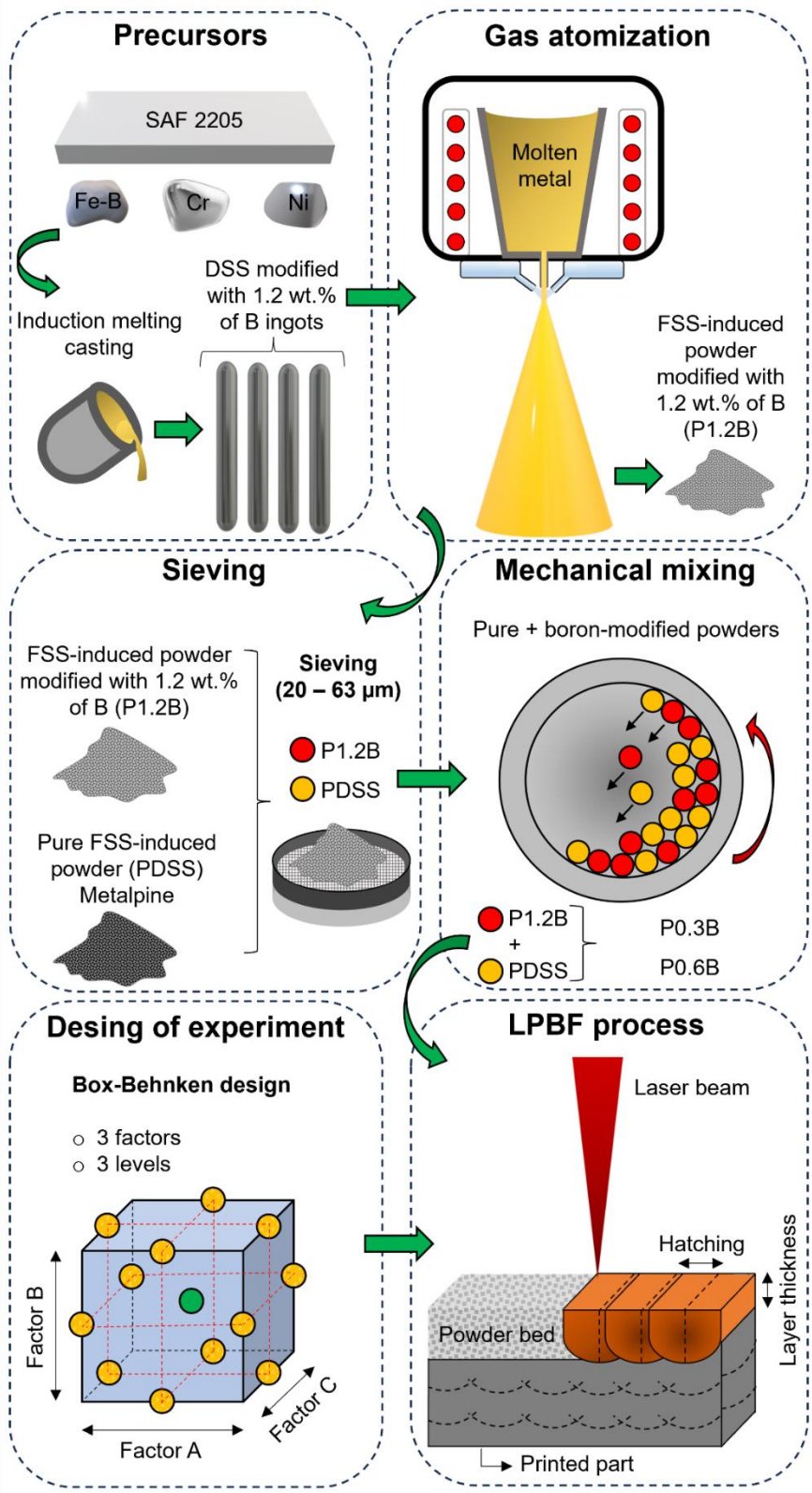

Figure 4.2 - Illustration of the processing steps from the precursors up to the production of the 3D-printed specimens. The high cooling rate of gas-atomization induces the formation of a FSS powder from DSS. Illustrations not to scale.

4.3 Microstructural characterization

Specimens were prepared according to standard procedures for metallographic analysis already described in Section 4.2. For SEM and EBSD analysis, the samples were cut off from the center of the perpendicular and parallel cube planes (see Fig. 4.3a). For TEM analysis, the samples were taken from the center of the perpendicular planes. The microstructures were characterized using a Axio optical microscope (ZEISS, Germany), a MIRA-TESCAN FEG (TESCAN, Czech Republic) scanning electron microscope (SEM) coupled with energy-dispersive X-ray spectroscopy (EDX) and electron back-scattered diffraction (EBSD), a FEI TECNAI G^2 F20-FEG (FEI, USA) transmission electron microscope (TEM), a FEI TECNAI 52 S-TWIN-LaB_6 (FEI, USA) transmission electron microscope (TEM) equipped with the ASTAR/DigiSTAR, NanoMEGAS system, and an Olympus LEXT OLS4000 (Olympus, Japan) confocal laser scanning microscopy (CLSM). Moreover, X-ray diffraction (XRD) analyses were performed using a Bruker D8 Advance ECO Bruker (Bruker, Germany) equipment with Cu radiation coupled with a high-speed detector SSD160.

For comparison purposes, a commercial SAF 2205 DSS subjected to hot-rolling, and heat-treated at 1373 K followed by water quenching, hereinafter named as ‘SAF 2205-hot rolled’, was subjected to the same following procedures to assess its microstructural, electrochemical and tribological features. Chemical composition of the SAF 2205-hot rolled obtained by optical emission spectroscopy (in wt.%): 0.026 C, 0.47 Si, 1.26 Mn, 0.028P, 22.02 Cr, 5.37 Ni, 2.89 Mo, 0.25 Cu, Fe bal.

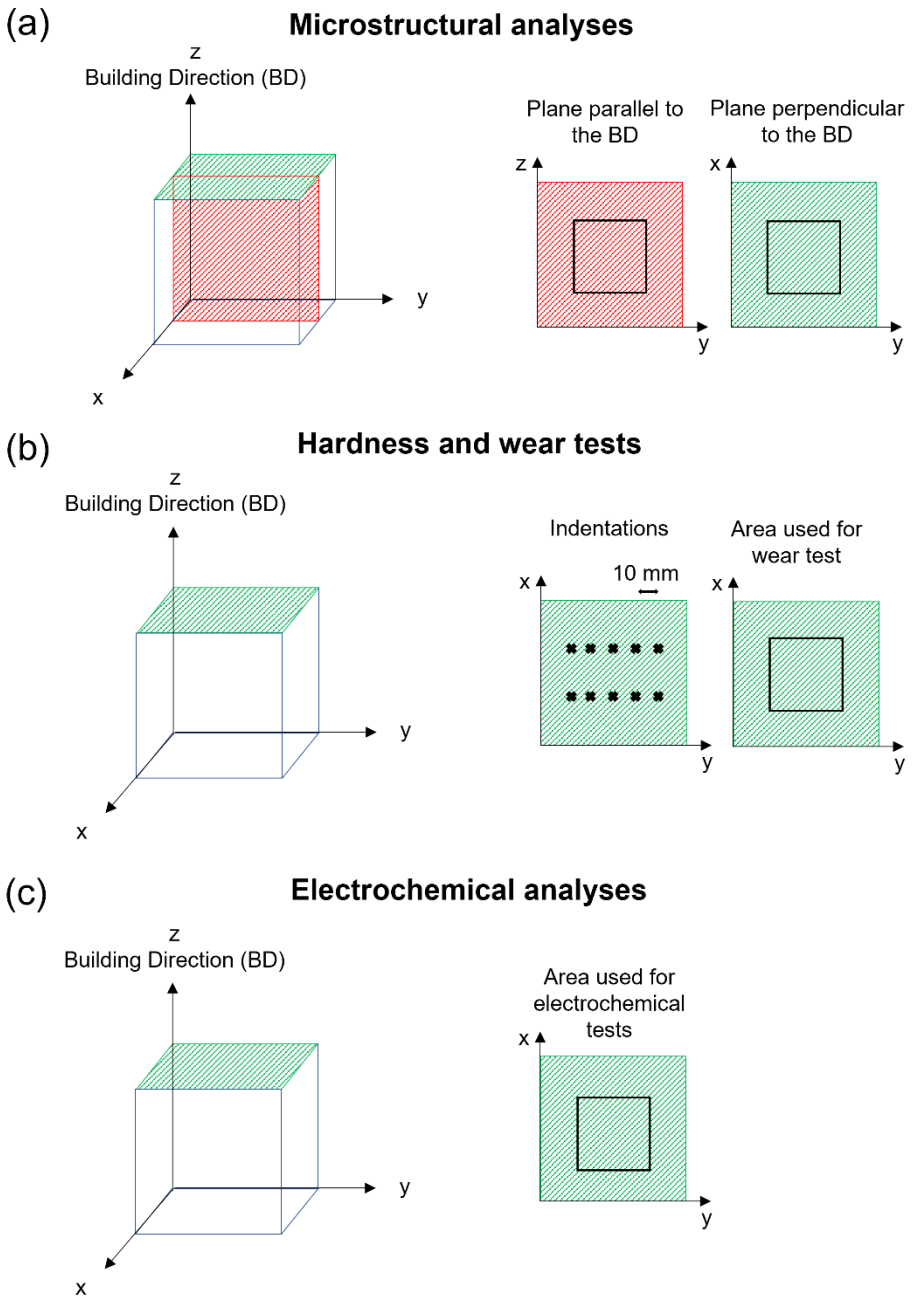

Figure 4.3 - Definition of the different planes in the 3D-printed specimens which were used to perform (a) microstructural (b) hardness and wear, and (c) electrochemical analyses.

4.4 Hardness and wear resistance characterization

Using a HMV Vickers microhardness tester (SHIMADZU, Japan), microhardness was measured with 10 indentations per specimen, 500 gf load and 15 s of dwell time, according to the ASTM E384 standard [71]. To measure

the specific wear rate, a reciprocating pin-on-plate test using a Plint & Partners equipment (Plint & Partners Ltd., England), TE 67/R and Al_2O_3 (2.7 mm of nominal diameter), was performed in triplicate based on the ASTM G133 standard [72]. The normal force, stroke length, sliding distance, oscillation frequency, wear time, temperature and relative humidity were 25 N, 10 mm, 100 m, 5 Hz, 16 min and 40 s, 295 ± 3 K and 55%, respectively. Vickers and wear tests were evaluated at the plane perpendicular to the building direction of the specimens (see Fig. 4.3b).

4.5 Electrochemical behavior characterization

Before electrochemical tests, the specimens were ground using the grinding sequence of 240, 320, 400, 600, 800, 1200, 2000 grit SiC paper and then polished using 1-µm alumina suspension. Finally, all specimens were cleaned with acetone.

All electrochemical measurements were performed in triplicate to ensure repeatability. Considering a three-electrode cell configuration in a Gamry 600 + potentiostat (Gamry Instruments, USA), in which a saturated calomel electrode (SCE) was used as reference, along with a platinum sheet as counter-electrode, and the L-PBF and hot rolled specimens as working-electrodes.

For cyclic potentiodynamic polarization (CPP) and electrochemical impedance spectroscopy (EIS) tests, a 0.6 M NaCl solution was used as electrolyte, which was prepared using high purity NaCl (>99%) and demineralized water. The working-electrodes had a surface area of 0.3 cm^2 exposed to the electrolyte during tests. The electrochemical procedure considered in this work was based on the recent literature on the electrochemical behavior of duplex and super duplex stainless steels produced by L-PBF [14, 56].

Prior to any CPP test, the working electrode was left at open circuit potential (OCP) for 1 h, in order to allow the stabilization of the potential at rest. Potentiodynamic polarization test was performed from − 250 mV regarding the OCP until a current density of 10^{-3} A/cm² was reached, using a 1 mV/s scan rate. An estimation of the corrosion current density (i_{corr}) was obtained by extrapolating the cathodic region, which displayed a “Tafel-like” behavior [73].

For EIS tests, a frequency ranges from 10^5 Hz to 10^{-2} Hz (10 points/decade) with an alternating current (AC) perturbation potential of 10 mV_{rms} around the OCP was used. The analyzes of the EIS data were modelled by EC-Lab software (BioLogic®, France) considering electrical circuit (EC) analog approach.

Finally, the degree of sensitization (DOS) of the specimens was also evaluated, thus double-loop electrochemical potentiokinetic reactivation (DL-EPR) tests using an electrolyte of 0.5 M H_2SO_4 + 0.01 M KSCN + 0.5 M NaCl diluted in 1000 ml of water were performed, considering an exposed area of 0.3 cm^2. A potential scan from − 0.05 V vs. OCP (initial and final potential) to 0.3 V vs. OCP (maximum potential) was utilized, being the forward and reserve scan rate 10 mV/min. The ratio (I_r/I_a, in %) of reactivation current (I_r) and activation current (I_a) was considered as an index of the degree of sensitization according to the ISO 12732 [74], where: Ir/Ia< 1%, Ir/Ia> 5%, and 1%< Ir/Ia< 5% are considered as unsensitized, sensitized, and slightly sensitized, respectively. The electrochemical analyses were performed at the plane perpendicular to the building direction of the specimens (see Fig. 4.3c).

5 RESULTS AND DISCUSSION

5.1 Feedstock powders

This section is focused on the structural analysis of the gas-atomized powders used to produce the alloys by L-PBF.

Figure 5.1 shows structural features of the feedstock powders. As expected, the XRD patterns in Fig. 5.1a show that both gas-atomized powders exhibit a completely δ-ferritic structure. It is well described that the γ-austenite formation is suppressed in duplex/superduplex stainless steels submitted to rapid solidification processes [51, 52, 56, 75-77], such as gas atomization (10^2 –10^6 $K \cdot s^{-1}$ [78]). For DSS modified with 1.2 wt.% of boron, low intensity peaks of the M_2B-type boride (M = Fe, Cr) are also observed, which can be seen in the in inset picture of the XRD pattern present in Fig. 5.1a. It must be emphasized that the low intensity of the boride's peaks on XRD patterns are associated to peak overlaps and the low structure factor of borides.

Near-spherical and smooth surfaces illustrate the particles with size <63 μm, as can be seen in Figs. 5.1b-d. A low amount of attached small particles (satellites) on the surface of larger particles is observed, attributed to the turbulent flow in the atomization chamber, which results in collisions and welding between large and small droplets [78, 79].

A cross-sectional micrograph in Fig. 5.1e shows that P1.2B powder presents a refined microstructure composed of a δ-ferritic matrix and fine primary needle-like borides with random orientations (length and width of 0.9 $\pm$ 0.3 μm and 0.1 $\pm$ 0.03 μm, respectively), which may indicate the high nucleation rate due to the solidification at high undercooling [31]. From thermodynamic calculations [Fig. 4.1], with cooling of the DSS modified with 1.2 wt.% of boron, M_2B boride is the first phase to form from the liquidus, followed by δ-ferrite. Also, the microstructural refinement is related to the high cooling rates associated to gas atomization [78].

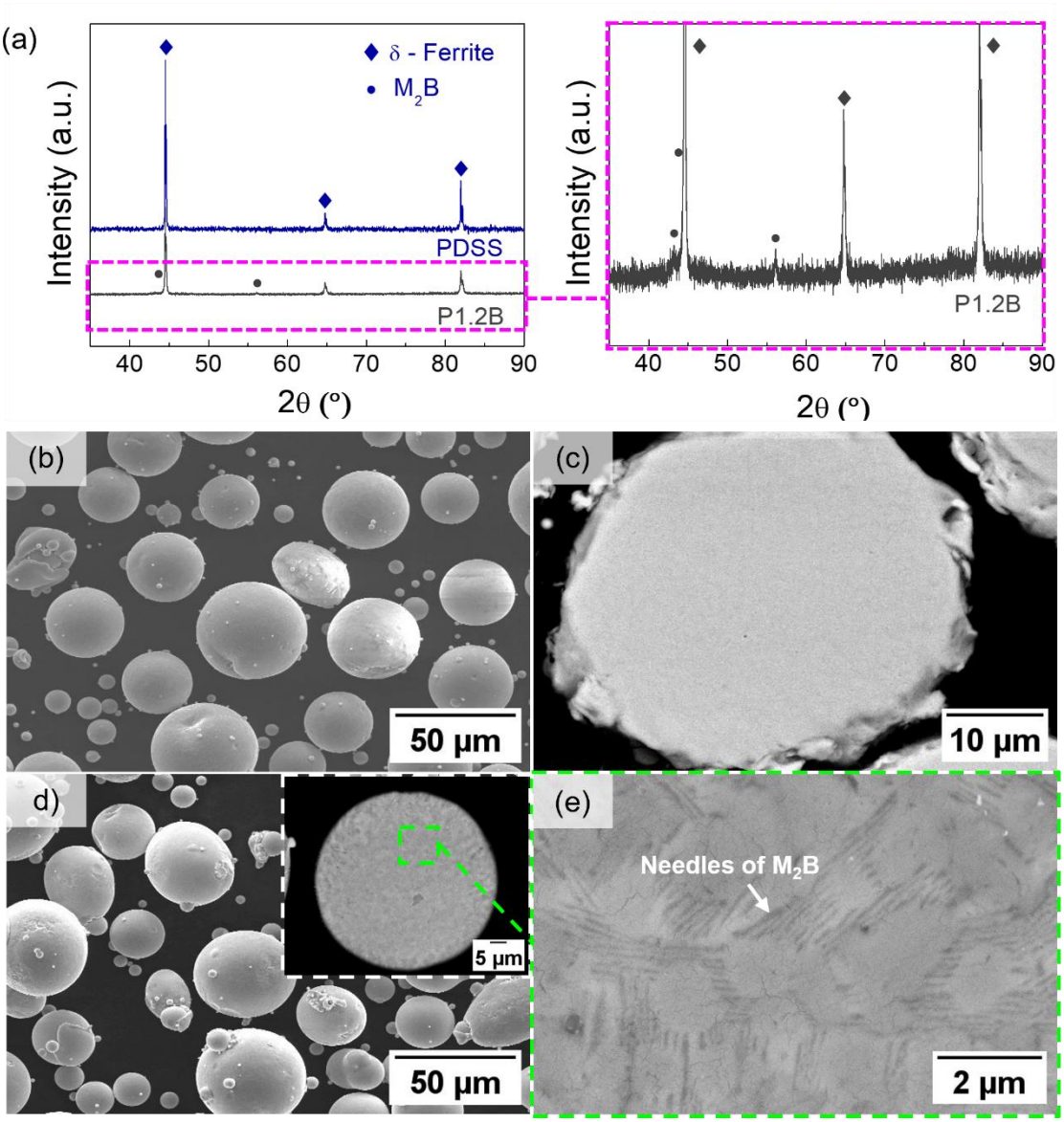

Figure 5.1 - Structural data of the gas-atomized feedstock powders before mechanical mixing: XRD patterns of the (a) pure (PDSS) and boron-modified (P1.2B) powders (zoom to show in details the peaks of M_2B for the P1.2B), and SEM micrographs of the (b, c) PDSS, and (d, e) P1.2B powders.

5.2 Laser powder bed fusion process – DoE/ANOVA

This section focuses on evaluating and verifying the reliability and effectiveness of the adjusted models used to optimize the L-PBF-processing parameters for the studied alloys.

Specimens were successfully produced using the L-PBF processing parameters listed in Table 4.3, cracks or delamination were not visually detected. Cubic specimens on the building substrate can be seen in Fig. 5.2a.

As previously highlighted, the boron-modified (0.3 and 0.6 wt.% of boron) and unmodified (pure) DSS produced by L-PBF were investigated in their as-built condition, named as “0.3B-LPBF”, “0.6B-LPBF”, and “Pure-LPBF”, respectively. Micrographs in Figs. 5.2b-d show the presence of irregularly shaped defects for the specimens produced using low laser power values (150 and 200 W), indicating the presence of lack-of-fusion defect caused by insufficient fusion of the material during processing. On the other hand, only small circular gas pores (which are presumably attributed to trapped gas or alloy element evaporation) as well as the lowest porosity values, can be seen for the specimens produced using the highest laser power (i.e., 250 W). Likewise, for different laser power values, the porosity percentage decreases as the scanning speed is reduced. It is reported that low energy densities are associated to lack-of-fusion defects, which may be minimized by increasing laser power or reducing scanning speed [15].

It is known that the pores formation is affected by the features of the melt pool, which is associated to the L-PBF parameters, material properties, powder particles features, etc.. Overall, the combination of high laser power and low scanning speed (i.e., high energy density) can lead to a highly fluctuated molten pool with keyhole-like effect by material evaporation [75]. On the other hand, low laser power simultaneously with high scanning speed (i.e., low energy density) can cause insufficient energy, often resulting in high surface tension, unmelted powder, and poor wetting of molten pool [75].

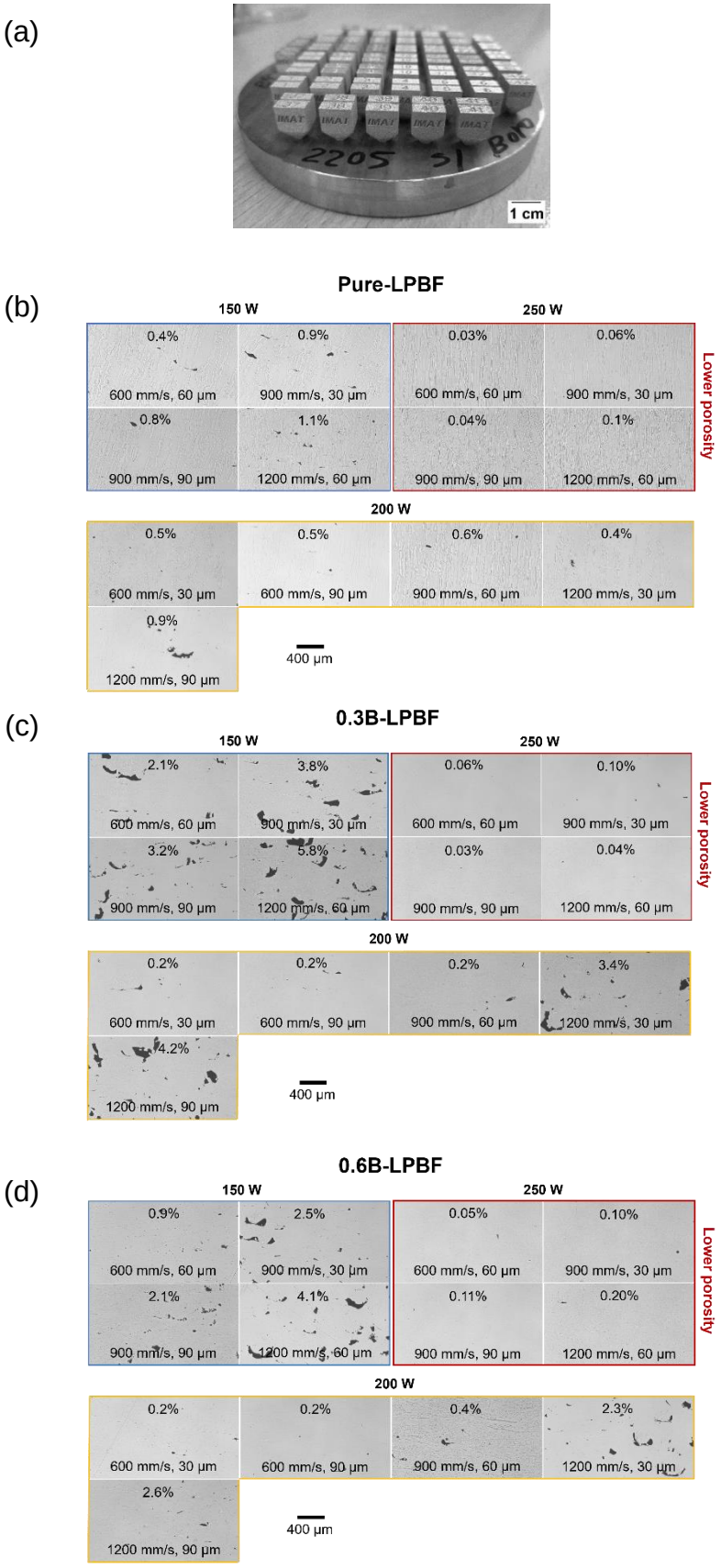

Figure 5.2 - Characterization of the L-PBF-produced specimens. (a) Specimens

on the substrate, and optical micrographs from the plane parallel to the BD of the (b) Pure-LPBF, (c) 0.3B-LPBF, and (d) 0.6B-LPBF alloys produced under different processing parameters. Porosity level and L-PBF parameters are shown in the micrographs.

The measured porosity for the L-PBF-printed specimens, as well as the L-PBF-processing parameters can be found in Appendix A, Tables A.2, A.3, and A.4.

The ANOVA results for the RSM models as well as the significance of main effects, interactions and quadratic terms are present in Appendix A, Tables A.5, A.6 and A.7. The F-value and P-value indicate how well the observed data fit the proposed model, ideally being greater than 4 and less than 0.05, respectively [80]. Thus, it is noteworthy that the processing parameters and/or interactions with P-value lower than 0.05 are significant within the experimental studied domain, as they have a confidence level of 95%.

Therefore, from the data in Tables A.6 and A7, it can be observed that the relevant parameters and interactions are similar for the alloys containing 0.3 and 0.6 wt.% of boron, being: P, V, P×P, V×V and P×V. The relevant processing parameters and interactions for the pure DSS (Table A.5) are similar to those presented for the boron-modified alloys, except for the V×V and P×V interactions, in which P-values are close to 0.05, being disregarded from the model. Furthermore, for the tested conditions, it can be seen that hatching did not significantly influence the porosity percentage, being also disregarded. Based on these results, quadratic RSM models were fitted for the Pure-LPBF, 0.3B-LPBF, and 0.6B-LPBF alloys, which are expressed by the following equations 5.1, 5.2 and 5.3, respectively.

$$Porosity = -0.561 + 0.01491 \times P + 0.0000483 \times V - 0.000056 \times P \times P \quad (5.1)$$

$$Porosity = 14.14 - 0.1058 \times P - 0.00290 \times V + 0.000312 \times P \times P + 0.000011 \times V \times V - 0.000062 \times P \times V \quad (5.2)$$

$$Porosity = 6.49 - 0.0555 \times P + 0.00078 \times V + 0.000197 \times P \times P + 0.000007 \times V \times V - 0.000051 \times P \times V \quad (5.3)$$

The proposed models demonstrated to be adequate to determine the porosity percentage for the studied alloys, since the coefficient of determination (R^2) for the models are 0.81, 0.90 and 0.93 for the Pure-LPBF, 0.3B-LPBF, and 0.6B-LPBF specimens, respectively. Therefore, in Tables A.2, A.3, and A4 it can also be seen a high correlation between the experimental and predicted porosity values, in which the predicted porosity values were obtained from the equations 5.1, 5.2, and 5.3.

The models fit were further validated through additional specimens produced using random processing parameters (Tables A.2, A.3, and A.4), which are presented in “experimental versus predicted” porosity response comparison graphs, as can be seen in Fig. 5.3. For the three alloys, the points are distributed along a straight line and within the confidence and prediction intervals, suggesting that the models were satisfactory to accurately predicting the porosity response within the selected design space.

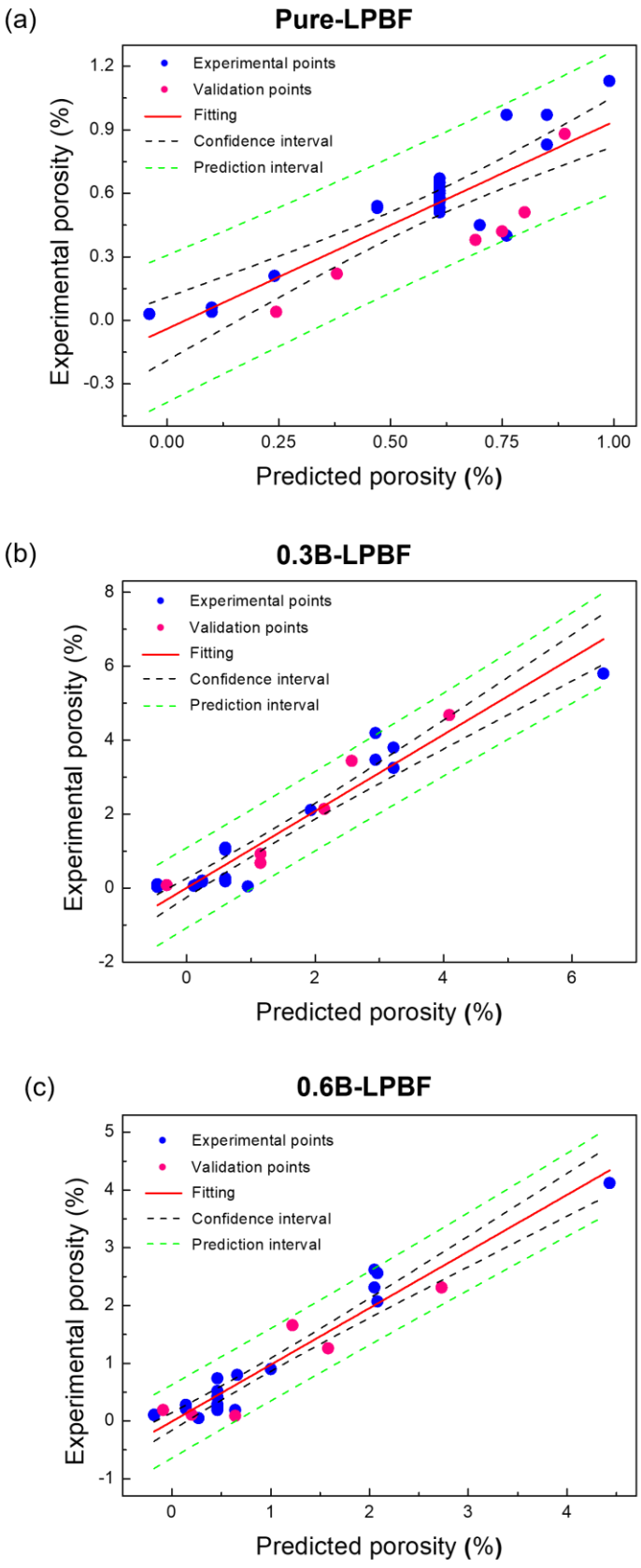

Figure 5.3 - Experimental versus predicted porosity response graphs obtained by

linear regression showing the relationship between experimental and predicted porosity for the (a) Pure-LPBF, (b) 0.3B-LPBF, and (c) 0.6B-LPBF specimens. Confidence and prediction intervals of 95%. R^2 greater than 73%, 91%, 92% (linear regression) for the Pure-LPBF, 0.3B-LPBF, and 0.6B-LPBF alloys, respectively.

The response surfaces for laser power and scanning speed are shown in Figure 5.4. It can be seen that the porosity percentage decreases as the laser power value increases, which seems to be the factor that presents the greatest contribution for the densification. In the tested conditions, lower laser power and higher scanning speed values lead to lack-of-fusion pores, as shown in Figs. 5.2b-d. Increasing laser power while decreasing the scan speed indicates a reducing trend in the porosity. Thus, for the studied alloys, at maximum laser power (250 W), it is possible to obtain a very low porosity percentage (close to 0.02 – 0.04 %vol.) using a relatively large range of scanning speed (600 to ~1000 mm/s).

It was shown in previous studies that the relative density of DSS produced by L-PBF is significantly influenced by the scanning speed [15, 75] and laser power [15], in which low laser powers combined to high scan speeds or high laser powers coupled with low scan speeds increase the porosity percentage.

The volumetric energy density (VED) (see Appendix A, Figure A.1, values obtained by Equation 4.1, Section 4.2) is utilized to determine a suitable combination of L-PBF parameters for different alloys, representing the amount of laser energy transferred to per unit volume of laser-irradiated powders [63]. For the boron-modified alloys, the porosity percentage decreases as VED increases, except for ~230 J/mm^3, which the porosity response does not follow this trend. At laser power of 250 W, regardless of the corresponding VED value, the porosity of the specimens remains below 0.1%. It indicates that, for the studied conditions, laser power of 250 W ensures a low porosity value regardless of the scanning speed and hatching distance. Moreover, the solely use of VED to determine the optimal L-PBF-processing range for the studied alloys may be limited, since the effect of individual parameters on the solidification process is not considered

where similar values of VED lead to different porosity percentage. Other works [63, 81, 82] also reported that VED cannot clearly predict the porosity due to the absence in evaluating the effect of the separate parameters on the dynamic of the melt pool, in which, for some alloys, it was not observed a clear relationship between VED and porosity, since same values of VED may lead to different porosity percentage and pore type [63].

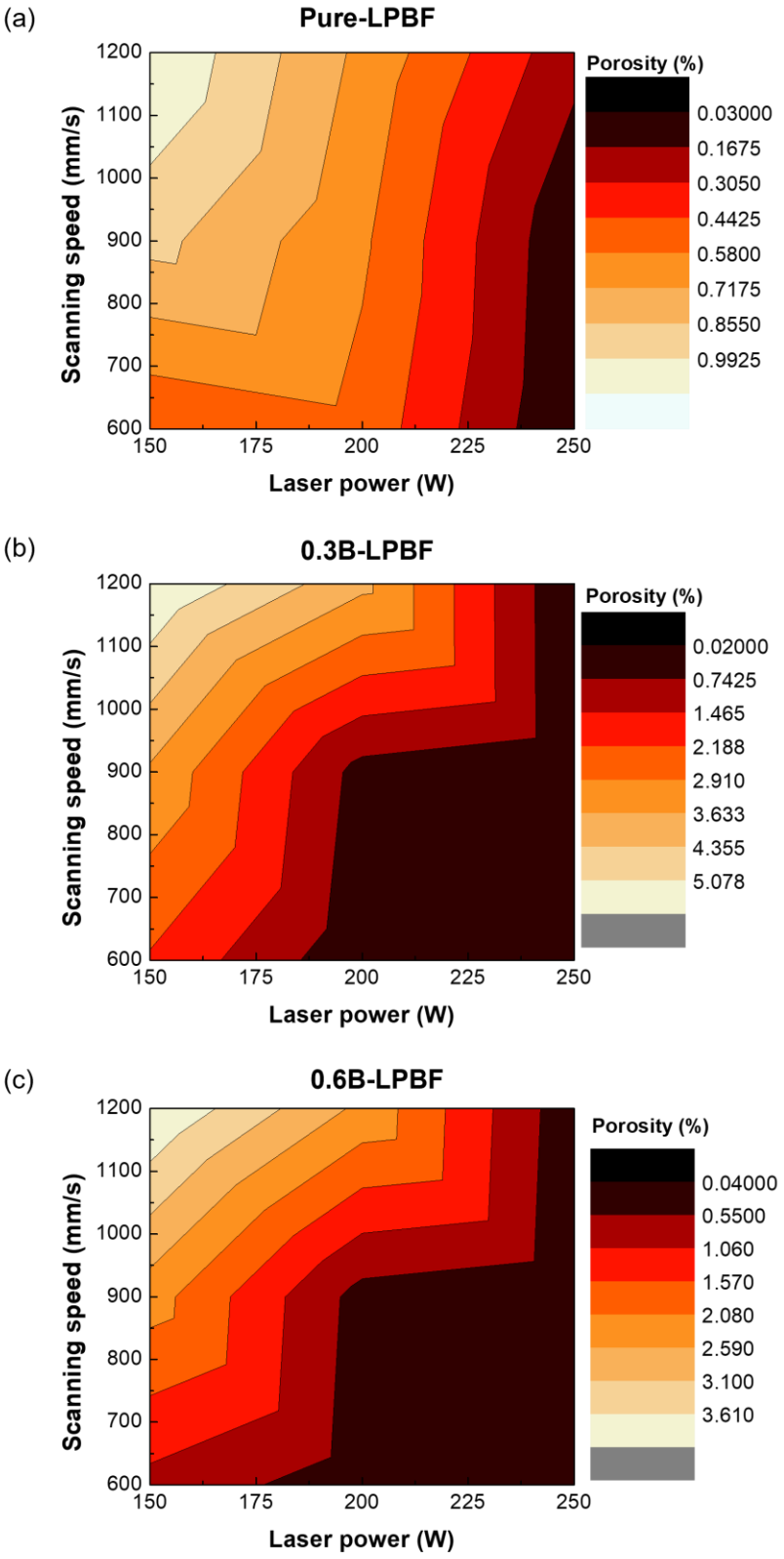

Figure 5.4 - Porosity response surfaces for the interactions between laser power and scanning speed for the (a) Pure-LPBF, (b) 0.3B-LPBF, and (c) 0.6B-LPBF alloys.

Based on analyzes from the model data's carried out using ANOVA, and aiming to obtain specimens with minimum porosity percentage, the optimized L-PBF-processing parameters were generated by Minitab and are shown in Table A.8 (Appendix A).

As previously mentioned, although the models indicate that the hatching does not significantly affects the porosity percentage of the studied alloys, specimens were produced using the optimized parameters (laser power and scanning speed present in Table A.8) and different hatching values (30, 60, and 90 μm) for further validation. As expected, the alloys exhibited similar porosity percentages using different values of hatching, being lower than 0.1%vol. (see Table A.8). Therefore, it can be seen that the porosity is not affected by the hatching under these tested conditions.

Finally, through an extensive analysis using Box-Behnken design and ANOVA, the specimens for further microstructural, corrosion and wear characterization were built using the optimum L-PBF-processing parameters listed in Table 5.1, which are near the minimum porosity percentage according to RSM. The measured porosity percentage also can be seen in Table 5.1 for the corresponding alloys. Moreover, the introduction of boron has not significantly affected the processing parameters during L-PBF, indicating that the three alloys have relatively similar behavior during 3D-printing.

Table 5.1 - Optimum processing parameters used to produce the alloys by L-PBF and their respective porosity responses.

Alloy	Power (W)	Speed (mm/s)	Layer thickness (μm)	Beam diameter (μm)	Hatching (μm)	Porosity (%)
Pure-LPBF	250	600	25	40	60	0.06 ± 0.03
0.3B-LPBF	250	830	25	40	60	0.02 ± 0.01
0.6B-LPBF	250	850	25	40	60	0.03 ± 0.01

Regarding the pure and boron-modified alloys in this work, the Box Behnken model was very useful for L-PBF-parameter optimization, being able to provide good results with a relatively small number of specimens. In general, although the relatively slight difference of the chemical composition of the studied

alloys, the results show that they present similar optimum L-PBF-processing parameters. At high laser power value, even using high scanning speed, the porosity percentage was low. However, at low laser power, the porosity increases as the scanning speed increases, which is caused by insufficient energy to fully melt the material due to shorter interaction time between laser and the material, which in turn lowered the temperature within the melt pool. Regarding the production of boron-modified stainless steels for real applications, the use of lower values of laser power and higher scanning speeds is highly desired for low energy and time consumption. However, these results showed that, despite using the highest laser power, the processing time can be reduced using higher speeds, since low porosity percentages are obtained regardless of scanning speed in the tested conditions.

5.3 Microstructural characterization of the L-PBF-produced alloys

Fig. 5.5 shows the XRD patterns of the L-PBF-produced alloys. The measurements were conducted on the surfaces parallel and perpendicular to the building direction (BD). All specimens exhibit a microstructure completely δ-ferritic, similar to the powders (Fig. 5.1a), since L-PBF is also a rapid solidification process (10^4–10^6 K s^{-1}) [36, 51, 52, 75-77, 83, 84]. Moreover, the boron-modified specimens present evidence of M_2B phase, as can be seen from the inset graph of the XRD patterns in Figs. 5.5a, b.

Given the high temperature associated to L-PBF [36], the regular near-spherical shape feedstock powder (see Figs. 5.1b, d) are completely melted; thus, the δ-ferritic structure of the bulk specimens is ascribed to the L-PBF process instead to be inherited from the feedstock δ-ferritic powder.

Although the alloys present a chemical composition typical of a duplex stainless steel (Table 4.1), their microstructures are nearly completely δ-ferritic given the L-PBF solidification nature; hence, in the as-built condition, they can be described as a highly alloyed ferritic-induced stainless steel. It is reported [40, 49, 51-58] that a heat treatment must be applied to recover the duplex microstructure (ferrite + austenite) of L-PBF-produced duplex and superduplex stainless steels.

However, in this work, the focus is on the characterization of these alloys in their as-built condition, i.e., almost entirely δ-ferritic.

Moreover, by the XRD results in Fig. 5.5, for the Pure-LPBF specimen, the intensity of δ-ferrite peaks changes accordingly to the analyzed specimen's surface, in which the most prominent peak for the plane parallel to BD is in the diffraction angle of ~45° ({110}), and in ~65° ({200}) for the plane perpendicular to BD. This phenomenon is an indicative of crystallographic texture, being typical of alloys produced by L-PBF [15, 20, 33, 39, 40, 48-59, 61-64]. For the boron-modified alloys, this phenomenon was not observed, suggesting an absence of process-induced texture. Further investigation by EBSD to characterize the grain crystallographic orientation of the specimens will be presented along the text.

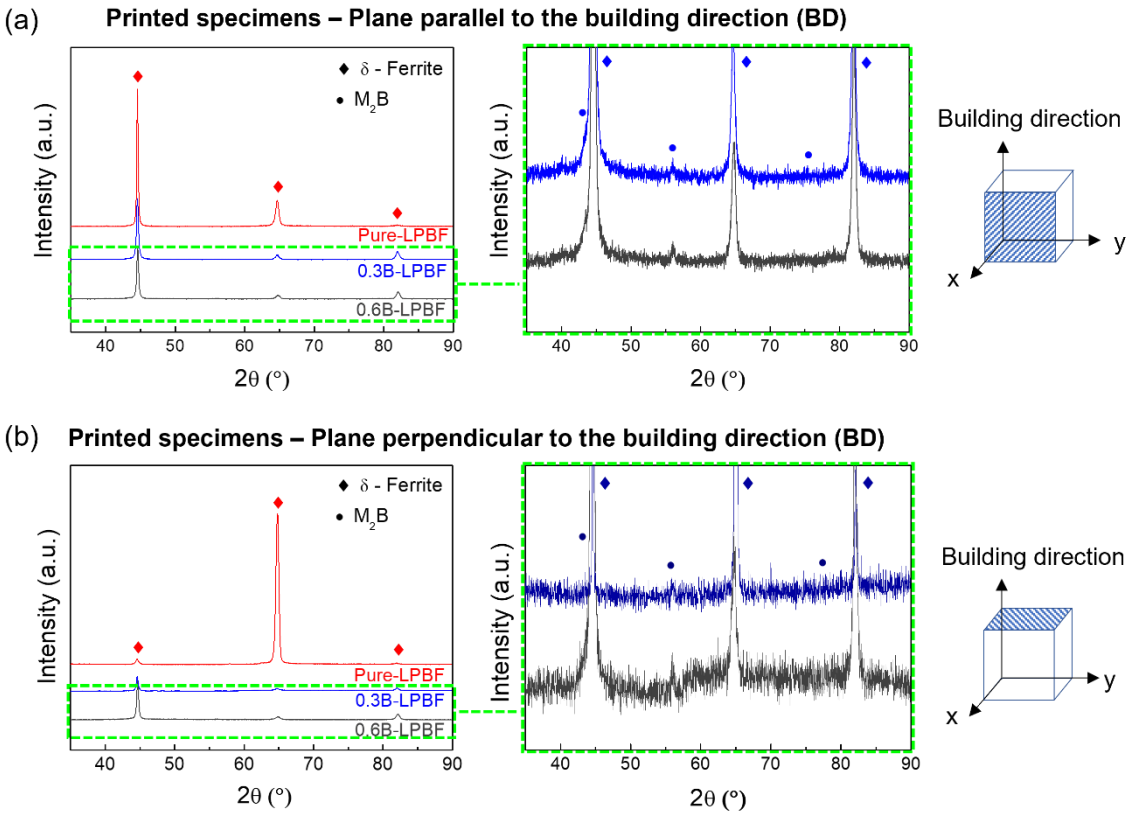

Figure 5.5 - XRD patterns of the Pure-LPBF, 0.3B-LPBF, and 0.6B-LPBF specimens in the planes (a) parallel and (b) perpendicular to the building direction. Zoom of the XRD patterns of the boron-modified printed specimens.

SEM analyzes were performed on the L-PBF-produced specimens in the planes along and perpendicular to the BD (Fig. 5.6). The Pure-LPBF specimen presents coarse columnar grains extending over several build layers (grain size ≥ 200 μm), in which its front and top views can be seen in Figs. 5.6a and b, respectively. These results are in agreement with the literature, since it is extensively reported [15, 20, 39, 40, 49-52, 59, 60, 62-64] that metals and alloys produced by L-PBF typically present large columnar grains across several layers according to the maximum temperature gradient along BD [85].

In contrast, the boron-modified stainless steels produced by L-PBF present an exceptionally refined microstructure composed of equiaxed δ-Fe grains, as can be seen in both planes (Figs. 5.6c-f). These results suggest that the addition of 0.3 and 0.6 wt.% of boron change the solidification conditions during L-PBF, leading to a remarkable grain refinement. It can be observed that the mean grain size decreased from ~200 μm (unmodified alloy) to ~1-2 μm (boron-modified alloys). As well, although the specimens exhibit homogeneous refined microstructure, from Figs. 5.6c, e, relatively coarse δ-Fe grains are observed in the melting pool boundaries, being mainly associated to the formation of a heat-affected zone (HAZs) below the melt pool boundaries, which is described as an grain coarsening effect in the HAZ through laser scanning and remelting of sequential layers [20, 84, 85]. However, compared to the specimen without boron addition, even the relatively coarse-grained regions in the boron-modified alloys are extremely refined.

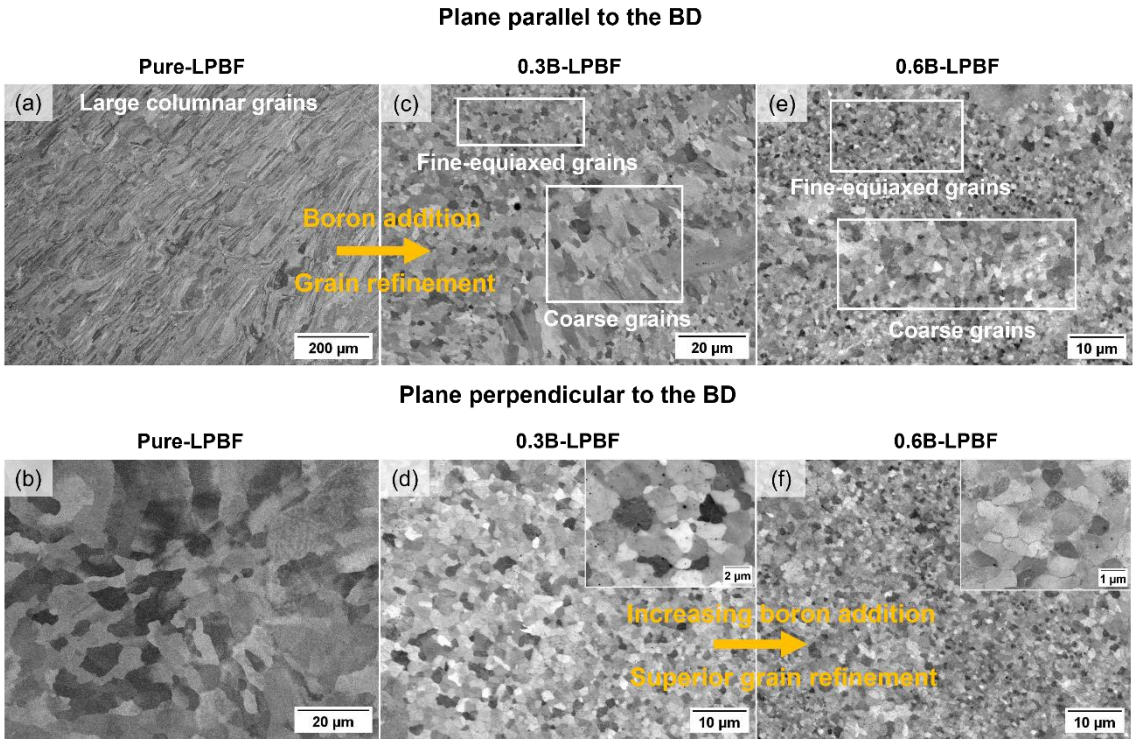

Figure 5.6 - SEM micrographs showing the planes parallel and perpendicular to the building direction (BD) of (a, b) Pure-LPBF, (c, d) 0.3B-LPBF, and (e, f) 0.6B-LPBF specimens, respectively.

Also, compared to the 0.3B-LPBF specimen, the alloy modified with 0.6 wt.% of boron presents a superior grain refinement, indicating that the refinement effect on the δ-ferrite grains is enhanced by increasing the boron content. Low magnification EBSD-micrographs of the boron-modified specimens in the plane parallel to the BD can be seen in Fig. 5.7. From an overview of the inverse pole figure (IPF) and GBs maps in Figs. 5.7a-d, it can be seen that both specimens present a homogeneous refined grain structure with few coarse grains (≤ 20 µm) indicated by red arrows in Figs. 5.7b, d. It is worth to stress that the 0.3B-LPBF and 0.6B-LPBF alloys are a result of the mixing of a pure and a boron-modified DSS powders, as detailed in section 4.1.

Therefore, the few number of coarsened grains present in the L-PBF-microstructure are a result of epitaxial grain growth that may be associated to insufficient boron content within some melt pools during heating, possibly caused during powder's mixing. Nonetheless, it can be concluded that the powder's

mixture was effective, and the boron was homogeneous distributed in the molten metal during heating in L-PBF.

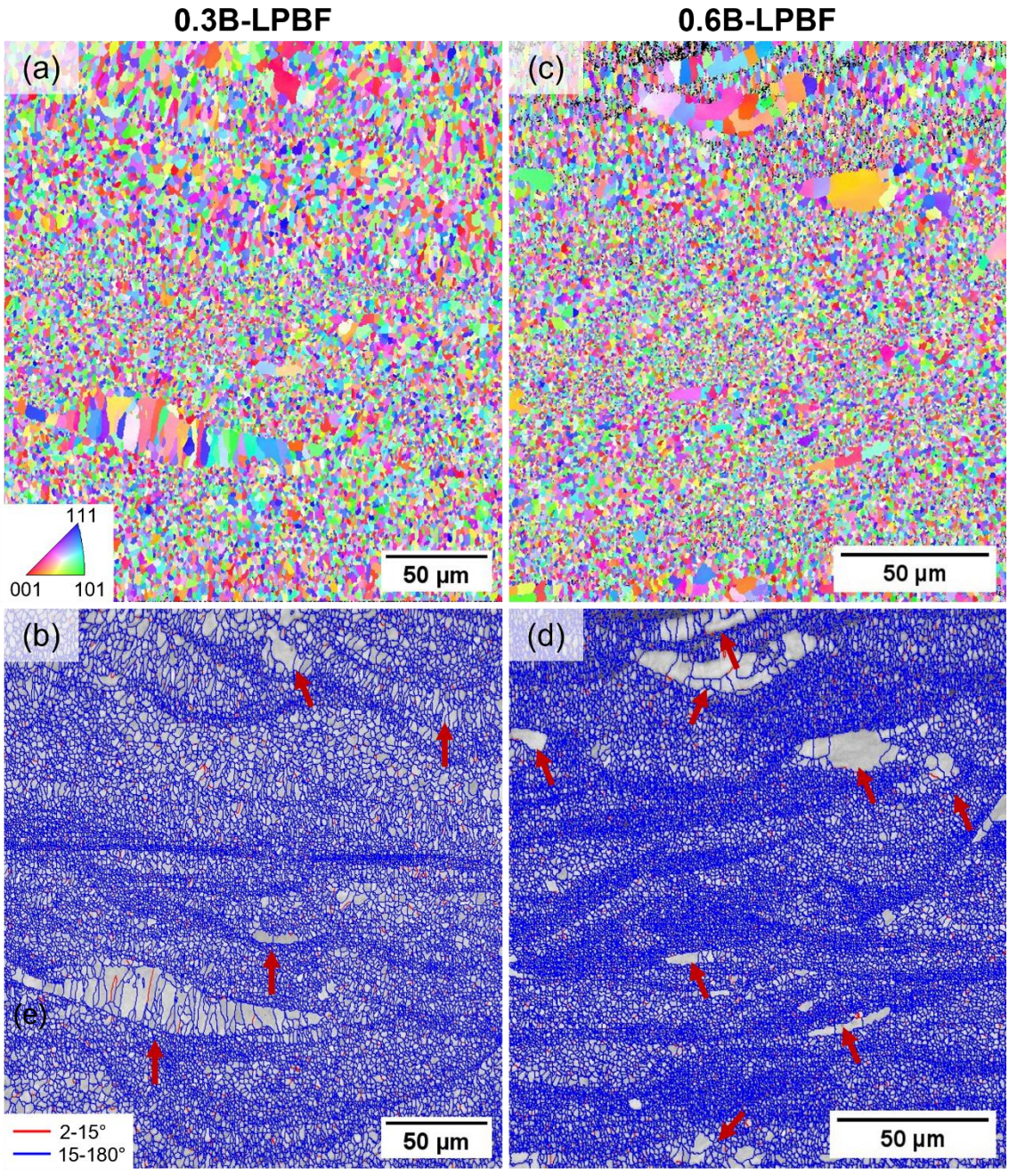

Figure 5.7 - EBSD characterization of the plane parallel to the building direction of the L-PBF specimens. Inverse Pole Figure (IPF-X) maps of (a) 0.3B-LPBF, and (b) 0.6B-LPBF specimens. Grain boundary distribution maps of (c) 0.3B-LPBF, and (d) 0.6B-LPBF specimens. Red arrows indicate coarser grains at the melting pool's bottoms, respectively.

EBSD analyzes were also performed in both planes of the L-PBF-produced specimens and can be seen in Fig. 5.8. The IPF maps in Figs. 5.8a-c and j-l show that, unlike the grains of the boron-modified specimens which no preferred grain orientation is observed, for pure duplex stainless steel, most of the grains are oriented at <001> (for the planes parallel and perpendicular to the BD), and <101> (for the plane parallel to the BD), being the preferred solidification direction with the highest heat flow for the δ-Fe grains [38-40, 48]. From the phase maps in Figs. 5.8d-f and m-o, all the alloys present a fully δ-ferritic microstructure (green color) with small traces of γ-austenite (red color), which is in agreement to the aforementioned XRD analysis (Fig. 5.5), and to recent studies regarding L-PBF-produced DSSs [15, 20, 33, 39, 40, 48-64].

Figs. 5.8g-i and p-r show the grain boundaries misorientation maps for the studies alloys. The boron-modified alloys contain a high fraction of high angle grain boundaries (HAGBs), which are defined by grain boundaries misorientations ≥ 15°. It confirms the presence of very refined and equiaxed δ-Fe grains on both planes. Also, there is no significant difference between both planes in terms of the δ-ferrite grain size. For the boron-modified alloys, the fraction of low angle grain boundaries (LAGBs) is much lower compared to HAGBs, while the pure alloy presents a high number of LAGBs (grain boundaries misorientation < 15°). It is reported that L-PBF-processed alloys present sub-grain structures caused by local lattice distortions [86].

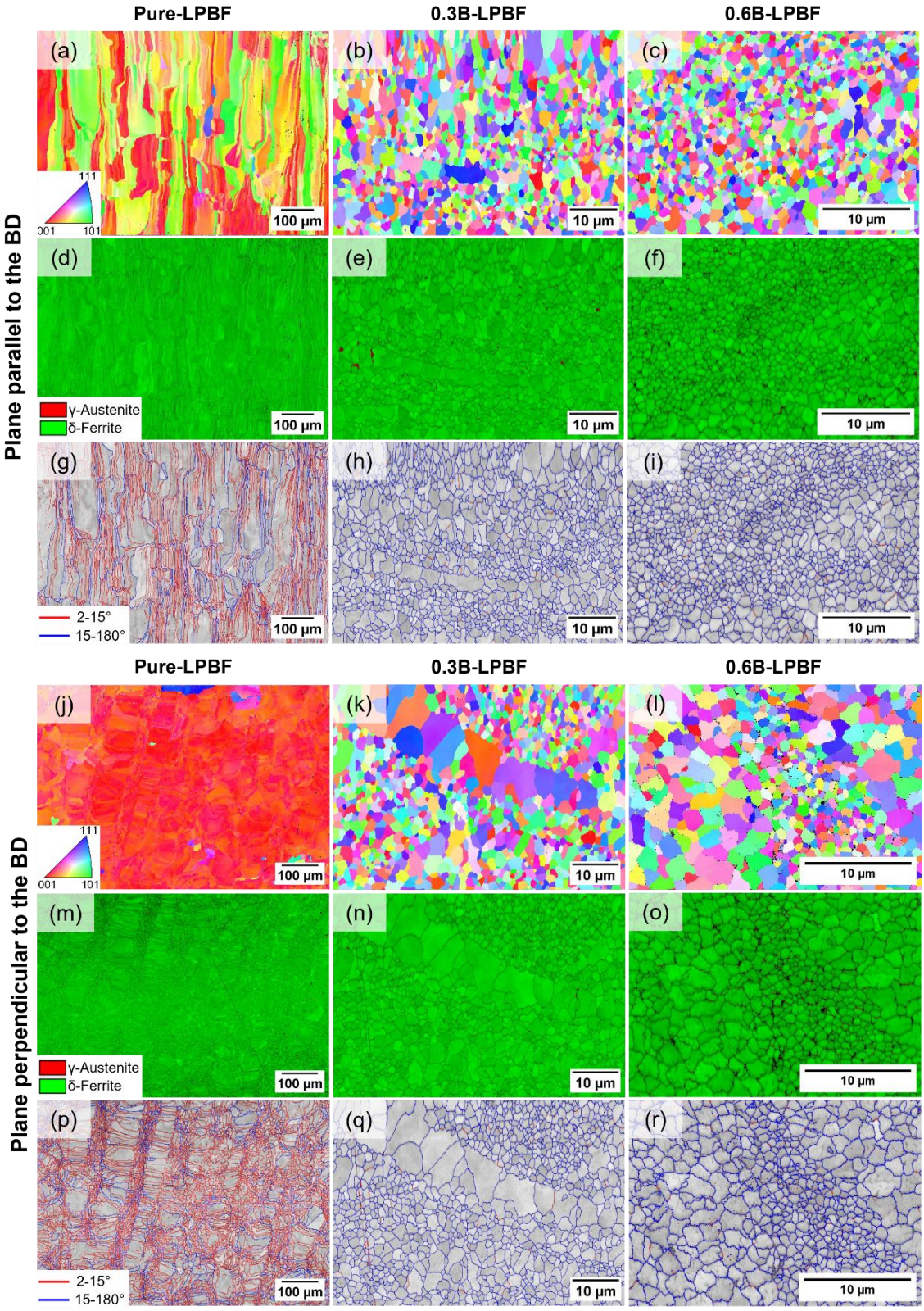

Figure 5.8 - EBSD characterization of the L-PBF-produced alloys in the planes parallel and perpendicular to the BD. (a-c, j-l) Inverse Pole Figure (IPF-X) maps,

(d-f, m-o) phase + image quality (IQ) maps, and (g-i, p-r) grain boundary distribution maps.

Pole figures (PF) were used to quantitatively evaluate the crystallographic texture of the L-PBF-produced alloys (see Fig. 5.9). The PF plots quantify the texture intensities along the three crystallographic direction-families <001>, <101> and <111>. It is worthy to mention that PF plots for γ-austenite phase were not performed due to its small phase fraction in as-built alloys. Furthermore, since the Pure-LPBF alloy has very large grain size, its texture quantification is only an estimative, since the statistics are insufficient for a reliable texture quantification. On the other hand, given its extremely refined microstructure, more than 1000 grains were used to perform the texture quantification for the boron-modified alloys.

For the pure alloy (Fig. 5.9a), it is possible to note the fiber texture along the BD, which is a result of the high directionality in heat transfer during 3D printing [35, 65, 87], indicating a tendency to anisotropic properties. The boron-modified stainless steels exhibit a highly randomized crystallographic texture (Figs. 5.9b, c). Such random crystallographic textures in L-PBF alloys may be highly desirable for many structural applications [14-17, 66], suggesting that boron-modified stainless steels with isotropic properties can be produced by L-PBF.

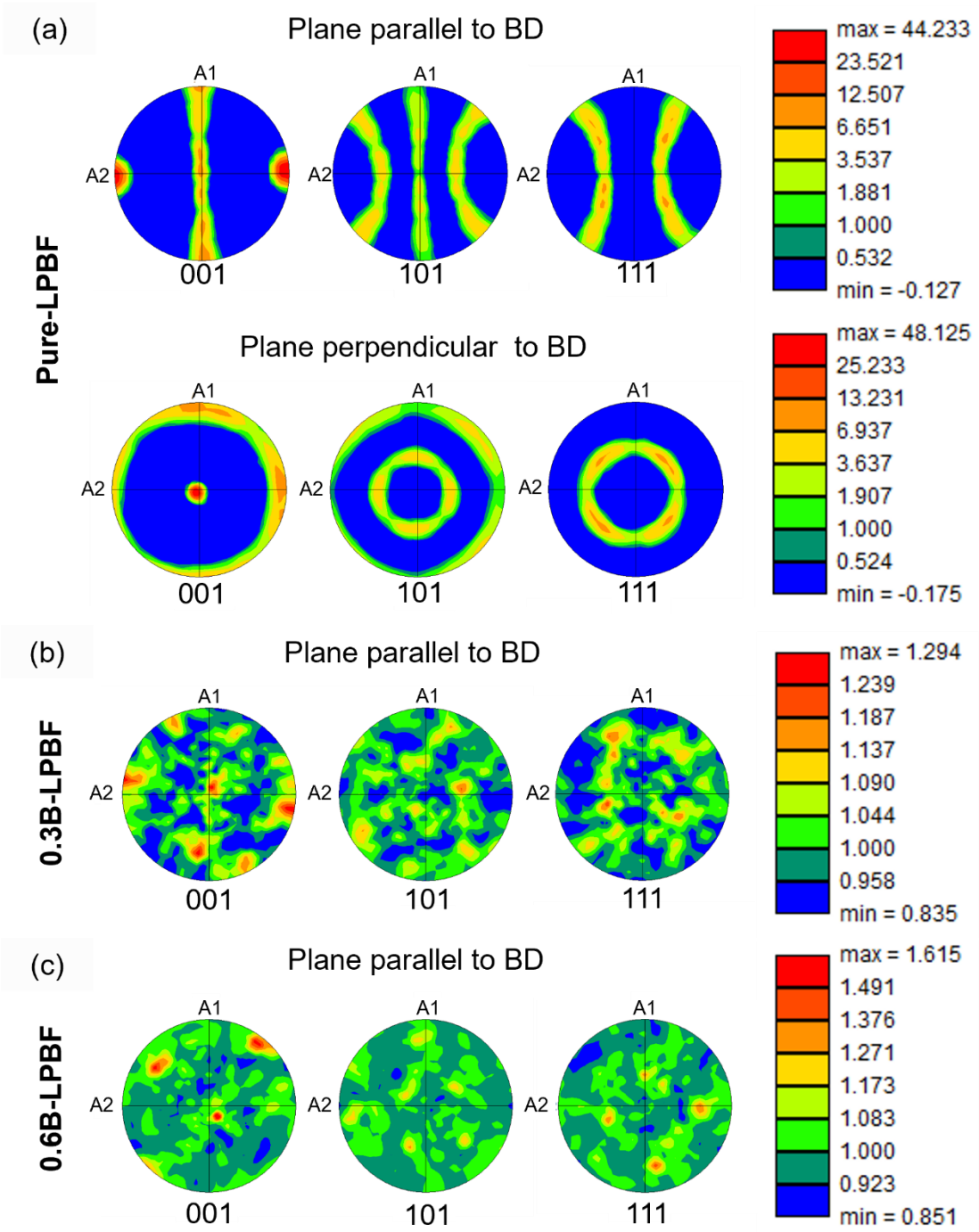

Figure 5.9 - (001), (101), and (111) pole figures of δ-ferrite for (a) Pure-LPBF, (b) 0.3B-LPBF, and (c) 0.6B-LPBF specimens. Crystallographic textures were calculated from EBSD datasets using the harmonic series expansion method with a Gaussian half-width of 5°, and a series rank of 34.

These results imply that the addition of boron promotes an excellent grain refinement in DSSs produced by L-PBF. To better understand the role of boron on the grain refinement mechanism, the alloys were further analyzed by SEM and TEM.

Figs. 5.10a, b show the microstructure of the boron-modified alloy after an etching procedure applied to attack the matrix. An interconnected and continuous network of particles (grey skeletal structure) can be seen surrounding the refined δ-ferrite grains (dark hollow regions). Moreover, as previously described, fine and coarse-grained zones are identified (Fig. 5.10a), in which refined particles are also present within the coarser grains (see the labeled area in Fig. 5.10b). These particles are not present within the grains of the fine-grained zone.

To assess the nature of these particles, present in the boron-modified alloys, STEM-DF micrographs and corresponding EDX analysis are shown in Figs. 5.10c-f. As already described, nanoparticles along the GBs and within the coarser grains can be observed in Figs. 5.10c, d. These particles are around 50-100 nm large and enriched in chromium, as can be seen by EDX phase map in Fig. 5.10e, and the EDX analysis (Fig. 5.10f) from the labeled areas in Fig. 5.10d.

Moreover, from Fig. 5.10d, a high number of dislocations can be observed. As previously reported [49], the high cooling rates during L-PBF induce these lattice defects, which also lead to high stresses and, thus, to the development of dislocations similar to those found after a thermomechanical process. It is reported [48] that the high dislocation density in the as-built alloys is related to development of plastic gradients within the grains which are contained by the formation of agglomerated dislocations.

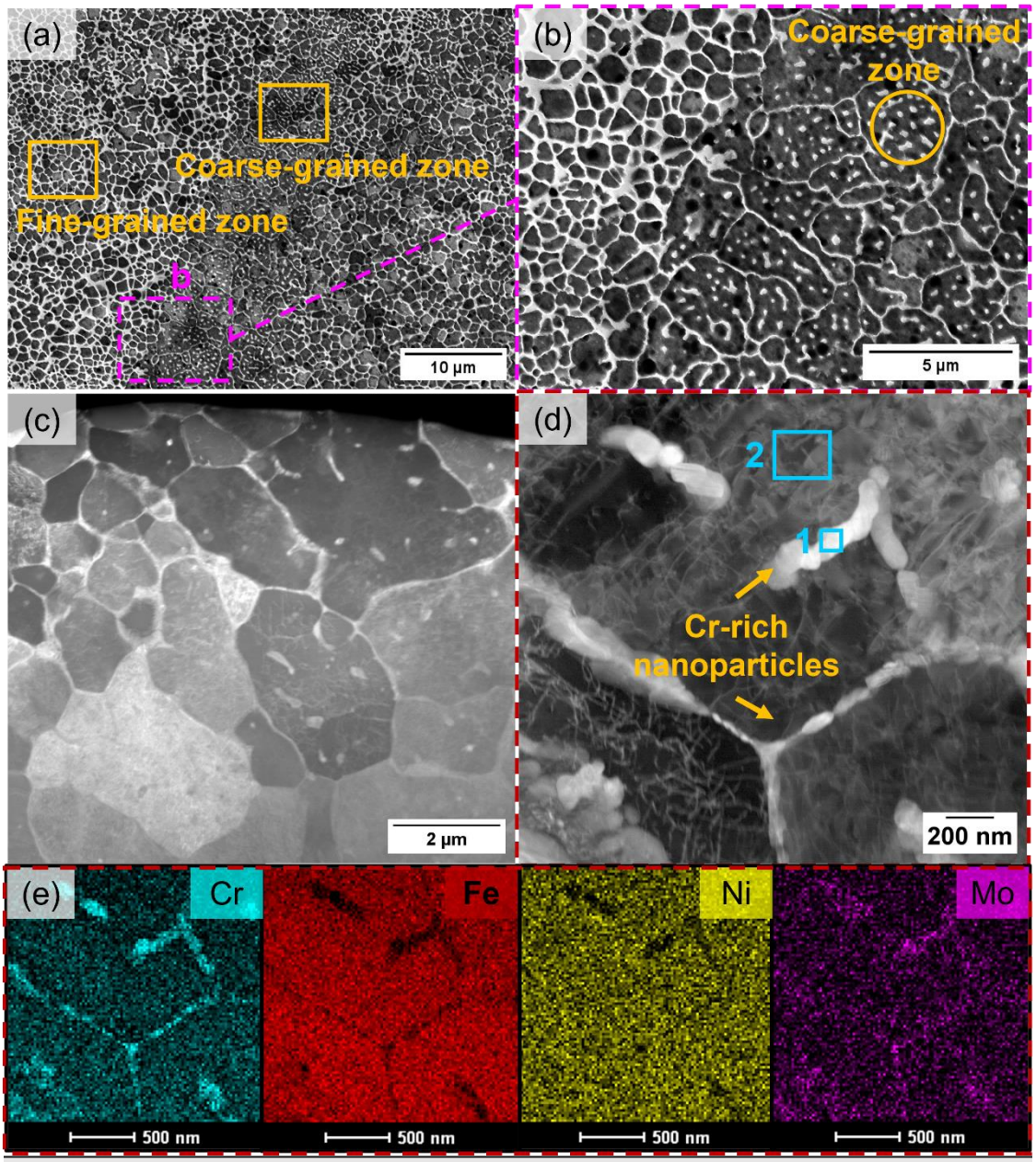

(f) Labeled area (%at.)	Cr	Ni	Mo	Mn	Si	Fe
1	47.88	2.41	1.92	4.96	2.27	Bal.
2	24.50	5.24	1.10	2.67	2.87	Bal.

Figure 5.10 - SEM and TEM analysis of the 0.6B-LPBF specimen. SEM micrograph showing interconnected and continuous network of particles in (a) low, and (b) high magnification after etching. STEM-DF micrographs showing nanoparticles decorating grain boundaries in (c) low and (d) high magnification, (e) HAADF-EDX maps from the area present in Fig. 5.10d, and (f) EDX analysis of the area in Fig. 5.10d.

Additionally, selected area electron diffraction (SAED) (Fig. 5.11b) and electron nanodiffraction (Fig. 5.11c) patterns from the labeled areas in Fig. 5.11a confirm that the microstructure of the boron-modified alloys is composed of plate-like Cr_2B nanoborides distributed along the GBs and within coarser δ-ferrite grains. Also, Figs. 5.11e and f, respectively, show ASTAR-TEM orientation and phase maps from the labeled area in Fig. 5.11d for the boron-modified alloy, in which Cr_2B nanoborides are at the GB of different δ-ferrite grains. As previously stated, the formation of Cr_2B phase is predicted by thermodynamic calculations in equilibrium solidification (Fig. 4.1), and by XRD analyzes performed in the boron-modified L-PBF-produced alloys (Fig. 5.5).

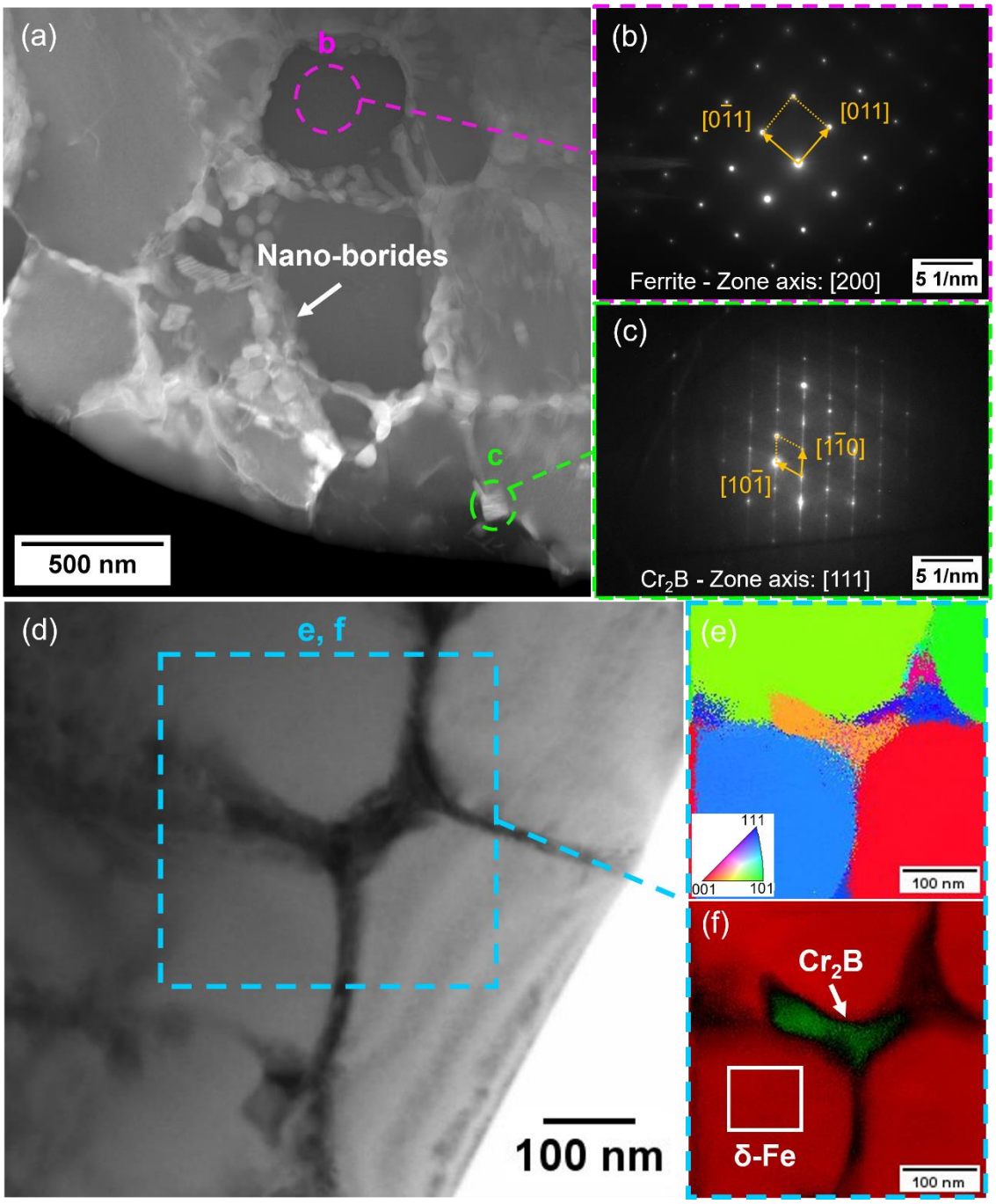

Figure 5.11 - TEM and ASTAR analysis of the 0.6B-LPBF specimen. (a) STEM-DF micrograph showing nanoprecipitates decorating grain boundaries. SAED patterns related to (b) δ-Fe matrix, and (c) Cr_2B nanoborides. (d) TEM-BF showing the nanoborides at the GBs, and ASTAR analysis showing the (e) crystallographic orientation map, and (f) phase map of the labeled area in Fig. 5.11d.

Indeed, for the L-PBF-printed boron-modified alloys, this interconnected and rigid armor of borides within the microstructure is relatively similar to typical eutectic microstructures exhibited for hypoeutectic boron-modified stainless steels extensively studied in previous works [5-7, 11]. However, unlike the microstructure exhibited by the boron-modified stainless steel produced by L-PBF, which is a fine-grained δ-Fe composite reinforced with nanoborides, the alloys obtained by spray forming [5-7, 11] present a relatively coarser microstructure reinforced with micro-size boride particles (~10 μm) in a duplex matrix (γ + α). Therefore, it indicates that, given the specific solidification conditions involved in L-PBF (e.g., high G, fast cooling), boron plays an important role in promoting excellent grain refinement during the solidification of these alloys.

Grain refinement was recently reported for several L-PBF-produced alloys, being achieved by addition of potent inoculants [15-21], and/or proper solutes [22, 23, 25-27], and by adjusting processing parameters to promote CET [14, 15, 18]. It is worthy to emphasize that for hypoeutectic boron-modified DSSs, δ-Fe is the first phase to form from the liquid, followed by the formation of M_2B, in equilibrium conditions (see the thermodynamic calculations in Fig. 4.1). Hence, M_2B cannot act as an inoculant particle for heterogeneous nucleation of δ-Fe during solidification, since it is not a primary phase. Although the borides are already formed in the powder (see Figs. 5.1a, e), the high temperature during L-PBF melts all phases. Therefore, the presence of boron and its segregation in L-PBF solidification may create conditions to restrict the δ-ferrite grain growth and to form a nano-eutectic structure.

On the one hand, the pure alloy (boron-free) presents a typical coarse textured columnar microstructure, being ascribed to the solidification conditions of L-PBF. Particularly, this is due to large thermal gradients along the BD, and high cooling rates within micro-sized melt pools [38-40]. The nucleation of δ-Fe occurs at the bottom of the melt pool, followed by epitaxial grain growth along <001> and <101> directions, which is characteristic for polycrystalline materials with cubic structures [35]. The formation of large columnar δ-ferrite grains that extent over several layers indicates that there was no nucleation event happening

at the front of the growing S/L interface; besides, the successive remelting of the already solidified layers during the process was only partial, thus, the remained grains enabled the epitaxial growth of the subsequent layers.

On the other hand, as described in Section 2.4, the occurrence of nucleation ahead of the epitaxially growing S/L interface is necessary to interrupt the columnar δ-ferrite grain growth during L-PBF solidification. Therefore, to obtain such fine equiaxed grains in the boron-modified alloys, it is known [44] that sufficient undercooling (ΔT) over the critical nucleation undercooling (ΔT_n) is required. It is worthy to mention that the overall undercooling (ΔT) ahead of the S/L interface consists of the difference between the melt temperature and the alloy liquids temperature, which is a sum of the thermal undercooling (ΔT_t), constitutional undercooling (ΔT_{CS}), and curvature undercooling (ΔT_r).

L-PBF solidification has special features, which has to be considered to understand the mechanisms for the outstanding grain refinement exhibited by the boron-modified alloys.

Boron is very efficient to generate constitutional undercooling (ΔT_{cs}) in ferrous alloys processed by casting, i.e., it exhibits a high growth restriction factor (Q) in the iron system [28]. Therefore, in conventional casting, boron segregates ahead of the solidification front due to its very low solubility in iron [5] resulting in a solute profile ahead of the S/L interface. The high segregation of boron is responsible for changing the solidification temperature ahead of the growing crystal, which coupled with the low thermal gradient (G) generates undercooling mostly by the constitutional undercooling (ΔT_{cs}), in which ΔT_t and ΔT_r are normally insignificant. Then, heterogeneous nucleation takes place on inoculants within the constitutional undercooling zone created by boron segregation, restricting the epitaxial grain growth and promoting grain refinement [22, 44]. In such cases, the high Q value presented by boron is an appropriate indicator to estimate its grain refinement effectiveness, since Q value indicates the efficiency of a solute to generate ΔT_{cs}.

However, unlike conventional casting process (low thermal gradient around 10^0-10^2 K/m [88]), L-PBF exhibits large thermal gradient (G) and high cooling rate (~10^6 K/m, and 10^3 - 10^6 K/s, respectively [35]), which may eliminate

the constitutional undercooling zone created by boron segregation, thus, weakening its growth restriction efficiency. Therefore, following recent findings from simulations and experimental data [21-23] to explain the grain refinement of different alloys produced by L-PBF, it is inferred that as the δ-ferrite melt solidifies, solute rejection at the growing S/L interface causes the formation of a boron-enriched solute boundary layer ahead of the solidification front, which is responsible to reduce the solidification front velocity, generating a lag in the growth rate of the δ-Fe crystal. Therefore, although the fast cooling rate induces high crystal growing velocity, it is constrained by the solute segregation. Thus, the difference between the theoretical and real growth rate during fast cooling promotes substantially large thermal undercooling (ΔT_t) ahead of the S/L interface. In theory, the solidification front should lag further behind the isotherm of the solidus temperature, which is established by the L-PBF-scanning speed and the thermal conductivity of the material [23]. This enlarged undercooling is responsible for increasing the nucleation rate on the underlying layer, favoring grain refinement. Therefore, unlike conventional casting in which the overall undercooling is based on the constitutional undercooling (ΔT_{cs}), at high cooling rate and large thermal gradients in L-PBF, thermal undercooling (ΔT_t) is the main responsible for the undercooling necessary for nucleation in front of the S/L interface. Therefore, the Q value cannot broadly reveal the role of solutes during L-PBF solidification, since there is not a linear correlation between Q value and grain size [22, 25]; instead, the grain refinement efficiency is governed by ΔT_t generated by the solute segregation. Similar results have been reported for different alloys system (e.g., Al-Si, Al-Ni, Al-Cu, Mo-B, Mo-C, and Fe-B) [22, 23, 25-27].

The presence of a boride network in a like-eutectic microstructure indicates an ineluctable solute segregation during solidification of the L-PBF-produced boron-modified alloys. Furthermore, increasing the boron content from 0.3 to 0.6 wt.%, a greater grain refinement efficiency is observed, which may be explained by the time-dependent nature of the kinetic process of the solute rejection. For the alloy with higher boron content, more boron is rejected from the growing δ-Fe crystal to the liquid, causing a higher lag in crystal growth and,

consequently, inducing a higher thermal undercooling (ΔT_t). For other L-PBF-produced alloys, it was also reported that increasing the solute content, a higher degree of grain refinement was achieved [22, 25-27].

Moreover, it is known that the L-PBF-processing parameters affect the thermal gradient and cooling rate during solidification, which consequently also influence the undercooling. Although in this work slightly different processing parameters were utilized to achieve the highest bulk density in the studied alloys, one may assumed that G is almost the same for the three evaluated materials. Anyhow, for all processing conditions, the pure DSS present columnar grain structure aligned to the BD (see Fig. 5.2b). Therefore, it is inferred that boron has a critical influence on crystal growth and grain refining efficiency of DSSs.

In summary, the production and solidification path of the boron-modified alloys from powder production to final L-PBF-produced parts are illustrated in Figure 5.12 and described below:

- Two powders were used as precursors, in which commercial DSS presents a fully δ-ferritic microstructure, and hypereutectic DSS modified with 1.2 wt.% of boron presents a microstructure composed of primary M_2B refined needles-like (~1 μm) homogeneously distributed in a δ-ferrite matrix. Mechanical mixing of powders precursors resulted in two hypoeutectic compositions, in which the boron content was reduced from 1.2 to 0.3 and 0.6 wt.%.
- During L-PBF, depending on the processing parameters, the temperature may reach 3000-5000 K [40, 89]; thus, the interaction between the laser beam and the mixed powders leads to the formation of a melt pool composed of fully melted δ-ferrite and M_2B phase (hypoeutectic composition) (Fig. 5.12, step (i)). Owing to the decomposition of finer M_2B needles (melting point around 2000 K [90]), many free atomic B and M (M = Fe, Cr) are incorporated to the molten metal. Such statement is supported by the presence of interconnected network of nanoborides at the GBs of the L-PBF-microstructure, instead of the micro-sized needles of M_2B present in the powder. Due to the convective forces and Marangoni flow within the melt pool, the molten metal is mixed and boron atoms are homogeneously distributed within the liquid (Fig. 5.12, step (ii)).

- With the fast cooling of the melt pool, and accordingly to thermodynamic calculations, primary δ-ferrite starts to solidify directly from the liquid. Since boron has a very low solubility in solid iron (<0.008 wt.% [30]), the dissolved boron atoms are rejected and segregated into the liquid at the front of the S/L interface of the δ-Fe growing grain. Such segregation results in a boron-enriched layer at the front of the S/L interface (Fig. 5.12, step (iii)). Compared to the theoretical growing rate, the boron-rich layer causes a lag in the actual growth of the S/L interface, extending the thermal undercooling ahead of the growing δ-Fe (Fig. 5.12, step (iv)). This increased undercooling increases the nucleation rate on the underlying layer, favoring the formation of numerous new grains that further impair the columnar δ-Fe grain growth (Fig. 5.12, step (v)).
- Following, the segregation raising the localized boron content close to the eutectic point (which is around 1 wt.% of boron accordingly to Fig. 4.1), the eutectic reaction $L \rightarrow \delta + M_2B$ occurs. As primary δ-ferrite grains are formed, boron remains in the liquid phase and, thus, it is segregated to the GBs (Fig. 5.12, step (vi)). Thus, the eutectic mixture of δ-Fe and M_2B-type nanoborides are formed in the last stage of solidification by the reaction of B with Cr and/or Fe, creating a continuous network around the equiaxed primary δ-Fe grains. Moreover, M_2B nanoborides act as GBs pinning points and limit the growth of δ-Fe grains, resulting in an extremely refined microstructure (Fig. 5.12, step (vii)).
- Despite the low solubility of boron in iron, one may be expected that the rapid solidification during L-PBF slightly extend the solubility of B in δ-ferrite [91], therefore, boron trapped in δ-Fe may precipitate due to heating and cooling cycles of L-PBF, being responsible for formation of Cr_2B nanoparticles within the relatively coarsened δ-Fe grains (see Fig. 5.10b). The high dislocation density present in the L-PBF-produced alloys (Fig. 5.10d) may enhance diffusion of the elements in solid solution and facilitate precipitation.

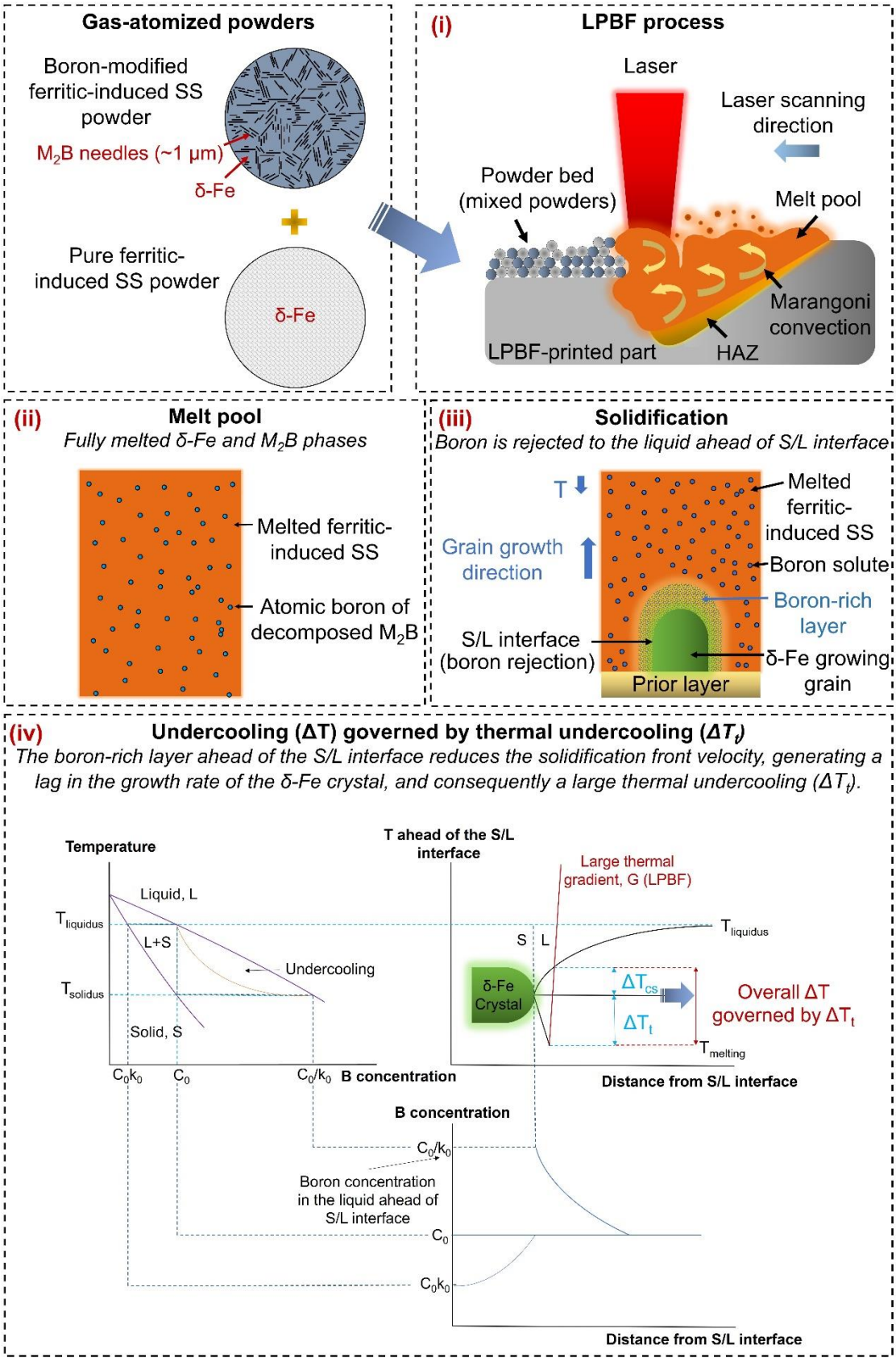
Gas-atomized powders
Boron-modified ferritic-induced SS powder
M2B needles (~1 μm)
δ-Fe
Pure ferritic-induced SS powder
δ-Fe
(i) LPBF process
Laser
Laser scanning direction
Powder bed (mixed powders)
Melt pool
Marangoni convection
LPBF-printed part
HAZ
(ii) Melt pool
Fully melted δ-Fe and M2B phases
Melted ferritic-induced SS
Atomic boron of decomposed M2B
(iii) Solidification
Boron is rejected to the liquid ahead of S/L interface
T
Grain growth direction
S/L interface (boron rejection)
Melted ferritic-induced SS
Boron solute
Boron-rich layer
δ-Fe growing grain
Prior layer
(iv) Undercooling (ΔT) governed by thermal undercooling (ΔTt)
The boron-rich layer ahead of the S/L interface reduces the solidification front velocity, generating a lag in the growth rate of the δ-Fe crystal, and consequently a large thermal undercooling (ΔTt).
Temperature
Liquid, L
Tliquidus
L+S
Undercooling
Tsolidus
Solid, S
C0k0
C0
C0/k0
B concentration
T ahead of the S/L interface
Large thermal gradient, G (LPBF)
S
L
Tliquidus
δ-Fe Crystal
ΔTcs
ΔTt
Overall ΔT governed by ΔTt
Tmelting
Distance from S/L interface
B concentration
C0/k0
Boron concentration in the liquid ahead of S/L interface
C0
C0k0
Distance from S/L interface

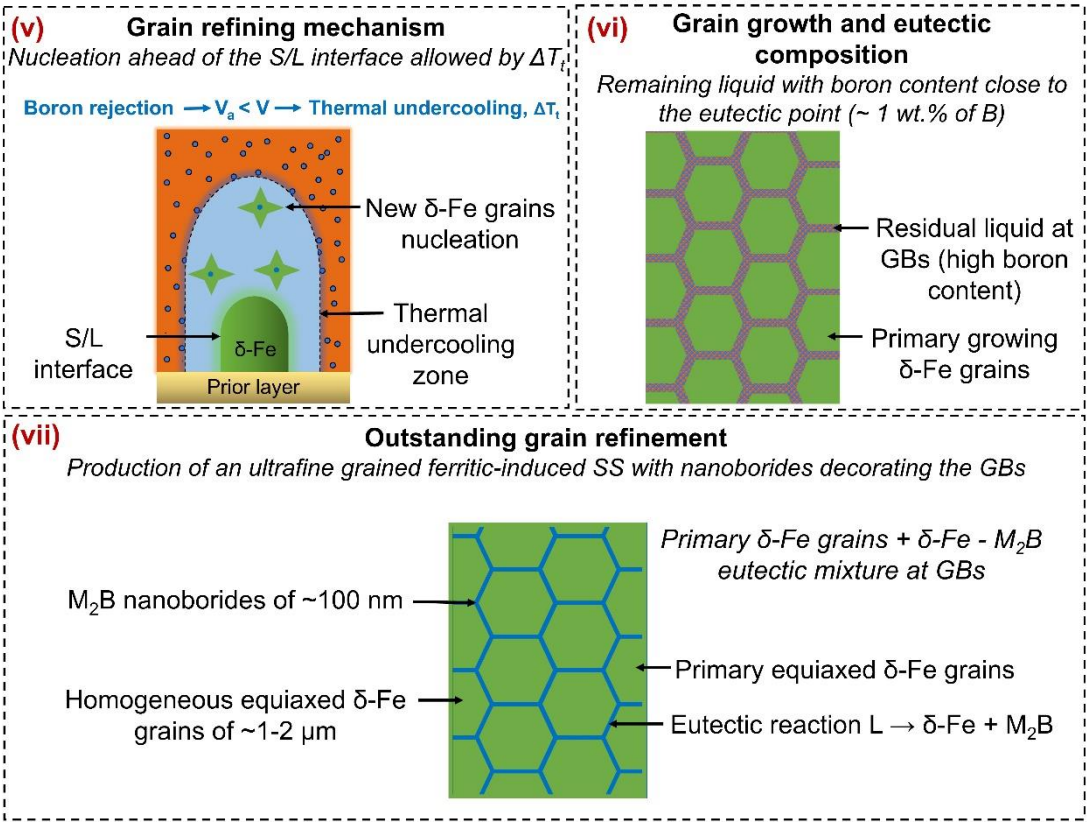

Figure 5.12 – Schematic illustration of the solidification path of the boron-modified alloys: (i) Boron pre-alloyed + pure FSS-induced powders mixture submitted to L-PBF, (ii) fully melting of powders within the melt pool, (iii) δ-Fe crystal formation, boron segregation, and formation of a boron-rich boundary ahead of the S/L interface, (iv) undercooling conditions ahead of the crystal tip during solidification in L-PBF condition, (v) nucleation of δ-Fe ahead of the S/L interface promoted by the enlarged thermal undercooling, (vi) δ-Fe grain growth and eutectic reaction in the remaining liquid within the GBs, (vii) formation of an ultrafine δ-induced stainless steel reinforced with M_2B nanoborides. Illustrations not to scale.

The results indicate that the addition of boron is very efficient to promote the formation of fine and equiaxed grained structure in FSSs or DSSs produced by L-PBF. Compared to other studies regarding the grain refining in stainless steels [16-21, 26], it can be seen that even low content of boron presents an outstanding efficiency in refining grains of stainless steels.

Interestingly, a recent work [26] evaluated the effect of boron on the grain refinement of an austenitic stainless steel produced by L-PBF. However, unlike

the current work in which a pre-alloyed boron-modified DSS powder was used, they performed an ex-situ mixture of pure boron particles (~2 µm) to a 316L powder (~30 µm). Even using double of boron content (~1 wt.% of boron), their efficiency on grain refining was drastically lower compared to that obtained in this work (see Fig. 2.4). In the current study, the high grain refinement efficiency even using small boron content (0.3 and 0.6 wt.% of B) may be related to the homogeneous distribution of refined borides within the matrix of the FSS-induced powder, which may facilitate the homogeneous melting and distribution of boron within the molten metal during L-PBF process.

Conclusively, a boron-modified stainless steel using pre-alloyed powders were produced by L-PBF for the first time, presenting an interesting grain structure which may be desirable for many applications, since the formation of a non-textured, refined and equiaxed grains may reduce the tendency to anisotropy and cracking susceptibility.

5.4 Hardness and wear resistance of the L-PBF-produced alloys

In the following section, the hardness and wear resistance of the as-built Pure-LPBF and 0.6B-LPBF specimens are evaluated (i.e., in its fully δ-ferritic state). For benchmark purposes, the results are compared to a hot-rolled SAF 2205 (commercial duplex stainless steel). Therefore, to allow a correlation between microstructure and properties, micrographs of the commercial SAF 2205 DSS are presented in Fig. 5.13, being possible to observe a dual-phase (α + γ) microstructure with elongated grains along the rolling axis, typical of hot rolled metals.

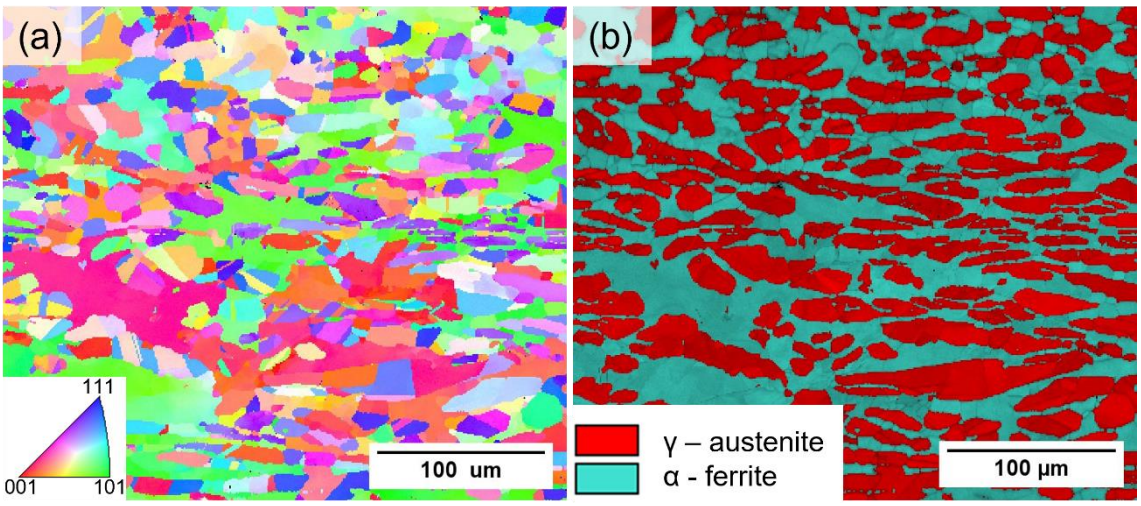

Figure 5.13 - EBSD characterization of SAF 2205 DSS submitted to hot rolling and heat-treatment at 1373 K followed by quenched in water. (a) Inverse Pole Figure (IPF-X) map, and (b) phase + image quality (IQ) map. Chemical composition obtained by optical emission spectroscopy (in wt.%): 0.026 C, 0.47 Si, 1.26 Mn, 0.028P, 22.02 Cr, 5.37 Ni, 2.89 Mo, 0.25 Cu, Fe bal.

Figure 5.14a shows the specific wear rate (κ) versus Vickers microhardness ($HV_{0.5}$), and the coefficient of friction (COF) along with the sliding distance for the studied alloys shown in Figure 5.14b.

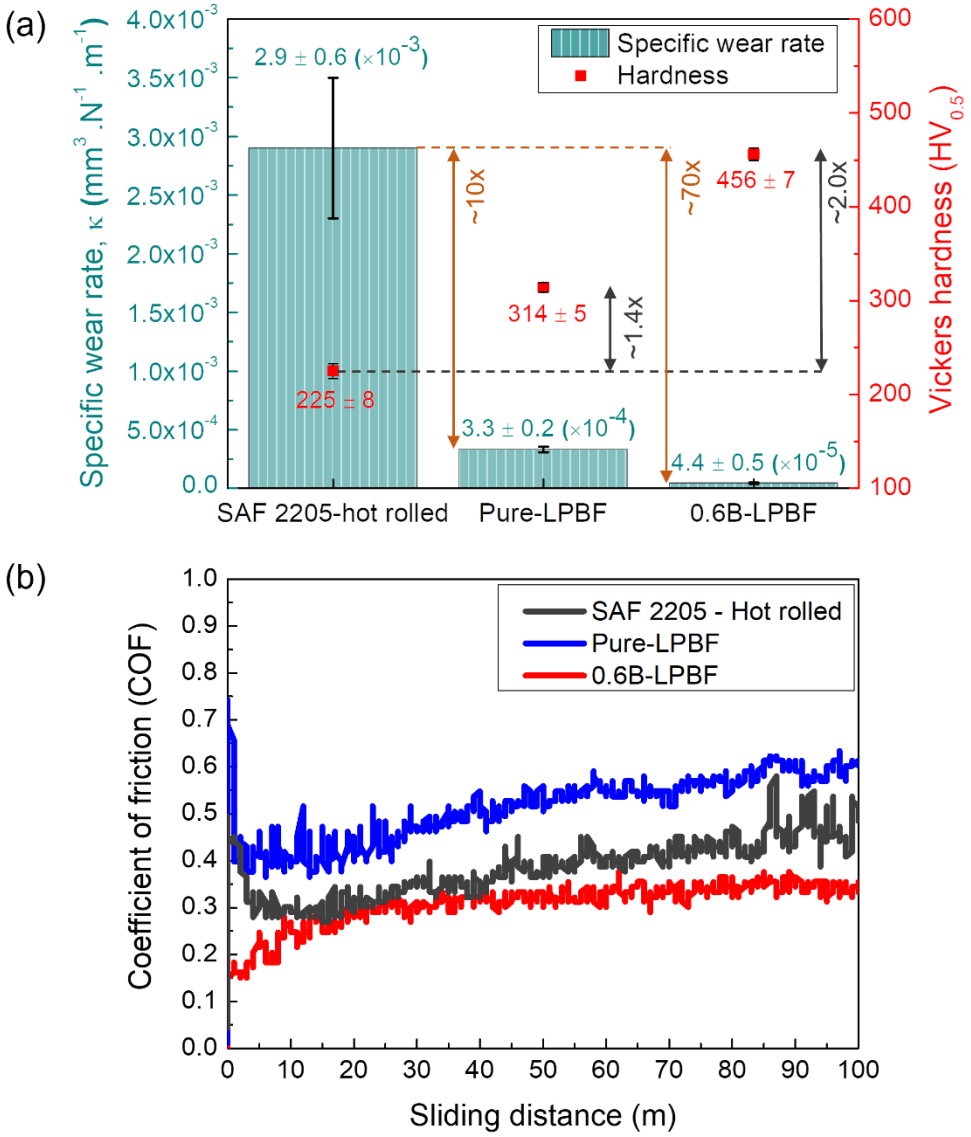

Figure 5.14 - Results of reciprocating pin-on-plate wear test. (a) Specific wear rate (k) vs. Vickers hardness ($HV_{0.5}$), and (b) coefficient of friction (COF) vs. sliding distance. Mean values and deviations from tests in triplicate. 10 indentations per specimen were performed for hardness measurement.

The microhardness values for the hot-rolled SAF 2205, Pure-LPBF, and 0.6B-LPBF specimens are 225 ± 8 $HV_{0.5}$, 314 ± 5 $HV_{0.5}$, and 456 ± 7 $HV_{0.5}$, respectively. The standard deviation was very low, indicating a uniformity of surface's hardness for all alloys. It can be observed that, compared to its hot-rolled counterpart, the alloys produced by L-PBF present higher hardness values.

In addition, regarding the LPBF-produced alloys, the hardness further increases with the boron addition.

There are some mechanisms that may affect the hardness of the studied alloys, including grain size, solid solution strengthening, secondary phase formation, and dislocation strengthening [17, 56, 85]. Firstly, as showed in Section 5.3, alloys produced by L-PBF present a high residual stress and high dislocation density associated to the fast heating and cooling cycles during L-PBF [48, 49], which is responsible for increasing the hardness by restricting the dislocations movement. Moreover, compared to the conventional dual-phase microstructure present in the hot-rolled SAF 2205 DSS (Fig. 5.13), the L-PBF-printed alloys present a single δ-ferritic matrix, whereby a significant solid solution strengthening is expected, due to the supersaturation of substitutional and interstitial alloying elements (e.g., Cr, Ni, Mo, B, N) in the δ-Fe.

Furthermore, the additional hardness increase observed for the L-PBF-produced boron-modified alloy is attributed to the formation of a microstructure composed of ultrafine grains with Cr_2B nanoborides within and along the GBs. Since grain size is one of the most dominant effects to increase hardness due to the Hall-Petch relation, this in synergy to the presence of hard and rigid reinforcement particles, contributes to the dislocation pinning [92, 93] thereby increasing hardness.

For comparison purposes, the enhanced hardness exhibited by the boron-modified alloy in this work (~450 $HV_{0.5}$ accordingly to Fig. 5.14a) is comparable to those found in hard and wear-resistant alloys, such as wrought cobalt-based Stellite 6 (~500 – 600 $HV_{0.5}$) [92], PTA-produced superduplex stainless steel (SDSS) modified with 3 wt.% of B (580 $HV_{0.5}$) [8], HVOF-produced coating of supermartensitic stainless steel modified with 0.7 wt.% of B (~500 $HV_{0.3}$) [12], and L-PBF-printed nanocomposites formed by 316L/B (~400 $HV_{0.5}$) [26], 316L/SiC (~500 $HV_{0.3}$) [93], Fe/TiB_2 (~380 $HV_{0.5}$) [85], and 316L/ TiB_2 (~600 $HV_{0.1}$) [94]. Therefore, even a relatively small amount of boron proved to be effective in significantly increasing the hardness of stainless steels obtained by L-PBF using pre-alloyed powder.

The specific wear rate values were ~3×10^{-3}, ~3×10^{-4} and ~4×10^{-5} $mm^3.N^{-1}.m^{-1}$ for the hot rolled SAF 2205, Pure-LPBF, and 0.6B-LPBF specimens, respectively. It can be seen that the wear resistance in sliding condition follows the same trend as hardness, which is expected, since both properties may be closely related depending on the wear condition. In other words, the results indicated that the wear resistance is improved as hardness increases. However, baselined against the hot-rolled SAF 2205, it is observed a 10-fold and 70-fold decrease of κ for L-PBF-produced SAF 2205 and SAF 2205 + B, respectively, for a ~1.4-fold and ~2.0-fold increase in hardness, respectively. Thus, the wear resistance improvement was much more sensitive to the microstructure than the hardness.

Recent findings [51, 52, 77] demonstrate that, compared to its wrought counterpart, DSSs obtained by L-PBF in its as-built condition (i.e., completely δ-ferritic) exhibit higher hardness, yield strength and ultimate tensile strength, which are related to the higher residual stress and solid solution strengthening. Also, although ferrite is as hard as austenite in DSSs, it is reported that ferrite is more rigid [95], being favorable to reduce the contacting area during sliding wear, which may also be related to the higher wear resistance of the alloys produced by L-PBF in contrast to the hot rolled SAF 2205. Similar results are reported for as-built DSS obtained by L-PBF [56].

The further wear resistance increase is associated to the boron addition, since one of the main goals of incorporating borides in stainless steels is to improve their wear resistance by producing an effective barrier against material removal from the relatively soft matrix, as shown in previously findings [3, 4, 6, 8, 11, 12, 29]. Therefore, it is assumed that the addition of boron in the stainless steel obtained by L-PBF generated two effects responsible for the enhanced wear resistance: the reduction of grain size and the formation of reinforcement of hard particles. Moreover, the specific wear rate of the current stainless steel modified with 0.6 wt.% of boron is comparable to those found for boron-modified stainless steel coatings obtained by L-PBF [29]. Likewise, these results are aligned with investigations into the mechanical and wear behaviour of L-PBF-produced nanocomposites (e.g., 316L/TiB_2 [94], 316L/SiC [93]), demonstrating an increase

in hardness and strengthening, being simultaneous to a reduction in the coefficient of friction and specific wear rate as the grains size reduces and the nanoparticles fraction increases.

From Fig. 5.14b, it can be seen that the boron-modified alloy exhibited the lowest COF value, since the friction characteristics of boron-modified steel ensure the separation of the cooperating areas of the surface layer (inferior contacting area) and reduce the rate of direct adhesion between the surface and irregularities [29, 96], being also related to lower material loss during sliding.

To discuss the wear mechanisms, the worn surfaces of the tested alloys and the respective Al_2O_3-pins used in the wear tests are shown in Fig. 5.15.

The presence of refined and rigid borides within the microstructure protects the matrix from excessive material removal [29], resulting in a clearly smaller wear track thickness for the boron-modified alloy (Fig. 5.15c). On the other hand, for the boron-free alloys produced by hot rolling and L-PBF, the wear tracks are larger and present basically the same thickness (Figs. 5.15a, b), but shallow for the alloy obtained by L-PBF (see Figs. 5.15g, h, i, j). Thus, upon sliding, the effective contact area between the counter-body pin and the worn track is the highest for the SAF 2205 produced by hot-rolling and the lowest for the L-PBF-produced boron-modified alloy, which reflects on the COF values.

Furthermore, as pointed out in Figs. 5.15d, e, g, h oxidation, plastic deformation and scratches occurred during the wear testing, being more pronounced for the boron-free stainless steels obtained by hot rolling and L-PBF, suggesting the occurrence of a more severe adhesive and abrasive wear behaviour (see EDX analysis present in Fig. 5.15q). In contrast, the boron-modified alloy (Fig. 5.15f) exhibits a much smoother worn surface with small cracks and shallow scratches formed during the wear testing, with low amount of oxidation (Fig. 4i) and plastic deformation. This indicates that the dominating wear mechanism was altered to slight abrasive wear, whereby this change in the wear mode may be related to the higher hardness and strengthening ascribed to the refined microstructure and borides formation (Figs. 5.15c-f).

The presence of high Fe and Cr content on the surface of the Al_2O_3-pins (Fig. 5.15q) confirms the abrasive and adhesive mechanisms of wear for the

tested alloys (Figs. 5.15n-p). Moreover, compared to other conditions (Figs. 5.15k, l), a lower metal amount attached on Al_2O_3-pin slid in comparison to the boron-modified alloy is seen (Fig. 5.15m), which is expected since less material is removed from it, being part adhered on the pin surface. These results further emphasizes that the boron-modified alloy present a better wear resistance, being consistent to the highest hardness and lowest average specific wear rate (Fig. 5.14a).

The different extension on wear mechanisms of the studied alloys results in different tribological performance. On the one hand, for pure stainless steels produced by hot-rolling and L-PBF, it is suggested that in the early stage of the sliding wear process, the surfaces are prone to oxidized after adhesive wear, especially due to the high content of alloying elements in solid solution with high affinity with oxygen (e.g., Cr, Ni, Mo). As the sliding wear process goes on, the oxide layer between the alloy's surface and the pin-tip is fractured and the debris are added into the tribosystem, resulting in scratches on the worn surfaces. On the other hand, besides the enhanced hardness and strengthening induced by boron addition, it is proposed that the boride particles acted as hard-skeleton support during sliding wear process, enabling the load transfer from the relatively soft δ-Fe matrix to the hard Cr_2B reinforcement, further preserving the matrix from being severely scratched by the debris. Similar mechanisms were reported for different additively manufactured nanoparticles-reinforced stainless steel under sliding wear condition [93, 94].

The analyzes indicated that the wear mechanisms are a mixture of oxidative, abrasive, and adhesive wear for the all studies alloys, being more prominent for the alloys without boron addition. For the boron modified alloy, the dominant wear mechanism seems to be abrasive wear, with a minor role of oxidative and adhesive wear components.

Thus, a hard and wear-resistant boron-modified stainless steel were successfully obtained by L-PBF, demonstrating that the wear resistance in sliding mode can be substantially increased by adding small content of boron to stainless steels manufactured by L-PBF.

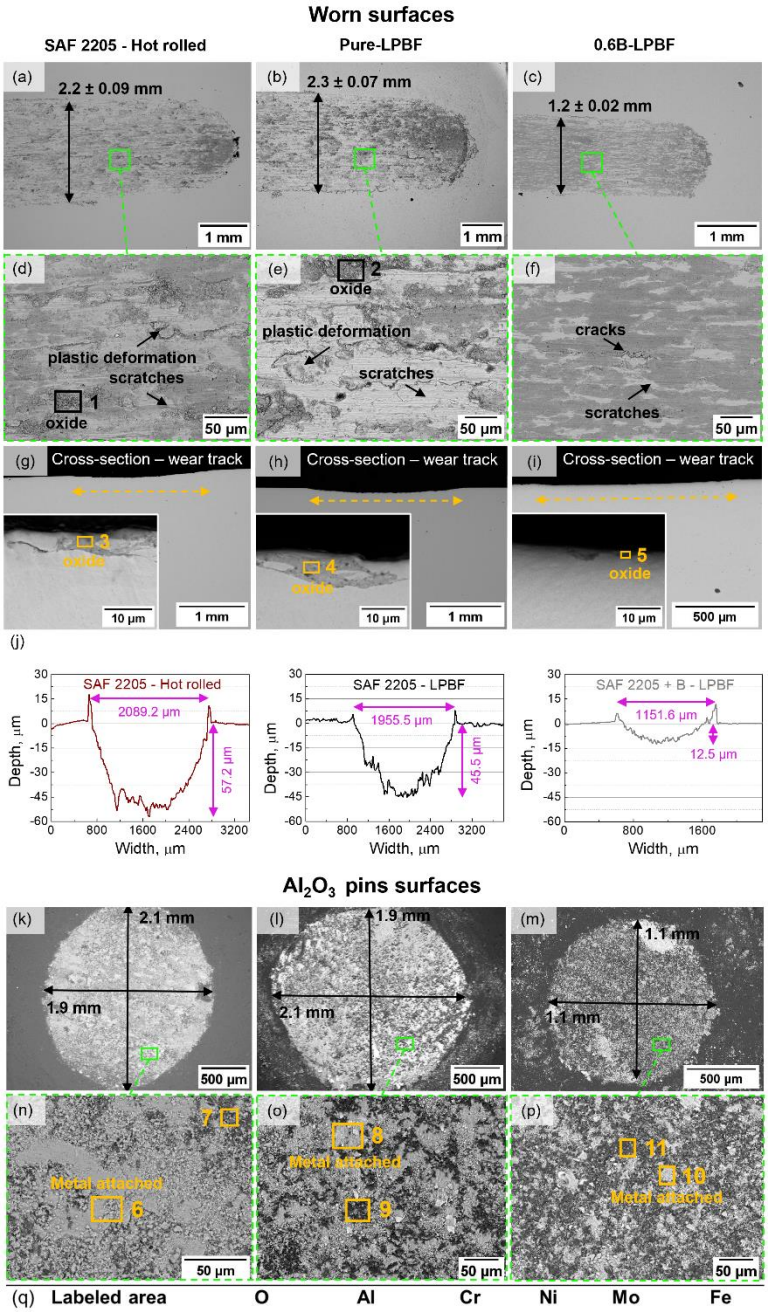

(q)

Labeled area	O	Al	Cr	Ni	Mo	Fe
1	12	7	18	4	1	58
2	15	7	17	4	2	55
3	22	5	22	1	4	46
4	17	5	17	4	2	55
5	14	1	21	5	2	57
6	3	1	21	4	2	69
7	23	58	3	1	-	15
8	14	5	18	4	1	58
9	29	66	1	1	-	3
10	13	9	20	4	1	53
11	41	54	1	-	1	3

Figure 5.15 - SEM micrographs of the worn surfaces of the (a, d) SAF 2205, (b, e) Pure-LPBF, (c, f) 0.6B-LPBF specimens. SEM micrographs of cross-section of

the wear tracks of (g) SAF 2205, (h) Pure-LPBF, and (i) 0.6B-LPBF specimens. (j) Representative wear track profiles of the tested specimens after pin-on-plate measurement. SEM micrographs of the Al_2O_3-pins used to wear tests of (k, n) SAF 2205, (l, o) Pure-LPBF, (m, p) 0.6B-LPBF specimens. (q) EDX results (in wt.%) of the labeled areas in Figs. 5.15d, e, g-i, n-p.

5.5 Electrochemical behavior of the L-PBF-produced alloys

This section is dedicated to evaluate the corrosion behavior in chloride electrolyte of the L-PBF-produced stainless steel modified with 0.6 wt.% of boron. Therefore, its electrochemical behavior was assessed by electrochemical impedance spectroscopy, cyclic potentiodynamic polarization, and double-loop electrochemical potentiokinetic reactivation tests. The results were contrasted to those exhibited by the boron-free alloys obtained by L-PBF and hot-rolling (i.e., Pure-LPBF and SAF 2205 DSS).

Figure 5.16 shows the EIS data as Nyquist and Bode plots for the L-PBF-produced alloys, and hot rolled SAF 2205. Table 5.2 presents the results from adjusting the experimental impedance results, $Z_{(\omega)exp}$, to the impedance of the equivalent circuit, $Z_{(\omega)EC}$.

A hierarchically arranged two-time constant equivalent circuit shown in Fig. 5.16a was used as representative of the interfacial electrochemical processes, which is based on [14, 56] on corrosion in 0.6M NaCl electrolyte of a duplex and ferritic stainless steels manufactured by L-PBF. The followed resistors R_s, R_f, and R_{ct} in Fig. 5.16a correspond to the electrolyte, passive film, and charge transfer resistances, correspondingly. The constant phase elements, CPE_{dl} and CPE_f, represent the capacitive-like responses assigned to the double layer and the passive film, respectively. Instead of a pure capacitance, C, CPE element (parameter (Q) and exponent (α)) was used to describe the non-ideal capacitive behavior of the interface, which may be related to micro defects (impurities, porosity, and roughness) [14, 56, 97].

It can be seen in Fig. 5.16b that the Nyquist diagrams show similar shape of capacitive loops, which is an indicative of a similar general corrosion behavior for all-tested alloys. Nonetheless, the Pure-LPBF specimen presents a larger

semi-circle diameter compared to the hot rolled SAF 2205 and 0.6B-LPBF specimens, being an indicative of a higher corrosion resistance [14, 56].

Moreover, Figs. 5.16c, d show the Bode plots for the tested specimens. It can be seen that the electrolyte resistance (R_s) values at high-frequency (10^5 – 10^3 Hz) are ~30 Ω cm^2 (Table 5.2) and which is expected due to the high content of mobile ions such as Na^+ and Cl^- in solution [14, 56]; also, at high-frequency, the phase angle is close to 0° (Fig. 5.16d).

At the lowest frequency (10^{-2} Hz), SAF 2205 (hot rolled), Pure-LPBF, and 0.6B-LPBF specimens present impedance values of 282, 438, and 317 kΩ cm^2, respectively (Fig. 5.16c). By Fig. 5.16d, it is observed that all tested specimens exhibit a constant phase angle lower than -80° over a wide frequency range (around 10^{-1} – 10^1 Hz), which is similar to highly passivated iron-based alloys [39, 98]. It suggests that the studied alloys present a highly stable passive film. Therefore, together with the double-layer, the behavior presented in Fig. 5.16d indicates that the protecting layer forming on the tested alloys results in a clear capacitive-like response from the surface.

As previously mentioned, the electrochemical parameters from the equivalent circuit (EC) fitting can be seen in Table 5.2. As it can be seen, all tested alloys demonstrated high corrosion resistance in 0.6 M NaCl electrolyte, being ascribed to their high values of passive film (R_f) and charge transfer (R_{ct}) resistances. The Pure-LPBF specimen displayed slightly higher values of resistances (R_f = 8.7×10^5 Ω cm^2, R_{ct} = 5.6×10^5 Ω cm^2) compared to the 0.6B-LPBF (R_f = 1.8×10^5 Ω cm^2, R_{ct} = 4.7×10^5 Ω cm^2), and hot rolled SAF 2205 (R_f = 2.1×10^5 Ω cm^2, R_{ct} = 2.7×10^5 Ω cm^2) specimens. All specimens presented clear capacitive-like behavior as indicated by α values (near 1), and the Q values are typical to those reported in literature [99, 100]. Besides, the measured error values are low ($\chi^2 \leq 10^{-2}$), indicating that the proposed equivalent circuit is adequate to represent the corroding interface.

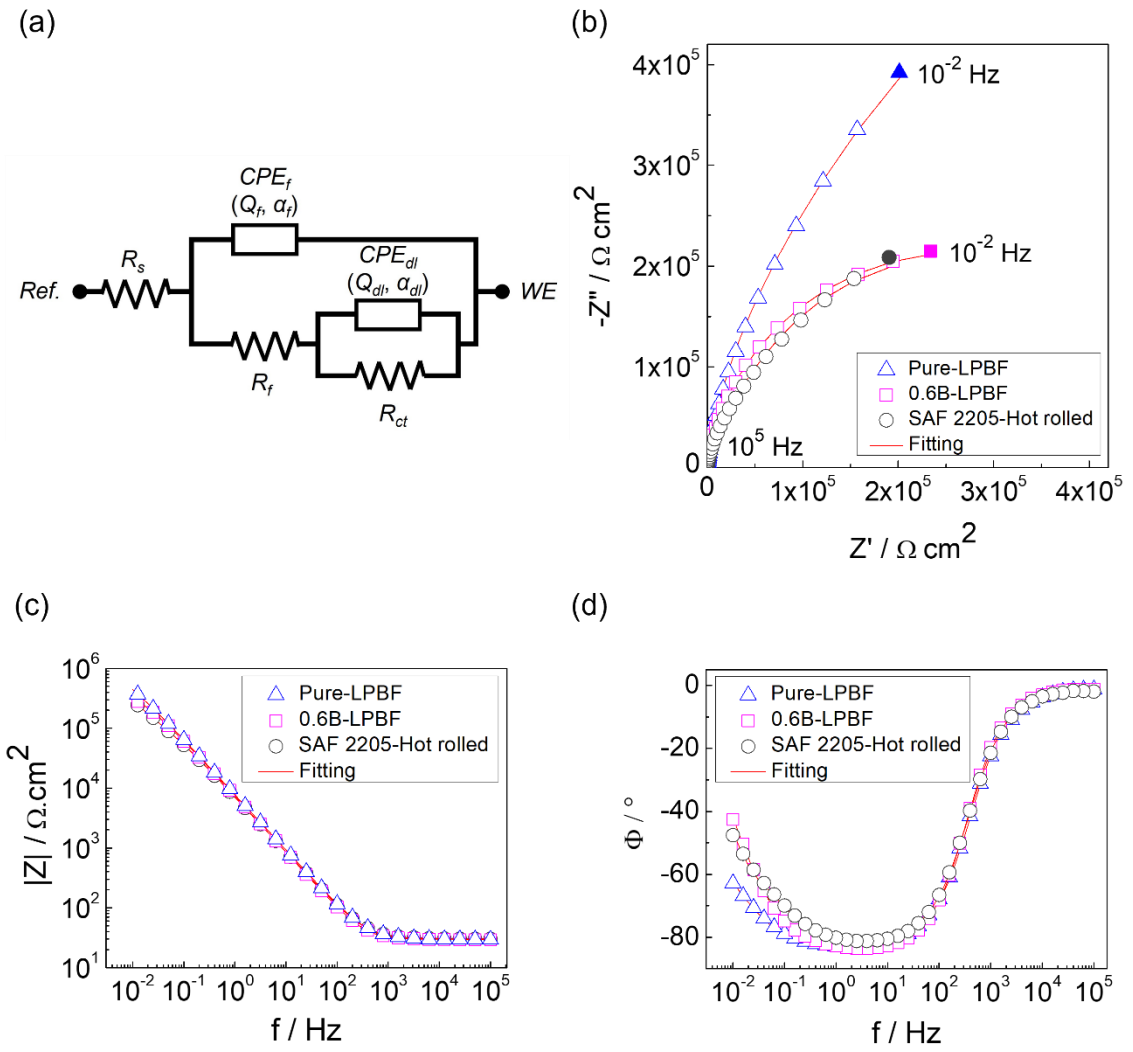

Figure 5.16 - EIS data for the L-PBF-processed specimen, and SAF 2205 hot rolled illustrating (a) equivalent electrical circuit used to model EIS data, (b) Nyquist diagram, (c) impedance Bode plot, and (d) phase angle plot. 0.6 M Tests carried out under 0.6 M NaCl solution.

Table 5.2 - EIS data relating equivalent circuit and corrosion parameters of hot rolled and L-PBF-produced alloys.

Alloy	R_s / Ω cm²	R_f / Ω cm²	R_{ct} / Ω cm²	R_p / Ω cm²	Q_f / μF $s^{(\alpha f-1)}$	α_f	Q_{dl} / μF $s^{(\alpha f-1)}$	α_{dl}	χ^2 / |Z|
SAF 2205	30.5	2.1×10^5	2.7×10^5	4.9×10^5	10.4	0.9	11.1	0.9	1.1×10^{-2}
Pure-LPBF	29.9	8.7×10^5	5.6×10^5	1.4×10^6	7.1	0.9	9.6	1.0	1.2×10^{-2}
0.6B-LPBF	29.5	1.8×10^5	4.7×10^5	6.5×10^5	7.2	0.9	1.5	0.4	3.9×10^{-3}

To further investigate the electrochemical behavior, cyclic potentiodynamic polarization (CPP) tests were performed to evaluate the repassivation ability once the passive film breaks down at high anodic potentials. Figure 5.17 shows the cyclic potentiodynamic polarization (CPP) curves of the studied alloys under 0.6M NaCl test electrolyte. The corrosion potential (E_{corr}), corrosion current density (i_{corr}), transpassive potential (E_{transp}), and repassivation potential (E_{rep}) are detailed in Table 5.3.

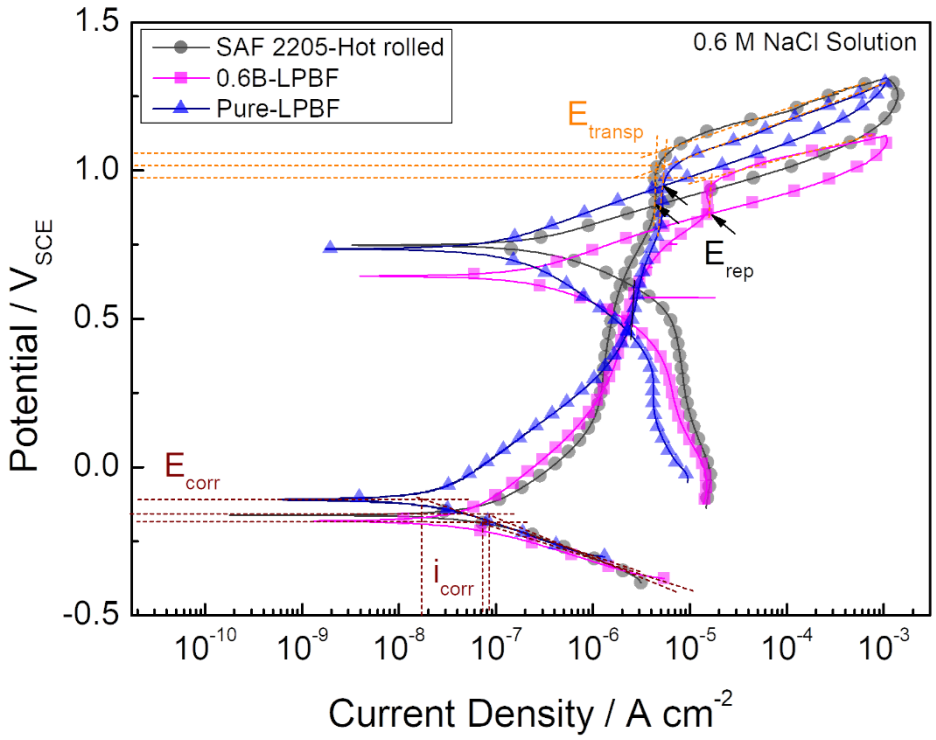

Figure 5.17 - Potentiodynamic polarization curves in 0.6M NaCl solution of L-PBF specimens and SAF 2205. Electrochemical parameters: Corrosion potential (E_{corr}), corrosion current density (i_{corr}), transpassivation potential (E_{transp}), repassivation potential (E_{rep}).

Table 5.3 - Summary of the electrochemical parameters from CPP curves in Fig. 5.17. Corrosion data reported in the literature for duplex and ferritic stainless steels using a similar electrochemical approach.

Alloys	**E_{corr} (V_{SCE})**	**E_{transp} (V_{SCE})**	**E_{rep} (V_{SCE})**	**i_{corr} (A/cm^2)**	**i_{pass} (A/cm^2)**	**$E_{transp} - E_{corr}$ (V_{SCE})**
SAF 2205[1]	-0.2 ± 0.01	1.1 ± 0.04	0.9 ± 0.01	9.3×10^{-8} ± 7.0×10^{-9}	1.4×10^{-6} ± 1.3×10^{-7}	1.2 ± 0.04
Pure-LPBF[1]	-0.1 ± 0.04	1.0 ± 0.02	0.9 ± 0.01	2.1×10^{-8} ± 1.3×10^{-8}	2.3×10^{-6} ± 8.3×10^{-7}	1.2 ± 0.06
0.6B-LPBF[1]	-0.2 ± 0.04	1.0 ± 0.02	0.8 ± 0.003	7.1×10^{-8} ± 2.3×10^{-8}	1.8×10^{-6} ± 1.0×10^{-7}	1.1 ± 0.07
UNS31803 LPBF [77]	0.1	1.0	0.7	7×10^{-9}	-	0.6
UNS31803 LPBF + HT [77]	-0.1	1.0	0.8	1×10^{-8}	-	0.9
S31803 LPBF [62]	-0.28	1.1	-	3×10^{-6}	-	-
2205 LPBF [56]	-0.2	1	-	2×10^{-7}	5×10^{-6}	-

2205 LPBF [61]	-0.1	1.1	-0.2	0.5×10^{-6}	-	0.1
25Cr7Ni LPBF [61]	-	1.1	-	1×10^{-7}	-	-
2507 LPBF [39]	-0.4	0.5	-0.6	1×10^{-5}	-	0.2
2507 LPBF [64]	-0.22	0.1	-	1.4×10^{-7}	-	-
2507 LPBF+HT [64]	-0.3	-0.1	-	3.2×10^{-7}	-	-
FSS LPBF [14]	-0.1	0.6	-	0.5×10^{-6}	-	-

[1] Data obtained in this work.

Corresponding to Table 5.3 and Figure 5.17, the corrosion behaviors are comparable for the three specimens. The corrosion current density (i_{corr}) values are low, in the order of 10^{-8} A/cm^2. A large passivation window (E_{transp}-E_{corr}) can be seen, which is ~1.2 V_{SCE}; and the transpassivation potential (E_{transp}) values for the three alloys are higher than 1.0 V_{SCE}, showing their high passivation stability. Moreover, during the backward scan, for the three tested alloys, the current density (i_{corr}) decreases as the potential declines, wherein the polarization curves form a positive but narrow hysteresis, indicating fast repair of the passive film with small degree of accelerated corrosion due to the repassivation process that occurs at high potential values (~0.9 V) close to E_{transp}.

For comparison purposes and being tested under similar conditions, Table 5.3 also presents corrosion results reported in literature to FSS obtained by L-PBF [14], DSSs/SDSSs obtained by L-PBF in its fully ferritic state [39, 56, 61, 62, 64, 77, 101], and DSSs/SDSSs produced by L-PBF and heat treatment (HT) to recover the duplex microstructure [64, 77].

Regarding E_{corr} and i_{corr}, the alloys obtained in this work present similar or superior corrosion resistance in respect to those reported in literature [14, 39, 56, 61, 62, 64, 77, 101], regardless of the heat treatment applied to recover the duplex microstructure. Thus, it is an indication that recovering the duplex microstructure is not mandatory to achieve great corrosion resistance under chloride solution.

The localized corrosion resistance is an important corrosion property for stainless steels since its passive film may break down due to mechanical impact or friction in service-life of a component [61]. Therefore, the high repassivation

ability exhibited by the L-PBF-produced alloys indicates that these alloys present a great potential to be used in harsh-environmental applications. Few studies involving L-PBF-manufacturing DSSs/SDSSs have evaluated repassivation behavior through CPP test; the reported literature [39, 61] indicates that DSSs and SDSSs present difficulties of repassivation in chloride media after the formation of a stable pit, with repassivation being enhanced after recovery of the dual-phase microstructure by heat-treatment. However, the excellent repassivation ability as demonstrated by the alloys studied in this work was also previously reported for a as-built DSS [77], which was ascribed to the fast cooling in L-PBF that consequently leads to the formation of a single δ-Fe phase highly alloyed with Cr, Ni, and Mo in solid solution, far beyond the typical values found for conventional ferritic stainless steels.

It is important to point out that the tested SAF 2205 obtained by hot rolling presents a conventional balanced duplex microstructure (α-ferrite + γ-austenite), as shown in Fig. 5.13; on the other hand, the pure and boron-modified alloys obtained by L-PBF present a fully δ-ferritic single phase due to the L-PBF solidification aspects. Additionally, unlike the Pure-LPBF which presents relatively coarse columnar δ-Fe grains, the boron-modified alloy is composed of fine δ-Fe grains with Cr-rich nanoborides decorating the GBs (see Figs. 5.8, and 5.11). Despite the studied alloys presenting a completely different microstructure with benefits to the tribological properties, the corrosion behavior was similar. It is known that microstructural features may affect the corrosion resistance, such as porosity, cracks, GBs, secondary phase, chemical composition, etc.; thus, the behavior of the alloy in a corrosive environment is dependent on several contributions.

Although both alloys produced by L-PBF present a fully δ-ferritic microstructure, they do not electrochemically behave as ferritic stainless steels, since their chemical composition is similar to that presented by DSSs. Thus, the as-built Pure-LPBF and 0.6B-LPBF alloys produced from a DSS present a matrix supersaturated of Cr, Ni, and Mo, since there is not partitioning of alloying elements between α-ferrite and γ-austenite, such as in conventional dual-phase DSSs [56, 77].

Moreover, the pitting resistance equivalent number (PREn = Cr + 3.3 Mo + 16 N) may give some insights about the capacity of an alloy to resist pitting; both L-PBF-produced alloys present a PREn ~ 32, being similar to the hot rolled SAF 2205 and much superior compared to conventional ferritic stainless steels (FSS), including those containing Mo, such as the 444-grade SS (PREn ~ 28 max. [14]). Therefore, this study reveals that the proportion of phases is not the unique factor in determining the corrosion resistance of DSSs. Furthermore, the elevated PREn is sufficient to ensure a spontaneous and effective passive film formation in chloride-containing solution.

It is also reported that alloys with high density dislocations (such as L-PBF-produced alloys) may have their corrosion resistance increased, since dislocations may act as “short path for diffusion” that increase diffusion kinetics, thus Cr and Mo diffuse more easily to promote a quick formation of a dense passive film on the metal’s surface [62]. Therefore, the high number of dislocations present in the L-PBF-produced alloys (see Fig. 5.10d) may facilitate the alloy’s passivation ability.

Distribution of alloying elements usually affects the passivity and corrosion resistance of stainless steels. The formation of Cr-rich borides in the δ-Fe matrix of 0.6B-LPBF alloy results in the consumption of Cr, which may be responsible for the formation of Cr depleted zones neighboring the precipitates. However, despite the presence of Cr_2B nanoparticles, the boron-modified alloy shows strong passivation ability over a wide range of applied potentials; thus, it can be seen that the pitting initiation is not significantly influenced by these particles. Moreover, as expected given the high chromium content in the alloy (>20 wt.%), the results indicate that the chromium content in matrix is sufficient to allow the formation of a stable passive film and still grant it as stainless.

Additionally, the electrochemical behavior may be affected by grain refinement; however, there is not a unified theory to explain the relationship between grain refinement and corrosion [102, 103], in which contradictory results are reported. Studies indicate that the grain refinement and consequent increase in GBs area may improve the chromium and molybdenum diffusion and promote the formation of compact passive film in refined FSS and DSS [103, 104]. For the

boron-modified alloys evaluated in this work, it is challenging to separate the effects of grain refining and formation of chromium-rich nanoparticles. However, as can be seen by EIS and CPP analysis, although its corrosion resistance is slightly lower compared to the boron-free stainless steel obtained by L-PBF, it can be inferred that the corrosion performance was not significantly affected by the grain refinement and the nanoborides formation.

SEM micrographs of the corroded surfaces after CPP tests are shown in Fig. 5.18. Pitting was observed for the three tested alloys. The hot rolled SAF 2205 exhibited smaller and shallow pitting (Figs. 5.18a, b), which may be related to inhibition of the pitting propagation by fast repassivation in the reverse scan. For the alloys obtained by L-PBF (Figs. 5.18c-f), the pits are relatively shallow and present larger surface areas compared to SAF 2205, indicating that the pitting propagation was interrupted after the initiation due to the repassivation process.

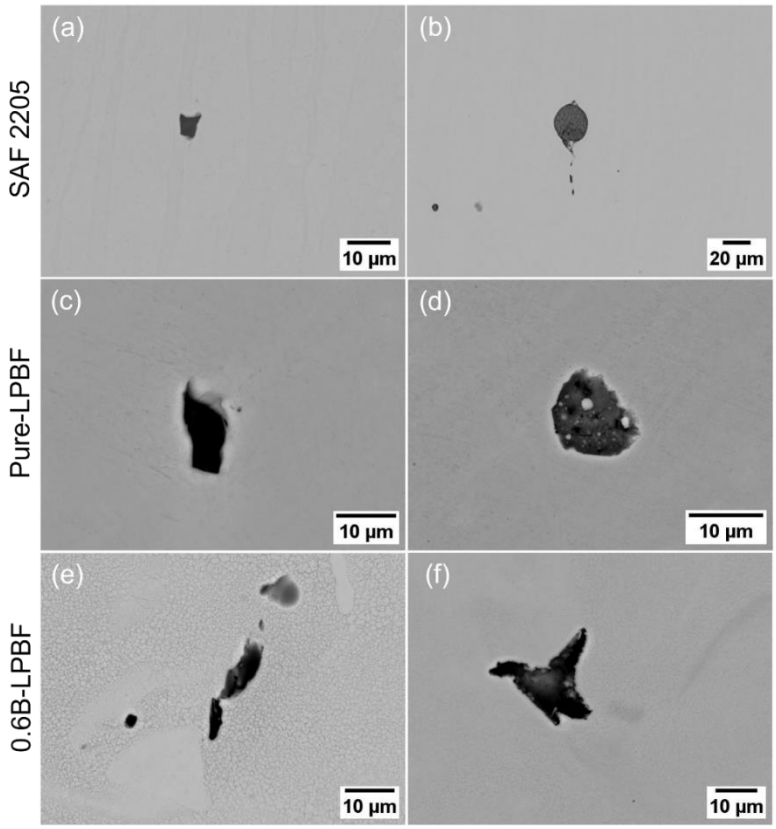

Figure 5.18 - SEM micrographs of the (a, b) SAF 2205, (c, d) Pure-LPBF, and (e, f) 0.6B-LPBF specimens after cyclic potentiodynamic polarization tests.

Figure 5.19 shows the degree of sensitization (DOS) of the studied alloys, which was assessed from DL-EPR testing.

Sensitization in stainless steels is related to the precipitation of chromium-rich carbides along the GBs, promoting the formation of Cr-depleted regions [105, 106] and consequently increasing the susceptible to intergranular corrosion (IGC). Although DSSs present an excellent corrosion resistance in the presence of chloride ions [2], precipitation of deleterious phases in the matrix (e.g., chromium carbide or other Cr-rich phases) may occur under service-life, post heat-treatment, and fusion welding process (at 623 – 1273 K) [107]. Moreover, sensitization is a risk in alloys produced by L-PBF given the repeated heat input from subsequently added layers, which may be responsible for inducing elemental heterogeneities and precipitation of deleterious phases [2, 108].

The ratio of the peak current densities in the reverse and forward directions denotes the degree of sensitization (DOS), which is a quantitative measure of the harshness of the grain boundary depletion of chromium [74]. However, no reactivation peak was observed for the tested alloys, which is an indicative of unsensitized microstructures. Therefore, despite the formation of Cr-rich borides along the GBs, the results indicate that there was no significant formation of chromium-depleted regions susceptible to intergranular corrosion (IGC). This may be related to the fact that alloys produced by L-PBF have a high density of dislocations, which can facilitate the diffusion of solutes, allowing chromium-poor regions to be replenished by chromium diffusion during the numerous heating and cooling rounds that the solidified layers are submitted during 3D printing, attenuating the elemental partitioning.

Another important aspect is the charge upon the activation scan before the steep decrease of current density, regarded as the critical charge for effective passive film formation. The SAF 2205 presented the highest charge for passivation (5.2×10^{-5} A/mV), followed by the Pure-LPBF (2.4×10^{-5} A/mV) and 0.6B-LPBF (1.9×10^{-5} A/mV). The lowest charge of the 0.6B-LPBF points out to a easier transition between the active to passive region that could be related, as mentioned earlier, by the higher density of dislocations and grain boundaries

surface acting as shortcut for rapid diffusion of alloying elements for passive film formation.

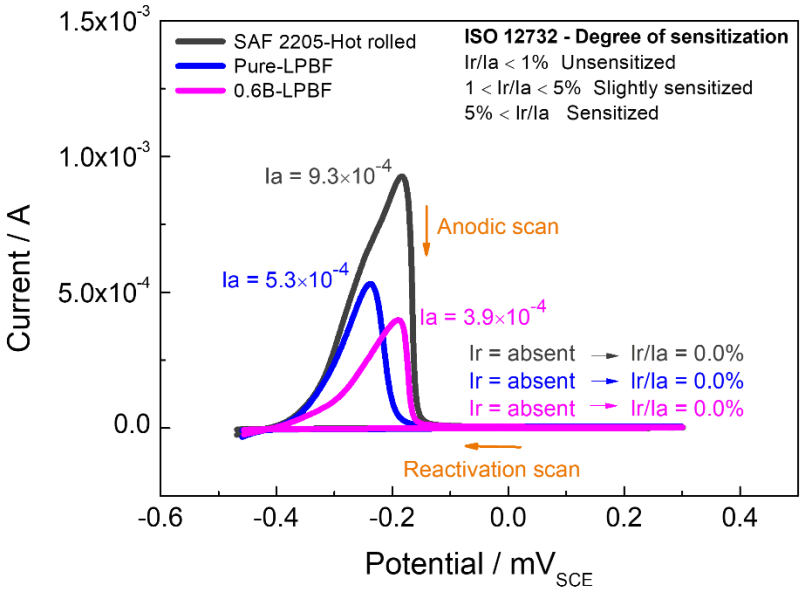

Figure 5.19 - Degree of sensitization (DOS) of the specimens assessed from double-loop electrochemical potentiokinetic reactivation (DL-EPR) test. Inserted information indicating the general interpretation of DOS from the Ir/Ia (%) values corresponding to the ISO 12732 [74].

In summary, although DSSs are theoretically not applied in their fully ferritic state, these alloys have great potential of application given their high pitting resistance, great repassivation ability, and absence of sensitization that may be caused by deleterious precipitates. Besides the corrosion resistance, as-built ferritic-induced stainless steels obtained from a DSS present high strength and hardness compared to its heat-treated condition.

Therefore, the addition of boron results in the formation of a refine-grained DSS alloy with further enhanced hardness, wear resistance, and excellent corrosion resistance. There is an industrial demand for advanced materials that are produced on request, in order to minimize the stock and reduce material waste. Therefore, the manufacturing by L-PBF of corrosion- and wear-resistant ferritic-induced stainless steels with nanoborides decorating GBs proves to be feasible, which have potential to be applied to components subjected to

challenging environments where high corrosion and wear resistances are required, such as impellers and valves used in petrochemical and marine industries.

6 CONCLUSIONS

For the first time, boron-modified stainless steels were produced by L-PBF. The solidification mechanisms, hardness, wear and corrosion behavior were systematically evaluated, resulting in the following conclusions:

(i) Dense and crack-free boron-modified stainless steel and boron-free stainless steel were successfully produced by L-PBF. The use of design of experiments tools are helpful to produce boron-modified stainless steel specimens with a relatively low number of experiments, identifying a narrow optimized processing window to build bulk composite materials.

(ii) Boron is very efficient to promote outstanding grain refinement in stainless steels produced by L-PBF, allowing the production of an extremely refined microstructure composed of δ-Fe grains and Cr_2B nanoborides decorating GBs.

(iii) Considering the L-PBF solidification aspects, a hypothesis is that the grain refinement is ascribed to an extended thermal undercooling generated by a lag between the real and theoretical growth rate, which may be credited to the accumulation of a boron-enriched boundary layer ahead of the S/L interface, which reduces the solidification front velocity.

(iv) L-PBF-produced alloys (boron-free and boron-containing) present higher hardness and wear resistance in sliding mode compared to hot rolled SAF 2205 DSS. The addition of boron further increases the hardness and wear resistance ascribed to the formation of Cr_2B nanoborides at GBs.

(v) Both pure and boron-containing alloys produced by L-PBF presented excellent corrosion resistance in chloride media, being comparable to commercial hot rolled SAF 2205 DSS. The L-PBF-produced alloys exhibit high pitting resistance, and great repassivation ability, which is extremely important, since the passive film of stainless steels may break in the component service-life. The absence of sensitization suggests that chromium-rich precipitates did not negatively affect the corrosion resistance.

(vi) As-built duplex stainless steel obtained by L-PBF presents excellent corrosion and wear resistances, which opens up the possibility of applying

this material in its completely ferritic state, without the need for heat treatment.

(vii) Microstructural characteristics presented by the L-PBF-produced boron-modified stainless steel are extremely desirable for numerous applications, since refined grains and absence of crystallographic texture may potentially minimize hot-cracking susceptibility and anisotropy.

All in all, L-PBF proved to be a very interesting technique to produce stainless steels modified with boron, as it results in fine-grained material with high hardness, and excellent wear and corrosion resistance; being a prospective candidate for use in applications where high wear and corrosion resistances are required.

7 RECOMMENDATIONS FOR FUTURE WORKS

(i) Perform heat treatments to recover the duplex matrix, and evaluate its microstructure, wear and corrosion behavior of the L-PBF-produced alloys.

(ii) Since ferritic stainless steel is more resistant against stress corrosion cracking, evaluate this property for the 0.6B-LPBF alloy.

(iii) Evaluate the tensile and impact toughness of the boron-modified alloys.

(iv) Perform tribological tests to evaluate the behavior of the material in face of the synergistic process of wear and corrosion (tribocorrosion).

(v) Produce stainless steels with different boron content by L-PBF, including hypereutectic compositions.

(vi) Produce different grades of boron-modified stainless steels by L-PBF and evaluate their properties.

(vii) Evaluate the feasibility of building parts with complex geometries using the studied alloys, given the numerous challenges related to complex thermal cyclic of L-PBF process.

8 REFERENCES

[1] M. Maher, I.I. Arregui, H. B. Youcef, B. Rhouta, V. Trabadelo. The synergistic effect of wear-corrosion in stainless steels: A review. Materials Today Proceedings, v. 51, 6, 1975-1990, 2022. Doi: 10.1016/j.matpr.2021.05.010

[2] R.N. Gunn. Duplex Stainless Steels: Microstructure, Properties and Applications (third ed.), Abington Publishing, Woodhead publishing Ltd, 1997. Doi: 10.1533/9781845698775

[3] J. Soyama, T. P. Lopes, G. Zepon, C.S. Kiminami, W.J. Botta, C. Bolfarini. Wear Resistant Duplex Stainless Steels Produced by Spray Forming. Metals and Materials International, v. 25, 456–464, 2019. Doi: 10.1007/s12540-018-0202-8

[4] J. Soyama, G. Zepon, T.P. Lopes, L. Beraldo, C.S. Kiminami, W.J. Botta, C. Bolfarini. Microstructure formation and abrasive wear resistance of a boron-modified superduplex stainless steel produced by spray forming. Journal of Materials Research., v. 31, 19, 2016. Doi: 10.1557/jmr.2016.323

[5] G. Zepon, N. Ellendt, V. Uhlenwinkel, C. Bolfarini. Solidification Sequence of Spray-Formed Steels, Metallurgical and Materials Transactions A, 842 v. 47A, 2016. Doi: 10.1007/s11661-015-3253-1

[6] G. Zepon, A.R.C. Nascimento, A.H. Kasama, R.P. Nogueira, C.S. Kiminami, W.J. Botta, C. Bolfarini. Design of wear resistant boron-modified supermartensitic stainless steel by spray forming process. Materials & Design, v. 83, 214–223, 2015. Doi: 10.1016/j.matdes.2015.06.020

[7] G. Zepon, R.P. Nogueira, C.S. Kiminami, W.J. Botta, C. Bolfarini. Electrochemical Corrosion Behavior of Spray-Formed Boron-Modified Supermartensitic Stainless Steel. Metallurgical and Materials Transactions A, v. 48A, 2017-2077, 2017. Doi: 10.1007/s11661-017-3980-6

[8] E. Sigolo, J. Soyama, G. Zepon, C.S. Kiminami, W.J. Botta, C. Bolfarini. Wear resistant coatings of boron-modified stainless steels deposited by Plasma Transferred Arc. Surface & Coatings Technology, v. 302, 255–264, 2016. Doi: 10.1016/j.surfcoat.2016.06.023

[9] E.R. Santos, W.A. Silva, G.Y. Koga, C. Bolfarini, G. Zepon. Corrosion Resistant Boron-Modified Ferritic and Austenitic Stainless Steels Designed by

CALPHAD. Metallurgical and Materials Transactions A, 2708, v. 52A, 2021. Doi: 10.1007/s11661-021-06226-4

[10] T.P. Lopes, J. Soyama, G. Zepon, A.R. C. Nascimento, A. Costa e Silva, C.S. Kiminami, W.J. Botta, C. Bolfarini. Thermodynamic Calculations for the Investigation of Phase Formation in Boron-Modified Ferritic Stainless Steel. Journal of Phase Equilibrium Diffusion, v. 38, 343–349, 2017. Doi: 10.1007/s11669-017-0550-y

[11] D.D.S. Silva, A.R.C. Nascimento, G.Y. Koga, G. Zepon, C.S. Kiminami, W.J. Botta, C. Bolfarini. Alloy design for microstructural-tailored boron modified ferritic stainless steel to ensure corrosion and wear resistance. Journal of Materials Research and Technology, v. 24, 418-429, 2023. Doi: 10.1016/j.jmrt.2023.03.023

[12] G.Y. Koga, G. Zepon, L.S. Santos, C. Bolfarini, C.S. Kiminami, W.J. Botta. Wear Resistance of Boron-Modified Supermartensitic Stainless Steel Coatings Produced by High-Velocity Oxygen Fuel Process. Journal of Thermal Spray Technology, v. 28, 2003–2014, 2019. Doi: 10.1007/s11666-019-00961-2

[13] R.P.M. Guimarães, L. Minkowitz, S. Arneitz, C. Sommitsch, J. Giedenbacher, M. Müller, A. Huskic, N. Wild, R.H. Buzolin, B. Meier, M. Skalon, F. Haas, S.T. Amancio-Filho. 1 - Powder bed fusion processes: main classes of alloys, current status, and technological trends. Advances in Metal Additive Manufacturing Woodhead Publishing Reviews: Mechanical Engineering Series, 1-104, 2023. DOI: 10.1016/B978-0-323-91230-3.00003-2

[14] P.F. Jiang, C.H. Zhang, S. Zhang, J.B. Zhang, J. Chen, H.T. Chen. Additive manufacturing of novel ferritic stainless steel by selective laser melting: Role of laser scanning speed on the formability, microstructure and properties. Optics and Laser Technology, v. 140, 107055, 2021. Doi: 10.1016/j.optlastec.2021.107055

[15] W. Zhao, H. Xiang, R. Yu, G. Mou. Effects of laser scanning speed on the microstructure and mechanical properties of 2205 duplex stainless steel fabricated by selective laser melting. Journal of Manufacturing Processes, v. 94, 1-9, 2023. Doi: 10.1016/j.jmapro.2023.03.068

[16] A. Durga, N.H. Pettersson, S.B.A. Malladi, Z. Chen, S. Guo, L. Nyborg, G. Lindwall. Grain refinement in additively manufactured ferritic stainless steel by in

situ inoculation using pre-alloyed powder. Scripta Materialia, v.194, 113690, 2021. Doi: 10.1016/j.scriptamat.2020.113690

[17] H. Ikehata, D. Mayweg, E. Jagle. Grain refinement of Fe-Ti alloys fabricated by laser powder bed fusion, Materials Design, v. 204, 109665, 2021. Doi: 10.1016/j. matdes.2021.109665.

[18] D. Karlsson, C.Y. Chou, N.H. Pettersson, T. Helander, P. Harlin, M. Sahlberg, G. Lindwall, J. Odqvist, U.Jansson. Additive manufacturing of the ferritic stainless steel SS441. Additive Manufacturing, v. 36, 101580, 2020. Doi: 10.1016/j.addma.2020.101580

[19] H. Ikehata, E. Jagle. Evaluation of microstructure and tensile properties of grain-refined, Ti-alloyed ferritic stainless steel fabricated by laser powder bed fusion. Materials Science & Engineering A, v. 818, 141365, 2021. Doi: 10.1016/j.msea.2021.141365

[20] Y. Fang, M.K. Kim, Y. Zhang, T. Kim, J. No, J. Suhr. A new grain refinement route for duplex stainless steels: Micro-duplex stainless steel matrix composites processed by laser powder bed fusion. Materials Science & Engineering A, v. 881, 145351, 2023. Doi: 10.1016/j.msea.2023.145351

[21] V.P.N. Samy, M. Schafle, F. Brasche, U. Krupp, C. Haase. Understanding the mechanism of columnar–to-equiaxed transition and grain refinement in additively manufactured steel during laser powder bed fusion. Additive Manufacturing, v. 73, 103702, 2023. Doi: 10.1016/j.addma.2023.103702

[22] Q. Tan, Y. Yin, A. Prasad, G. Li, Q. Zhu, D. Henry StJohn, M.X. Zhang. Demonstrating the roles of solute and nucleant in grain refinement of additively manufactured aluminium alloys. Additive Manufacturing, v. 49, 102516, 2022. Doi: 10.1016/j.addma.2021.102516

[23] A. Prasad, L. Yuan, P. Lee, M. Patel, D. Qiu, M. Easton, D; StJohn. Towards understanding grain nucleation under Additive Manufacturing solidification conditions. Acta Materialia, v. 195, 392-403, 2020. Doi: 10.1016/j.actamat.2020.05.012

[24] M. Bermingham, D. StJohn, M. Easton, L. Yuan, M. Dargusch. Revealing the Mechanisms of Grain Nucleation and Formation During Additive Manufacturing.

Journal of The Minerals, Metals & Materials Society, v. 72, 3, 2020. Doi: 10.1007/s11837-020-04019-5

[25] L. Kaserer, D. Brennsteiner, J. Braun, V. Goettgens, I. Letofsky–Papst, P. Singer, H. Kestler, W. Schafbauer, G. Leichtfried. Solute-induced grain refinement and defect suppression in boron modified molybdenum manufactured via laser powder-bed fusion. International Journal of Refractory Metals and Hard Materials, v. 117, 106384, 2023. Doi: 10.1016/j.ijrmhm.2023.106384

[26] Q. Zheng, H.S. Chen, J. Zhou, W. Wang, S.X. Xi, Y. Yuan. Effect of boron element on microstructure and mechanical properties of 316L stainless steel manufactured by selective laser melting. Journal of Materials Research and Technology, v. 26, 3744e3755, 2023. Doi: 10.1016/j.jmrt.2023.08.148

[27] J. Braun, L. Kaserer, J. Stajkovic, H. Kestler, G. Leichtfried. Grain refinement mechanisms of alloying molybdenum with carbon manufactured by laser powder bed fusion. Materials & Design, v. 215, 110507, 2022. Doi: 10.1016/j.matdes.2022.110507

[28] H. Okamoto. Desk handbook phase diagrams for binary alloys. Materials Park, OH: ASM International, 2000. 978-1615030460

[29] B.J.M. Freitas, V.A. Oliveira, P. Gargarella, G.Y. Koga, C. Bolfarini. Microstructural characterization and wear resistance of boride-reinforced steel coatings produced by Selective Laser Melting (SLM). Surface & Coatings Technology, v. 426, 127779, 2021. Doi: 10.1016/j.surfcoat.2021.127779

[30] N.J. Calos, E. Graham, D.R. Cousens, P. Christodoulou, C.H.L. Kennard, L.K. Bekessy, S.F. Parker. Mode of Boron Solubility in Ferrous Alloys. Materials Transaction, vol. 42, 496–501, 2001. Doi: 10.2320/matertrans.42.496

[31] J. Soyama, C.T. Rios. Microstructure and mechanical properties of a rapid solidified boron- modified duplex stainless steel. Materials Science and Technology, v. 35:7, 815-822, 2019. Doi: 10.1080/02670836.2019.1591030

[32] Amt B.S. "EN ISO/ASTM 52900: 2017- Additive manufacturing. General principles. Fundamentals and vocabulary.

[33] N. Haghdadi, H. Chen, Z. Chen, S.S. Babu, X. Liao, S.P. Ringer, S. Primig. Intergranular precipitation and chemical fluctuations in an additively

manufactured 2205 duplex stainless steel. Scripta Materialia, v. 219, 114894, 2022. Doi: 10.1016/j.scriptamat.2022.114894

[34] S.R. Narasimharaju, W. Zeng, T.L. See, Z. Zhu, P.Scott, X. Jiang, S. Lou. A comprehensive review on laser powder bed fusion of steels: Processing, microstructure, defects and control methods, mechanical properties, current challenges and future trends. Journal of Manufacturing Processes, v. 75, 375–414, 2022. Doi: 10.1016/j.jmapro.2021.12.033

[35] T. DebRoy, H.L. Wei, J.S. Zuback, T. Mukherjee, J.W. Elmer, J.O. Milewski, A.M. Beese, A. Wilson-Heid, A. De, W. Zhang. Additive manufacturing of metallic components – Process, structure and properties. Progress in Materials Science, v. 92, 112-224, 2018. Doi: 10.1016/j.pmatsci.2017.10.001

[36] X. Zhang, C.J. Yocom, B. Mao, Y. Liao. Microstructure evolution during selective laser melting of metallic materials: A review. Journal of Laser Application, v. 31 (3), 031201, 2019. Doi: 10.2351/1.5085206

[37] D.C. Montgomery. Design and Analysis of Experiments, 8th ed.; Arizona State University: Tempe, AZ, USA, 2013. 978-1118146927

[38] T.N. Le, Y.L. Lo. Effects of sulfur concentration and Marangoni convection on melt-pool formation in transition mode of selective laser melting process. Materials and Design, v. 179, 107866, 2019. Doi: 10.1016/j.matdes.2019.107866

[39] P. Murkute, S. Pasebani, O.B. Isgor. Metallurgical and electrochemical properties of super duplex stainless steel clads on low carbon steel substrate produced with laser powder bed fusion. Scientific Reports, v. 10 (1), 10162, 2020. Doi: 10.1038/s41598-020-67249-2

[40] P. Murkute, S. Pasebani, O.B. Isgor. Effects of heat treatment and applied stresses on the corrosion performance of additively manufactured super duplex stainless steel clads. Materialia, v. 14, 100878, 2020. Doi: 10.1016/j.mtla.2020.100878

[41] A.K.S. Chauhan, M. Shukla. Residual Stress Modeling and Simulation of Direct Metal Laser Sintered Ti-6Al-4V Alloy, Materials Today Proceedings, v. 18, 7, 5189-5195, 2019. Doi: 10.1016/j.matpr.2019.07.518

[42] Z. Chen, Y. Xiang, Z. Wei, P. Wei, B. Lu, L. Zhang, J. Du. Thermal dynamic behavior during selective laser melting of K418 superalloy: numerical simulation

and experimental verification. Applied Physics A, v.. 124, 313, 2018. Doi: 10.1007/s00339-018-1737-8

[43] T. Niendorf, S. Leuders, A. Riemer, H.A. Richard, D. Schwarze, T. Troster. Highly anisotropic steel processed by selective laser melting. Metallurgical and Materials Transactions B, v. 44, 794–796, 2013. Doi: 10.1007/s11663-013-9875-z

[44] W. Kurz, D.J. Fisher, Fundamentals of Solidification, Transaction Technology Publications, 1986. ISBN 0-87849-523-3. Doi: 10.1002/crat.2170210909

[45] S. Kou. Welding metallurgy. (2nd edition), John Wiley & Sons, 2003. ISBN 0-471-43491-4. Doi: 10.1002/0471434027

[46] W. Kurz, B. Giovanola, R. Trivedi. Theory of microstructural development during rapid solidification. Acta Metallurgic, v. 34, 823-830, 1986. Doi: 10.1016/0001-6160(86)90056-8

[47] M. Garibaldi, I. Ashcroft, M. Simonelli, R. Hague. Metallurgy of high-silicon steel parts produced using selective laser melting. Acta Materialia, v. 110, 207-216, 2016. Doi: 10.1016/j.actamat.2016.03.037

[48] N. Haghdadi, C. Ledermueller, H. Chen, Z. Chen, Q. Liu, X. Li, G. Rohrer, X. Liao, S. Ringer, S. Primig. Evolution of microstructure and mechanical properties in 2205 duplex stainless steels during additive manufacturing and heat treatment. Materials Science and Engineering A, v. 835, 142695, 2022. Doi: 10.1016/j.msea.2022.142695

[49] F. Hengsbach, P. Koppa, K. Duschik, M.J. Holzweissig, M. Burns, J. Nellesen, W. Tillmann, T. Tröster, K.P. Hoyer, M. Schaper. Duplex stainless steel fabricated by selective laser melting - Microstructural and mechanical properties. Materials and Design, v. 133, 136–142, 2017. Doi: 10.1016/j.matdes.2017.07.046

[50] K. Davidson, S. Singamneni. Selective Laser Melting of Duplex Stainless Steel Powders: an Investigation. Materials and Manufacturing Processes, v. 31:12, 1543-1555, 2016. Doi: 10.1080/10426914.2015.1090605

[51] F. Shang, X. Chen, Z. Wang, Z. Ji, F. Ming, S. Ren, X. Qu. The microstructure, mechanical properties, and corrosion resistance of UNS S32707

hyper-duplex stainless steel processed by selective laser melting. Metals, v. 9, 1012, 2019. Doi: 10.3390/met9091012

[52] S. Papula, M. Song, A. Pateras, X.-B. Chen, M. Brandt, M. Easton, Y. Yagodzinskyy, I. Virkkunen, H. Hänninen. Selective laser melting of duplex stainless steel 2205: effect of post-processing heat treatment on microstructure, mechanical properties, and corrosion resistance. Materials, v. 12, 2468, 2019. Doi: 10.3390/ma12152468

[53] J. Kunz, A. Boontanom, S. Herzog, P. Suwanpinij, A. Kaletsch, C. Broeckmann. Influence of hot isostatic pressing post-treatment on the microstructure and mechanical behavior of standard and super duplex stainless steel produced by laser powder bed fusion. Materials Science & Engineering A, v. 794, 139806, 2020. Doi: 10.1016/j.msea.2020.139806

[54] N. Haghdadi, M. Laleh, H. Chen, Z. Chen, C. Ledermueller, X. Liao, S. Ringer, S. Primig. On the pitting corrosion of 2205 duplex stainless steel produced by laser powder bed fusion additive manufacturing in the as-built and postprocessed conditions. Materials & Design, v. 212, 110260, 2021. Doi: 10.1016/j.matdes.2021.110260

[55] G.N. Nigon, O.B. Isgor, S. Pasebani. The effect of annealing on the selective laser melting of 2205 duplex stainless steel: Microstructure, grain orientation, and manufacturing challenges. Optics & Laser Technology, v. 134, 106643, 2021. Doi: 10.1016/j.optlastec.2020.106643

[56] B.J.M. Freitas, L.C.M. Rodrigues, C.A.E. Claros, W.J. Botta, G.Y. Koga, C. Bolfarini. Ferritic-induced high-alloyed stainless steel produced by laser powder bed fusion (L-PBF) of 2205 duplex stainless steel: Role of microstructure, corrosion, and wear resistance. Journal of Alloys and Compounds, v. 918, 165576, 2022. Doi: 10.1016/j.jallcom.2022.165576

[57] H. Xiang, W. Zhao, Y. Lu. Effect of solution temperature on microstructure and mechanical properties of selective laser melted Fe–22Cr–5Ni-0.26N duplex stainless steel. Journal of Materials Research and Technology, v. 19, 1379-1389, 2022. Doi: 10.1016/j.jmrt.2022.05.124

[58] S. Jeffs, R. Douglas, W. Beard, M. Coleman, J. Adams, T. Jones, D. Poole, R. Lancaster. Characterizing the high temperature tensile behaviour of laser

powder bed fused duplex stainless steel 2205 using the small punch test. Materials Characterization, v. 189, 111953, 2022. Doi: 10.1016/j.matchar.2022.111953

[59] C. Cui, L. Becker, E. Gärtner, J. Boes, J. Lentz, V. Uhlenwinkel, M. Steinbacher, S. Weber, R.F. Heinen. Laser Additive Manufacturing of Duplex Stainless Steel via Powder Mixture. Journal of Manufacturing and Materials. Processing, v. 6, 72, 2022. Doi: 10.3390/jmmp6040072

[60] M. Mirz, S. Herzog, C. Broeckmann, A. Kaletsch. Influence of the L-PBF Process Atmosphere on the Microstructure and Tensile Properties of AISI 318LN Duplex Stainless Steel. Journal of Manufacturing and Materials Processing, v. 6, 32, 2022. Doi: 10.3390/jmmp6020032

[61] M. Laleh, N. Haghdadi, A.E. Hughes, S. Primig, M.Y.J. Tan. Enhancing the repassivation ability and localised corrosion resistance of an additively manufactured duplex stainless steel by post-processing heat treatment. Corrosion Science, v. 198, 110106, 2022. Doi: 10.1016/j.corsci.2022.110106

[62] J. Zhang, H. Zhu, X. Xi, X. Li, Z. Xiao. Anisotropic response in mechanical and corrosion performances of UNS S31803 duplex stainless steel fabricated by laser powder bed fusion. Journal of Materials Research and Technology, v. 26, 4860-4870, 2023. Doi: 10.1016/j.jmrt.2023.08.199

[63] A. Mulhi, S. Dehgahi, P. Waghmare, A.J. Qureshi. Process Parameter Optimization of 2507 Super Duplex Stainless Steel Additively Manufactured by the Laser Powder Bed Fusion Technique. Metals, v. 13(4), 725, 2023. Doi: 10.3390/met13040725

[64] C. Xie, B. Li, G. Liu, J. Liu, H. Ying, D. Li, S. Wang, L. Wang. Study on the effect of solution treatment on mechanical and corrosion properties of SAF 2507DSS produced by LPBF. Journal of Materials Research and Technology; v. 26: 2070e2081, 2023. Doi: 10.1016/j.jmrt.2023.08.057

[65] X. Lin, T.M. Yue, H.O. Yang, W.D. Huang. Solidification Behavior and the Evolution of Phase in Laser Rapid Forming of Graded Ti6Al4V-Rene88DT Alloy. Metallurgical and Materials Transaction A, v. 38, 127, 2007. Doi: 10.1007/s11661-006-9021-5

[66] V. Manvatkar, A. De, T. DebRoy. Heat transfer and material flow during laser assisted multi-layer additive manufacturing. Journal of Applied Physics; v. 116 (12): 124905, 2014. Doi: 10.1063/1.4896751

[67] M.H. Mosallanejad, B. Niroumand, A. Aversa, A. Saboori. In-situ alloying in laser-based additive manufacturing processes: A critical review. Journal of Alloys and Compounds, v. 872, 159567, 2021. DOI: 10.1016/j.jallcom.2021.159567

[68] ASTM International ASTM B214–07 Standard Test Method for Sieve Analysis of Metal Powders, 2016. Doi: 10.1520/B0214–16

[69] Coherent Inc., “Creator,” 2019. https://content.coherent.com/legacy-assets/pdf/COHR_CREATOR_DS_0119_1.pdf (accessed Sep. 28, 2021).

[70] L. Minkowitz, S. Arneitz, P.S. Effertz, S.T. Amancio-Filho. Laser-powder bed fusion process optimisation of AlSi10Mg using extra trees regression. Materials & Design, v. 227, 111718, 2023. 10.1016/j.matdes.2023.111718

[71] ASTM International ASTM E384–17 Standard Test Method for Microindentation Hardness of Materials, 2017. Doi: 10.1520/E0384–17

[72] ASTM International ASTM G133–05 Standard Test Method for Linearly Reciprocrating Ball-on-Flat Sliding Wear, 2016. Doi: 10.1520/G0133–05R16

[73] J. Tafel. Über die Polarisation bei kathodischer Wasserstoffentwicklung. Zeitschrift für Physikalische Chemie, 50, 641, 1905. DOI: 10.1515/zpch-1905-5043

[74] ISO 12732:2006 Corrosion of metals and alloys — Electrochemical potentiokinetic reactivation measurement using the double loop method (based on Cihal's method) 20060.

[75] M. Femenia, J. Pan, C. Leygraf, P. Luukkonen. In situ study of selective dissolution of duplex stainless steel 2205 by electrochemical scanning tunnelling microscopy. Corrosion Science, v. 43, 1939-1951, 2001. Doi: 10.1016/s0010-938x(00)00180-3

[76] K. Saeidi, L. Kevetkova, F. Lofaj, Z. Shen. Novel ferritic stainless steel formed by laser melting from duplex stainless-steel powder with advanced mechanical properties and high ductility. Materials Science and Engineering A, v. 665, 59-65, 2016. Doi: 10.1016/j.msea.2016.04.027

[77] D. Jiang, N. Birbilis, C.R. Hutchinson, M. Brameld. On the microstructure and electrochemical properties of additively manufactured duplex stainless steels produced using laser-powder bed fusion. Corrosion, v. 76 (9), 871-883, 2020. Doi: 10.5006/3571

[78] N. Ciftci, N. Ellendt, G. Coulthard, E.S. Barreto, L. Madler, V. Uhlenwinkel. Novel cooling rate correlations in molten metal gas atomization. Metallurgical and Materials Transaction B, v. 666 (50B), 2019. Doi: 10.1007/s11663-019-01508-0

[79] K. Kassym, A. Perveen. Atomization processes of metal powders for 3D printing. Materials Today Proceedings, v. 26, 1727-1733, 2020. Doi: 10.1016/j.matpr.2020.02.364

[80] J.D. Kechagias, N. Vidakis. Parametric optimization of material extrusion 3D printing process: an assessment of Box-Behnken vs. full-factorial experimental approach, The International Journal of Advanced Manufacturing Technology, v. 121, 3163–3172, 2022. Doi: 10.1007/s00170-022-09532-2

[81] M. Giovagnoli, G. Silvi, M. Merlin, M.T.D. Giovanni. Optimisation of process parameters for an additively manufactured AlSi10Mg alloy: Limitations of the energy density-based approach on porosity and mechanical properties estimation. Mater. Sci. Eng. A, 802, 140613, 2021. DOI: 0.1016/j.msea.2020.140613

[82] Q. Deng, X. Wang, Q. Lan, Z. Chang, Z. Liu, N. Su, Y. Wu, D. Liu, L. Peng, W. Ding. Limitations of linear energy density for laser powder bed fusion of Mg-15Gd-1Zn-0.4Zr alloy. Mater. Charact., 190, 112071, 2022. DOI: 10.1016/j.matchar.2022.112071

[83] K.P. Davidson, S.B. Singamneni. Metallographic evaluation of duplex stainless steel powders processed by selective laser melting. Rapid Prototyping. Journal, 23 (6), 1146-1163, 2017. Doi: 10.1108/RPJ-04-2016-0053

[84] P. Hou, S. Mooraj, V.K. Champagne, M.J. Siopis, P.K. Liaw, S. Gerasimidis, W. Chen, Effect of build height on temperature evolution and thermally induced residual stresses in plasma arc additively manufactured stainless steel, Metallurgical and Materials Transaction A, v. 53, 627–639, 2022. Doi: 10.1007/s11661-021-06538-5.

[85] S. Feng, S. Guan, S. Zhang, S. Mooraj, M. Luebbe, X. Fan, K.A. Beyer, T. Li, J. Liu, J. Kong, P.K. Liaw, H. Wen, S. Gerasimidis, W. Chen. Ultrafine-grained Fe-TiB2 high-modulus nanocomposite steel with high strength and isotropic mechanical properties by laser powder bed fusion. Additive Manufacturing, v. 70, 103569, 2023. Doi: 10.1016/j.addma.2023.103569

[86] Y.M. Wang, T. Voisin, J.T. McKeown, J. Ye, N.P. Calta, Z. Li, Z. Zeng, Y. Zhang, W. Chen, T.T. Roehling, R.T. Ott, M.K. Santala, P.J. Depond, M.J. Matthews, A.V. Hamza, T. Zhu. Additively manufactured hierarchical stainless steels with high strength and ductility. Nature Materials, v. 17, 63–70, 2018. Doi: 10.1038/NMAT5021.

[87] H.L. Wei, J. Mazumder, T. DebRoy. Evolution of solidification texture during additive manufacturing, Scientific Reports, v. 5, 1–7, 2015. Doi: 10.1038/srep16446

[88] G. Liang, Y. Ali, G. You, M.X. Zhang. Effect of cooling rate on grain refinement of cast aluminium alloys. Materialia, v. 3, 113-121, 2018. Doi: 10.1016/j.mtla.2018.08.008

[89] P. Bidare, I. Bitharas, R.M. Ward, M.M. Attallah, A.J. Moore, Fluid and particle dynamics in laser powder bed fusion, Acta Materialia, v. 142, 107–120, 2018. Doi: 10.1016/j.actamat.2017.09.051

[90] J.H. Devletian, R.W. Heine. Grain Refining Effect of Boron in Carbon Steel Welds. Welding Research Supplement, 529-535, 1973.

[91] W.E. Frazier, Metal Additive Manufacturing: A Review. Journal of Materials Engineering and Performance, v. 23, 1917-1928, 2014. Doi: 10.1007/s11665-014-0958-z

[92] M.X. Yao, J.B.C. Wu, W. Xu, R. Liu. Metallographic study and wear resistance of a high-C wrought Co-based alloy Stellite 706K. Materials Science and Engineering A, v. 407, 1–2, 291-298, 2005. Doi: 10.1016/j.msea.2005.07.053

[93] Y. Zou, C. Tan, Z. Qiu, W. Ma, M. Kuang, D. Zeng. Additively manufactured SiC-reinforced stainless steel with excellent strength and wear resistance. Additive Manufacturing, v. 41, 101971, 2021. Doi: 10.1016/j.addma.2021.101971

[94] B. Almangour, D. Grzesiak, J.M. Yang. Rapid Fabrication of Bulk-form TiB2/316L Stainless Steel Nanocomposites with Novel Reinforcement

Architecture and Improved Performance by Selective Laser Melting. Journal of Alloys and Compounds, v. 680, 480-493, 2016. Doi: 10.1016/j.jallcom.2016.04.156

[95] X.F. Wang, X.P. Yang, Z.D. Guo, Y.C. Zhou, H.W. Song, Nanoindentation characterization of mechanical properties of ferrite and austenite in duplex stainless steel, Journal of Advanced Materials Research, v. 26-28, 1165–1170, 2007. Doi: 10.4028/www.scientific.net/amr.26-28.1165

[96] J. Lubas. Tribological properties of surface layer with boron in friction pairs. Surface Review and Letters, v. 16, 767-773, 2009. Doi: 10.1142/S0218625X09013232

[97] D. Wallindera, J. Pan, C. Leygraf, A. Delblanc-Bauer. EIS and XPS study of surface modification of 205LVM stainless steel after passivation. Corrosion Science, v. 41, 275-289, 1999. Doi: 10.1016/s0010-938x(98)00122-x

[98] G.R. Engelhardt, R.P. Case, D. Macdonald. Electrochemical impedance spectroscopy optimization on passive metals. Journal of Electrochemical Society, v. 163 (8), 470-476, 2016. Doi:10.1149/2.0811608jes

[99] Y.H. Yang, Y. Gu. Effect of Mn addition on mechanical property and corrosion behavior in hot rolled 19% Cr duplex stainless steel. Journal of Advanced Materials Research, v. 1004–1005, 231-234, 2014. Doi: 10.4028/www.scientific.net/amr.1004-1005.231

[100] Z. Brytan, J. Niagaj, Ł. Reiman. Corrosion studies using potentiodynamic and EIS electrochemical techniques of welded lean duplex stainless steel UNS S82441. Applied Surface Science, v. 388, 160-168, 2016. Doi: 10.1016/j.apsusc.2016.01.260

[101] A.A. Akilan, S.D. Nath, R.K. Enneti, G. Gupta, S.V. Atre. Mechanical and corrosion properties of gas and water atomized laser-powder bed fusion fabricated 25Cr7Ni stainless steel. Manufacturing Letters, v. 31, 60–63, 2022. Doi: 10.1016/j.mfglet.2021.07.006

[102] K.D. Ralston, N. Birbilis. Effect of Grain Size on Corrosion: A Review. Corrosion, v. 66, 7, 2010. Doi: 10.5006/1.3462912

[103] R.K. Gupta, N. Birbilis. The influence of nanocrystalline structure and processing route on corrosion of stainless steel: A review. Corrosion Science, v. 92, 1-15, 2015. Doi: 10.1016/j.corsci.2014.11.041

[104] L. Jinlong, L. Tongxiang, W. Chen, D. Limin. Effect of ultrafine grain on tensile behaviour and corrosion resistance of the duplex stainless steel. Materials Science and Engineering C, v. 62, 558-563, 2016. Doi: 10.1016/j.msec.2016.02.008

[105] V.S. Moura, L.D. Lima, J.M. Pardal, A.Y. Kina, R.R.A. Corte, S.S.M. Tavares. Influence of microstructure on the corrosion resistance of the duplex stainless steel UNS S31803. Materials Characterization, v. 59 (8), 1127-1132, 2018. Doi: 10.1016/j.matchar.2007.09.002

[106] K.S. Assis, A.C. Rocha, I.C.P. Margarit-Mattos, F.A.S. Serra, O.R. Mattos. Practical aspects on the use of on-site double loop electrochemical potentiodynamic reactivation technique (DL-EPR) for duplex stainless steel. Corrosion Science, v. 74, 250-255, 2013. Doi: 10.1016/j.corsci.2013.04.050

[107] K.W. Chan, S.C. Tjong. Effect of Secondary Phase Precipitation on the Corrosion Behavior of Duplex Stainless Steels. Materials, 7(7), 5268-5304, 2014. DOI: 10.3390/ma7075268

[108] T.H. Chen, J.R. Yang. Effects of solution treatment and continuous cooling on σ-phase precipitation in a 2205 duplex stainless steel. Materials Science and Engineering A, v. 311 (1–2), 28-41, 2001. Doi: 10.1016/s0921-5093(01)00911-x

APPENDIX A

Table A.1 - Experiments applied for the L-PBF-parameters optimization using Box-Behnken design.

Experiment	Laser power (W)	Scanning speed (mm/s)	Hatching (µm)
1	150	600	60
2	250	600	60
3	150	1200	60
4	250	1200	60
5	150	900	30
6	250	900	30
7	150	900	90
8	250	900	90
9	200	600	30
10	200	1200	30
11	200	600	90
12	200	1200	90
13 [1]	200	900	60
14 [1]	200	900	60
15 [1]	200	900	60
16 [1]	200	900	60
17 [1]	200	900	60
18 [1]	200	900	60
19 [1]	200	900	60
20 [1]	200	900	60
21 [1]	200	900	60
22 [1]	200	900	60

[1] 10 samples were used as the central point of Box-Behnken design.

Table A.2 - Experimental porosity, predicted porosity and model validation for the Pure-LPBF alloy.

Experiment	Laser power (W)	Scanning speed (mm/s)	Hatching (µm)	Experimental porosity (%)	Predicted porosity (%)

1	150	600	60	0.45	0.70
2	250	600	60	0.03	-0.04
3	150	1200	60	1.13	0.99
4	250	1200	60	0.21	0.24
5	150	900	30	0.97	0.85
6	250	900	30	0.06	0.10
7	150	900	90	0.83	0.85
8	250	900	90	0.04	0.10
9	200	600	30	0.54	0.47
10	200	1200	30	0.40	0.76
11	200	600	90	0.53	0.47
12	200	1200	90	0.97	0.76
13 [1]	200	900	60	0.70	0.61
14 [1]	200	900	60	0.63	0.61
15 [1]	200	900	60	0.67	0.61
16 [1]	200	900	60	0.61	0.61
17 [1]	200	900	60	0.60	0.61
18 [1]	200	900	60	0.56	0.61
19 [1]	200	900	60	0.53	0.61
20 [1]	200	900	60	0.51	0.61
21 [1]	200	900	60	0.65	0.61
22 [1]	200	900	60	0.58	0.61
23 [2]	230	700	90	0.04	0.24
24 [2]	230	1000	90	0.22	0.38
25 [2]	150	700	90	0.42	0.75
26 [2]	150	800	90	0.51	0.80
27 [2]	150	1000	90	0.88	0.89
28 [2]	170	700	90	0.38	0.69

[1] Samples for the central point of Box-Behnken.
[2] Samples used to the model validation.

Table A.3 - Experimental porosity, predicted porosity and model validation for the 0.3B-LPBF alloy.

Experiment	Laser power (W)	Scanning speed (mm/s)	Hatching (µm)	Experimental porosity (%)	Predicted porosity (%)
1	150	600	60	2.11	1.93
2	250	600	60	0.06	0.11
3	150	1200	60	5.80	6.49
4	250	1200	60	0.04	0.95
5	150	900	30	3.80	3.22
6	250	900	30	0.10	-0.46
7	150	900	90	3.25	3.22
8	250	900	90	0.03	-0.46
9	200	600	30	0.20	0.24
10	200	1200	30	3.47	2.94
11	200	600	90	0.17	0.24
12	200	1200	90	4.19	2.94
13 [1]	200	900	60	1.09	0.60
14 [1]	200	900	60	1.05	0.60
15 [1]	200	900	60	1.03	0.60
16 [1]	200	900	60	0.22	0.60
17 [1]	200	900	60	0.21	0.60
18 [1]	200	900	60	0.23	0.60
19 [1]	200	900	60	0.20	0.60
20 [1]	200	900	60	0.20	0.60
21 [1]	200	900	60	0.18	0.60
22 [1]	200	900	60	0.26	0.60
23 [2]	150	700	90	2.14	2.14
24 [2]	150	800	90	3.44	2.57
25 [2]	150	1000	90	4.68	4.09
26 [2]	170	700	90	0.68	1.15
27 [2]	170	700	50	0.92	1.15
28 [2]	230	700	90	0.08	-0.31
29 [2]	230	1000	90	0.09	0.15

[1] 10 samples were used as the central point in Box-Behnken.

[2] Samples used as the validation points.

Table A.4 - Experimental porosity, predicted porosity and model validation for the 0.6B-LPBF alloy.

Experiment	Laser power (W)	Scanning speed (mm/s)	Hatching (µm)	Experimental porosity (%)	Predicted porosity (%)
1	150	600	60	0.90	1.00
2	250	600	60	0.05	0.27
3	150	1200	60	4.12	4.43
4	250	1200	60	0.19	0.64
5	150	900	30	2.56	2.08
6	250	900	30	0.10	-0.18
7	150	900	90	2.07	2.08
8	250	900	90	0.11	-0.18
9	200	600	30	0.28	0.14
10	200	1200	30	2.31	2.05
11	200	600	90	0.21	0.14
12	200	1200	90	2.62	2.05
13 [1]	200	900	60	0.74	0.46
14 [1]	200	900	60	0.41	0.46
15 [1]	200	900	60	0.25	0.46
16 [1]	200	900	60	0.21	0.46
17 [1]	200	900	60	0.22	0.46
18 [1]	200	900	60	0.19	0.46
19 [1]	200	900	60	0.21	0.46.
20 [1]	200	900	60	0.29	0.46
21 [1]	200	900	60	0.52	0.46
22 [1]	200	900	60	0.42	0.46
23 [2]	150	700	90	1.66	1.22
24 [2]	150	800	90	1.26	1.58
25 [2]	150	1000	90	2.31	2.73
26 [2]	170	700	90	0.80	0.66
27 [2]	250	1200	30	0.09	0.64

28 [2]	230	700	90	0.19	-0.09
29 [2]	230	1000	90	0.11	0.20

[1] 10 samples were used as the central point in Box-Behnken.
[2] Samples used as the validation points.

Table A.5 - Analysis of variance (ANOVA) of the results shown in Table A.2 for the Pure-LPBF alloy.

Factor	SQ	MQ	F-value	P-value
P	1.15520	1.15520	90.34	0.000
V	0.16820	0.16820	13.15	0.003
H	0.02000	0.02000	1.56	0.235
P×P	0.09489	0.09489	7.42	0.018
V×V	0.00023	0.00023	0.02	0.895
H×H	0.00080	0.00080	0.06	0.807
P×V	0.06250	0.06250	4.89	0.047
P×H	0.00360	0.00360	0.28	0.605
V×H	0.08410	0.08410	6.58	0.025
Misfit	0.12020	0.04007	10.85	0.002

SQ: sum of square; MQ: mean of square; P-value: probability level; P: laser power; V: scanning speed; H: hatching.

Table A.6 - Analysis of variance (ANOVA) of the results shown in Table A.3 for the 0.3B-LPBF alloy.

Factors	SQ	MQ	F-value	P-value
P	27.122	27.1216	75.64	0.000
V	15.015	15.0152	41.88	0.000
H	0.0006	0.0006	0.00	0.964
P×P	2.948	2.9484	8.22	0.011
V×V	4.776	4.7761	13.32	0.002
H×H	2.0905	2.0905	7.28	0.019
P×V	3.441	3.4410	9.60	0.007
P×H	0.0576	0.0576	0.20	0.662
V×H	0.1406	0.1406	0.49	0.498

Misfit	4.241	0.6058	3.64	0.0038

SQ: sum of square; MQ: mean of square; P-value: probability level; P: laser power; V: scanning speed; H: hatching.

Table A. 7 - Analysis of variance (ANOVA) of the results shown in Table A.4 for the 0.6B-LPBF alloy.

Factors	SQ	MQ	F-value	P-value
P	10.5800	10.5800	248.24	0.000
V	7.6050	7.6050	178.44	0.000
H	0.0072	0.0072	0.17	0.688
P×P	0.7988	0.7988	18.74	0.001
V×V	1.4600	1.4600	34.26	0.000
H×H	0.9614	0.9614	22.56	0.000
P×V	2.3716	2.3716	55.65	0.000
P×H	0.0625	0.0625	1.47	0.249
V×H	0.0361	0.0361	0.85	0.376
Misfit	0.2268	0.0756	2.39	0.136

SQ: sum of square; MQ: mean of square; P-value: probability level; P: laser power; V: scanning speed; H: hatching.

Table A.8 - Influence of the hatching on the porosity of the alloys obtained by L-PBF. Five printed samples were used for each condition.

Alloy	Experiment	Power (W)	Speed (mm/s)	Layer thickness (µm)	Beam diameter	Hatching (µm)	Porosity (%)
Pure	1	250	600	25	40	30	0.04 ± 0.03
	2	250	600	25	40	60	0.06 ± 0.03
	3	250	600	25	40	90	0.03 ± 0.01
0.3	1	250	830	25	40	30	0.16 ± 0.07
	2	250	830	25	40	60	0.02 ± 0.01
	3	250	830	25	40	90	0.03 ± 0.02
0.6	1	250	850	25	40	30	0.09 ± 0.03
	2	250	850	25	40	60	0.03 ± 0.01

	3	250	850	25	40	90	0.05 ± 0.02

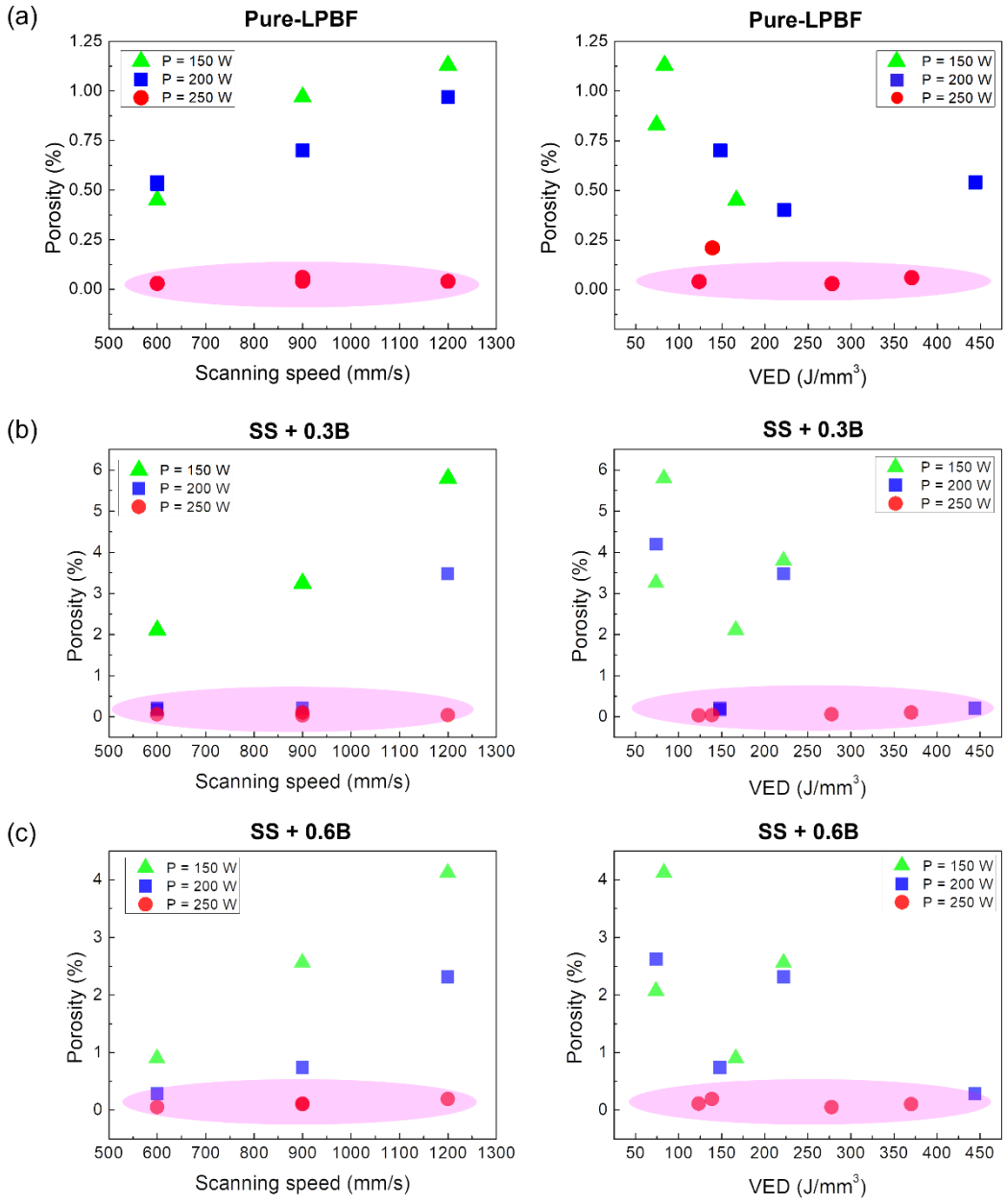

Figure A.1 - Relative density for the studied alloys varying scanning speed and the corresponding volumetric energy density (VED) for (a) Pure-LPBF, (b) 0.3B-LPBF, and (c) 0.6B-LPBF specimens. VED was obtained from the equation VED= P⁄((v × t ×h))[60], in which P, v, t, h represent laser power, scanning speed, layer thickness, and hatching distance, respectively.